SLAC-R-520
UC-414

Measurement of the Polarized Forward-Backward Asymmetry of s-Quarks at SLD*

Shinya Narita

Stanford Linear Accelerator Center
Stanford University
Stanford, CA 94309

SLAC-Report-520
March 1998

Prepared for the Department of Energy
under contract number DE-AC03-76SF00515

Printed in the United States of America. Available from the National Technical Information Service, U.S. Department of Commerce, 5285 Port Royal Road, Springfield, VA 22161.

*Ph.D. thesis, Tohoku University

Abstract

This thesis presents a direct measurement of the parity-violating parameter A_s by analyzing the polarized forward-backward asymmetry of s quarks in $e^+e^- \to Z^0 \to s\bar{s}$. We have used the data taken at the Stanford Linear Accelerator Center (SLAC), from the SLAC Large Detector (SLD), which records the products of e^+e^- interactions at a center of mass energy $\sqrt{s} = 91.2$ GeV at the SLAC Linear Collider (SLC). The unique features of the SLC/SLD experimental apparatus provide interesting tests of the electroweak and the QCD physics. The small, stable SLC beam spot, and the precise tracking capability of the SLD allow the isolation of light flavor events. Charged hadrons are identified over wide momentum range with the Cherenkov Ring Imaging Detector (CRID). High momentum charged kaon, $\Lambda^0/\bar{\Lambda}^0$, and K_s^0 are used to select $Z^0 \to s\bar{s}$ events and to identify the s-quark direction. The averaged polarization was 63.0% in 1993 SLD run and 77.3% in 1994-95 run. We obtained $A_s = 0.86 \pm 0.17(stat.) \pm 0.10(syst.)$. This value is consistent with the prediction from the Standard Model and with the values of A_b measurements from SLD and LEP experiments.

Acknowledgements

First, I'd like to thank my advisor, Haruo Yuta. He gave me a chance to join the SLD experiment. His suggestions are always quite essential and he has told me what are important things for a physicist.

Special thanks to Dave Muller, whose guidance and suggestions lead me to finishing up this thesis. He has answered my great deal of questions over many subjects. My thanks go to CRIDers with whom I have spent the most time since I joined the SLD experiment. Dave Aston has told me a principle of the CRID and solved the problems on offline study. Tom Pavel also gave me many suggestions in my CRID study. Sometimes, he solved our computer problems. Thanks to Blair Ratcliff, who is a group leader, for his suggestions. Hide Kawahara has taught me the hardware of the CRID. I would like to thank Lillian DePorcel, Jennifer Chan, and other Group B secretaries in the past few years. I had stayed at SLAC quite comfortably by their help.

Thanks to Phil Burrows, Ken Baird, and Hiro Masuda. They gave me many useful comments on my analysis. I really appreciate for their kindness. I'd like to thank Takashi Akagi who gave me suggestions on physics and also told me how wonderful the American life is. We drunk almost every Friday night. Thanks to Kenji Abe. Many questions have been solved by discussion with him.

I'd like to thank my colleagues in Tohoku, Koya Abe, Tadashi Nagamine, Fumihiko Suekane, Kazushi Neichi, Takayuki Matsumoto, Syuichiro Hatakeyama, Hiroyuki Kawasaki, Masayuki Koga, and Kyoko Tamae for their encouragement and assistance. Special thanks to Kazumi Hasuko and Jun Yashima. I enjoyed myself staying at SLAC with them.

Finally, I want to thank my parents. I have been able to concentrate on my study with

their continuous help and supports. I'm very sorry I can't tell the completion of this thesis to my father. He passed away just a month ago, but I never forget his love. I'd like to express my gratitude to my brother and sister. They also have encouraged me.

Thanks to all !

Contents

List of Tables

List of Figures

Chapter 1

Introduction

The fermion production asymmetry A_f at the Z^0 pole, which is defined by the combination of vector and axial vector couplings, express the parity violation in the $Zf\bar{f}$ coupling. This parity violation originates from the difference of the strength between the couplings of left-handed fermion and right-handed fermion to the Z^0 boson. For heavy quarks, c and b, A_c and A_b have been well measured in SLC/SLD and LEP experiments, and the experimental precisions of these results are still being improved [1].

In the Standard Model, s quark is expected to have the same parity violating parameter as b quark. If one can measure the parity violating parameter for s quark, A_s precisely, the universality of the coupling constants can be examined by comparing with the measured A_b. However, A_s has not been measured well in contrast to heavy quarks asymmetries. The events $Z^0 \to c\bar{c}, b\bar{b}$ are selected by using the feature of decay of D or B meson. For light flavor events ($Z^0 \to u\bar{u}, d\bar{d}, s\bar{s}$), however, it is more difficult to specify the initial quarks because the final state hadrons can contain any light quarks in the selected events. One of the most important stages of this analysis is to select pure $s\bar{s}$ events as much as possible. Many fragmentation models predict that particles with the highest momentum among particles produced from the fragmentation process tend to carry the primary quark information. Therefore, the selection of a pure sample of high momentum strange particles are expected to provide a cleaner tagging of $Z^0 \to s\bar{s}$ events. Thus, this allows the better A_s measurement giving an interesting test of the electroweak interaction as well as the strong interaction.

The DELPHI collaboration reported the measurement of the forward-backward asym-

metry of strange quarks at the Z^0 pole [2]. They selected charged kaon and Λ^0 samples and obtained s-quark with 43% purity. [1] From those sample, the average s-quark forward-backward asymmetry was found to be $0.131 \pm 0.035(stat.) \pm 0.013(syst.)$. They also measured the forward-backward asymmetry for the unresolved d- and s- quark sample using high energy neutrons or neutral kaons tagged in the hadron calorimeter. The combined d- and s-quark purity was 69% and the asymmetry was found to be $0.112 \pm 0.031(stat.) \pm 0.054(syst.)$. These values themselves are consistent with Standard Model prediction. Because they used unpolarized electron beams and can only measure the forward-backward asymmetry which is the production of the asymmetries at both the Z^0 production and decay vertices, A_s is obtained indirectly from the forward-backward asymmetry.

In SLC/SLD experiment, the availability of polarized electron beam enables to obtain the parity violating parameter directly from the measurement of the cross sections of $Z^0 \to q\bar{q}$ for left-handed and right-handed electron beam.

The measurement described in this thesis is performed at the Stanford Linear Accelerator Center (SLAC), using about 150,000 hadronic Z^0 decays collected in 1993-1995 with the SLAC Large Detector (SLD) at the Stanford Linear Collider (SLC). The SLD is equipped with some powerful tools for studying electroweak physics and the theory of strong interaction (Quantum Chromodynamics : QCD). The small, stable beams of the SLC, and the precision tracking performance of SLD allow to separate light and heavy flavor events. The SLD has the excellent charged hadron identification device, the Cherenkov Ring Imaging Detector (CRID), which gives high identification efficiency over a wide track momentum range.

This thesis presents a direct measurement of A_s from the polarized forward-backward asymmetry of s-quark production in e^+e^- collision at $\sqrt{s} = 91.2$ GeV. In this analysis, charged kaon, $\Lambda^0/\bar{\Lambda}^0$, and K_s^0 are tagged for the $s\bar{s}$ event selection. The CRID is used to tag high purity charged kaons and protons.

The data used for this thesis comes from the SLD experiment. The SLD experiment has been carried out under an international collaboration which consists of about 200 physicists from 26 institutes. Tohoku university and Nagoya university have been participating since

[1] Estimated using the JETSET fragmentation model. The model-dependence in this estimate is a limitation of such analysis, especially when purity is so low

1988 under Japan-United States scientific cooperative project. The Tohoku group is involved to construct the CRID and the new vertex detector, VXD3.

This thesis is organized as follows: Chapter 2 contains a brief overview of physics in e^+e^- annihilation at the Z^0 pole and theoretical background of A_s measurement. Then we discuss the accelerator and detector apparatus in Chapter 3. The generator and detector simulation for SLD Monte Carlo data is discussed in Chapter 4. Chapter 5 discusses the barrel portion of the CRID more in detail, its components and structure, offline alignment study, particle identification method, and finally its performance. Chapter 6 introduces the SLD triggers, hadronic event selection criteria, and the flavor tagging technique which is used to select light flavor events in this analysis. Then, Chapter 7 discusses tags of strange particles used for $s\bar{s}$ event selection. In Chapter 8, pure $s\bar{s}$ events tag, the inclusive properties of jets initiated by s-quarks, and calculation of the polarized forward-backward asymmetry are described here. Here the systematic error estimation is also discussed. Finally, the experimental results are summarized in Chapter 9.

Chapter 2

Physics in $e^+e^- \rightarrow Z \rightarrow f\bar{f}$

In this chapter, we discuss the physics of e^+e^- annihilation at the Z^0 pole focusing on the electroweak and strong interactions.

2.1 Framework of Electroweak Theory

The Standard Model of electroweak interaction is based on the $SU(2)_L \times U(1)$ group, where the $SU(2)$ symmetry arises in "weak isospin" space and the $U(1)$ asymmetry arises in "weak hypercharge" space. The $SU(2)$ group is generated by a vector triplet, $\mathbf{W}_\mu = (W^1_\mu, W^2_\mu, W^3_\mu)$, and the $U(1)$ is generated by the singlet, B_μ. These generators may be thought of as massless vector bosons, which are not eigenstates of the electroweak interaction. A process known as spontaneous symmetry breaking is invoked by way of the "Higgs mechanism". The broken symmetry gives rise to physical bosons which are linear combinations of the group generators,

$$W^\pm_\mu = \frac{1}{\sqrt{2}}\left(W^1_\mu \pm iW^2_\mu\right), \tag{2.1}$$

$$Z_\mu = \frac{gW^3_\mu - g\prime B_\mu}{\sqrt{g^2 + g'^2}}, \tag{2.2}$$

$$A_\mu = \frac{g'W^3_\mu + gB_\mu}{\sqrt{g^2 + g'^2}}, \tag{2.3}$$

where $W^\pm_\mu$ are the charged massive bosons, Z_μ is the neutral massive boson, A_μ is the massless photon. The $W^\pm$, Z^0 and all of the fermions acquire mass through self-interaction terms provided by the Higgs field. A consequence of the Higgs mechanism is the prediction

of one or more massive Higgs bosons, which have not been observed yet experimentally.

The hypercharge and isospin fields are "mixed". The magnitude of the mixing is defined by the coupling g and g' in the following manner:

$$g = \frac{e}{\sin\theta_w}, \quad g' = \frac{e}{\cos\theta_w}, \tag{2.4}$$

where e is the magnitude of the charge of the electron and the parameter θ_w is known as the weak mixing angle.

The portion of the electroweak Lagrangian which describes the interaction between fermions and the gauge bosons is written by,

$$\begin{aligned} \mathcal{L} &= \frac{e}{\sin\theta_w \cos\theta_w}(J^3_\mu - \sin^2\theta_w J^{e.m.}_\mu)Z_\mu \\ &+ \frac{2}{\sqrt{2}\sin\theta_w}(J^-_\mu W^+_\mu + J^+_\mu W^-_\mu) \\ &+ eJ^{e.m.}_\mu A_\mu, \end{aligned} \tag{2.5}$$

where J_μ are the fermion currents. The first term of Eq (2.5) is the weak neutral current interaction (Z^0 exchange), the second term is the weak charged current interaction ($W^\pm$ exchange), and the third term is the electro magnetic interaction (γ exchange).

In the electroweak sector of the Standard Model, the tree level process can be described with three parameters; they are g (the $SU(2)$ coupling constant), g' ($U(1)$ coupling constant), and v which is the vacuum expectation value of the Higgs field. However, none of these parameters are directly accessible experimentally. In stead, we can define three combinations of them which can be measured experimentally, that is, α, G_F, and M_Z. They are formed by,

$$\alpha \equiv \frac{e^2}{4\pi} = \frac{gg'}{4\pi\sqrt{g^2+g'^2}} \tag{2.6}$$

$$G_F = \frac{1}{\sqrt{2}v^2} \tag{2.7}$$

$$M_Z = \frac{\sqrt{g^2+g'^2}v}{2}. \tag{2.8}$$

The values of these parameters [3] are shown in Table 2.1.

Parameter	Measured value
α	1/137.0359895(61)
G_F	$1.16639(2) \times 10^{-5}$ (GeV)$^{-2}$
M_Z	91.187(7) GeV/c^2

Table 2.1: The parameters which specify the electroweak Standard Model at tree level.

2.2 Z^0 Production and Decay

In the process $e^+e^- \rightarrow f\bar{f}$, two neutral gauge bosons can be exchanged, namely γ, Z, as shown in Figure 2.1. The cross section is proportional to the square of the sum of the two matrix elements, $\mathcal{M}_Z$ and $\mathcal{M}_\gamma$, and given by

$$\frac{d\sigma}{d\cos\theta} = \frac{1}{64\pi^2 s}|\mathcal{M}_\gamma + \mathcal{M}_Z|^2, \tag{2.9}$$

where θ is the scattering angle and s is the square of the center of mass energy. Figure 2.2 shows the total cross section for $e^+e^- \rightarrow \mu^+\mu^-$ as a function of $\sqrt{s}$. The large resonance peak is observed around the Z^0 which arises from the Z^0 exchange process, whereas the long-tail contribution comes from the γ exchange process. At $\sqrt{s} = 91.2$ GeV, the contribution from the Z^0 exchange is ~ 800 times that from the γ exchange. Therefore, pure photon-exchange term can be neglected. In addition, the $\gamma - Z$ interference term is also very small and negligible at the Z^0 pole. This leaves only the pure Z exchange. In the case of a polarized electron beam, the tree-level differential cross section for $e^+e^- \rightarrow f\bar{f}$ at the Z^0 pole is given by [4],

$$\frac{d\sigma_f}{dcos\theta} = K(v_e^2 + a_e^2)(v_f^2 + a_f^2)[(1 - A_e P_e)(1 + cos^2\theta) + 2A_f(A_e - P_e)cos\theta], \tag{2.10}$$

where θ is the fermion polar angle, P_e is the signed longitudinal polarization of electron, and v_f and a_f are the vector and axial vector couplings to Z^0 (v_e and a_e are the electron couplings to Z^0). They are defined in terms of the weak mixing angle θ_w, Q_f, and T_f^3 as;

$$\begin{aligned} v_f &= T_f^3 - 2\sin^2\theta_w Q_f, \\ a_f &= T_f^3, \end{aligned} \tag{2.11}$$

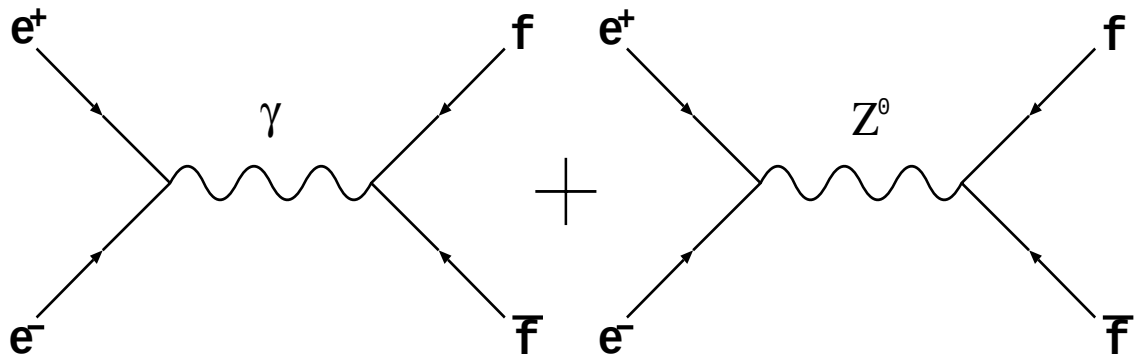

Figure 2.1: The tree level diagrams for $e^+e^- \to f\bar{f}$

where Q_f and T_f^3 are the charge and the third component of weak isospin of the fermion. The quantity A_f corresponds to the cross section asymmetry parameter and is defined for fermion, f by

$$A_f \equiv \frac{2v_f a_f}{v_f^2 + a_f^2}. \tag{2.12}$$

The deviation of A_f from zero is a measure of the parity violation in the $Zf\bar{f}$ coupling. The coefficient, K in Eq (2.10) is given by,

$$K = \frac{\alpha^2}{4\sin^4 2\theta_w} \frac{s}{(s - M_z^2)^2 + \Gamma_z^2 s^2/M_z^2}, \tag{2.13}$$

with α being the electromagnetic fine structure constant. M_z and Γ_z are the mass and total decay width of the Z^0, respectively. Table 2.2 lists the vector, axial vector couplings to the Z^0, and A_f for leptons and quarks calculated in the Standard Model.

2.3 Electroweak asymmetries

The electroweak asymmetry is the ratio of cross sections where the parameter of interest has been isolated by the angular- or polarization-dependence of the differential cross section. This has the advantage that errors inherent in determining the absolute cross section, such as those due to luminosity normalization and absolute detection efficiency, cancel in the asymmetry which is formed. Using this method allows the isolation and examination of

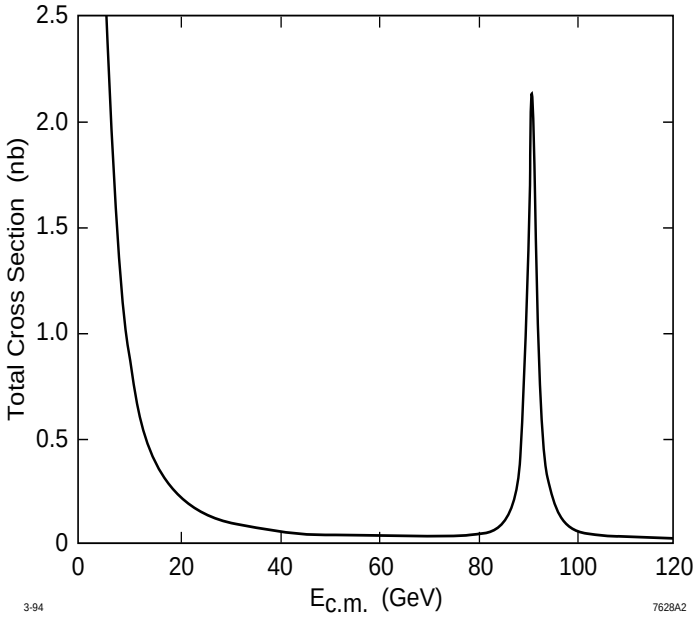

Figure 2.2: The total cross section for $e^+e^- \to \mu^+\mu^-$ v.s. center of mass energy.

fermion	a_f	v_f	A_f
ν_e, ν_μ, ν_τ	$\frac{1}{2}$	$\frac{1}{2}$	1
e, μ, τ	$-\frac{1}{2}$	$-\frac{1}{2} + 2\sin^2\theta_w$	0.155
u, c, t	$\frac{1}{2}$	$\frac{1}{2} - \frac{3}{4}\sin^2\theta_w$	0.667
d, s, b	$-\frac{1}{2}$	$-\frac{1}{2} + \frac{2}{3}\sin^2\theta_w$	0.935

Table 2.2: The vector and axial vector couplings for the fermion to the Z^0. The values of A_f are calculated with $\sin^2\theta_w = 0.232$.

various electroweak couplings. In the following, the asymmetries related with this work will be described.

2.3.1 The Left-Right Asymmetry

The simplest example of the asymmetry which can be formed for an experiment with a polarized electron beam is the left-right asymmetry A_{LR} which measures the asymmetry at the initial vertex. The left-right asymmetry A_{LR} is given by,

$$A_{LR} = \frac{\sigma_L - \sigma_R}{\sigma_L + \sigma_R}, \tag{2.14}$$

where σ_L and σ_R are the total Z^0 cross section for left-handed and right-handed electron beams respectively. A_{LR} is directly related to the weak mixing angle $\sin^2\theta_w$. From Eqs (2.10) and (2.11) with $|P_e| = 1$,

$$A_{LR} = A_e = \frac{2v_e a_e}{v_e^2 + a_e^2} = \frac{2[1 - 4\sin^2\theta_w^{eff}(M_Z^2)]}{1 + [1 - 4\sin^2\theta_w^{eff}(M_Z^2)]}. \tag{2.15}$$

where θ_w^{eff} is "$effective$" weak mixing angle [5] which includes the QED effects of initial-state radiation. For the arbitrary beam polarization $|P_e|$,

$$A_{LR}^{meas} = |P_e| A_e = |P_e| \frac{N_L - N_R}{N_L + N_R}, \tag{2.16}$$

where A_{LR}^{meas} is the measured asymmetry, given by the difference between the number of Z^0 events produced with left-handed electron beam (N_L) and the number produced with a right-handed electron beam (N_R) over the total Z^0 events. As seen from this expression, the higher the beam polarization, the larger the asymmetry. For $P_e = 1$, the expected value of A_{LR} is about 0.16.

One of the advantages of this asymmetry is that there is no dependence on the final state fermion couplings. This implies that all final state, except the e^+e^- final[1], can be used to measure A_{LR} which greatly increases the statistical precision power of the measurement. Another advantage of this measurement is that it is very insensitive to the details of the detector. As long as its detection efficiency of fermions is the same as that for antifermions at each value of $\cos\theta$, the efficiency effects should be canceled in the ratio, because the Z^0

[1]Because of contributions from t-channel Bhabha scattering.

decays into a back-to-back fermion-antifermion pair and the detector was designed to be symmetric about its midplane perpendicular to the beam axis. In addition, A_{LR} is very sensitive to the value of $\sin^2\theta_w^{eff}$, because we have $\delta \sin^2\theta_w^{eff} = \delta A_{LR}/7.84$ obtained from Eq (2.15).

2.3.2 The Forward-Backward Asymmetry

The differential cross section in Eq (2.10) has a term which is asymmetric in polar angle, leading to a difference of cross sections for Z^0 decays between the forward and backward hemispheres. The fermion forward-backward asymmetry A_{FB}^f is defined by

$$A_{FB}^f = \frac{\sigma_F^f - \sigma_B^f}{\sigma_F^f + \sigma_B^f} = \frac{3}{4} A_e A_f, \tag{2.17}$$

where

$$\sigma_B = \int_{-1}^{0} \frac{d\sigma}{d\cos\theta} d\cos\theta, \tag{2.18}$$

and

$$\sigma_F = \int_{0}^{1} \frac{d\sigma}{d\cos\theta} d\cos\theta. \tag{2.19}$$

This asymmetry is proportional to the product of initial- and final-state coupling asymmetries and is caused by parity violation at both the production and decay vertices.

One disadvantage of the definition of A_{FB}^f is that the cross sections integrated over $\cos\theta$, are affected by inefficiency of acceptance at large values of $|\cos\theta|$. A more ideal form involves finding the forward-backward asymmetry as a function of $|\cos\theta|$ and is given by

$$A_{FB}^f(|\cos\theta|) = \frac{\sigma_F^f(\cos\theta) - \sigma_B^f(-\cos\theta)}{\sigma_F^f(\cos\theta) + \sigma_B^f(-\cos\theta)} = A_e A_f \frac{2|\cos\theta|}{1+\cos^2\theta}. \tag{2.20}$$

With this formulation, the detector acceptances in the numerator and denominator could cancel in the formed asymmetry, if the $\cos\theta$ binning is taken small enough.

The availability of one polarized beam enables to form a double asymmetry, so-called left-right forward-backward asymmetry or polarized forward-backward asymmetry $\tilde{A}_{FB}^f$ [6]:

$$\tilde{A}_{FB}^f = \frac{\sigma_{FL}^f - \sigma_{FR}^f - \sigma_{BL}^f + \sigma_{BR}^f}{\sigma_{FL}^f + \sigma_{FR}^f + \sigma_{BL}^f + \sigma_{BR}^f}, \tag{2.21}$$

where L and R refer to the helicity of the incident electron beam; F and B stand for "forward" and "backward". If the electron beam has polarization P_e, then this asymmetry can be expressed in terms of the coupling asymmetry using Eq (2.10):

$$\tilde{A}_{FB}^{f} = \frac{3}{4}|P_e|A_f. \tag{2.22}$$

This longitudinally polarized beam has one advantages of forming the double asymmetry in which the Z^0 production asymmetry caused by the parity violation in the initial state coupling has been cancelled, leaving experimentally accessible quantities in the final state coupling. In addition, for substantial net beam polarization, the raw asymmetry $\tilde{A}_{FB}^{f}$ becomes quite large compared to the regular forward-backward asymmetry A_{FB}^{f}, since P_e can, in principle, be ~ 1, whereas $A_e \sim 0.16$. This makes a smaller fractional error on the measurement of $\tilde{A}_{FB}^{f}$ compared with that for A_{FB}^{f} for a given data sample.

2.4 Production of Hadrons in e^+e^- Collisions

For A_s measurement, we need to select the sample of the $Z^0 \to s\bar{s}$ events from tagged hadrons. In such a case, the question is how often the final state hadrons can carry the information of primary quark from Z^0 decay correctly. To answer the question, Figure 2.3 shows a conventional view of the reaction $e^+e^- \to hadrons$. In stage (i), the initial quark-antiquark pairs are produced in the Z^0 decay. This stage can be calculated from electroweak physics. In stage (ii), parton shower develops and perturbative QCD can be used to calculate this stage. In stage (iii), the partons (quarks or gluons) become bound into colorless hadrons. This stage is known as hadronization or fragmentation, which is fundamentally a non-perturbative part in QCD. In the final stage (iv), the hadrons are produced in stage (iii) decay to lighter hadrons. In the following section, we focus on the fragmentation process. The process exhibits the characteristic feature of hadronic Z^0 decays. For example, the large number of hadrons appearing in the detector travel in largely the same direction as the original quarks. Therefore, the hadrons are, more or less, thought to carry the information of initial quark pairs and the translation of the quark information into hadrons depends on fragmentation process. For specifying initial quark flavor, it is important to understand the fragmentation.

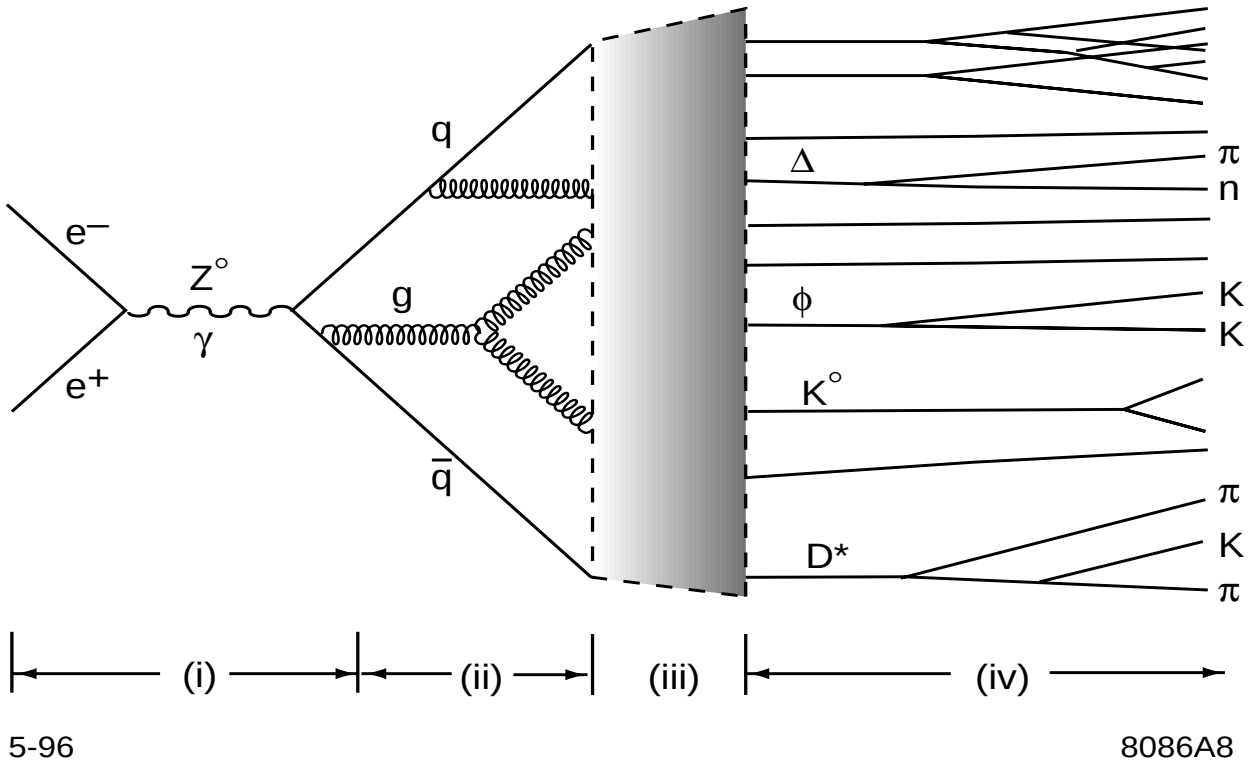

Figure 2.3: The stages of typical $e^+e^- \rightarrow$ hadrons interaction.

2.4.1 Fragmentation Models

The fragmentation process can not be calculated perturbatively. So far, there is no complete theoretical treatment of the non-perturbative process of fragmentation that derives from QCD. Therefore, we necessarily rely on fragmentation models, which have been tested against a large number of experimental data.

There exist three major classes of the fragmentation models, which are widely used by current high energy physics experiments;

- Independent Jet models,
- String Fragmentation models,
- Cluster Fragmentation models.

Among these, the string model incorporated in the JETSET Monte Carlo simulation is tuned

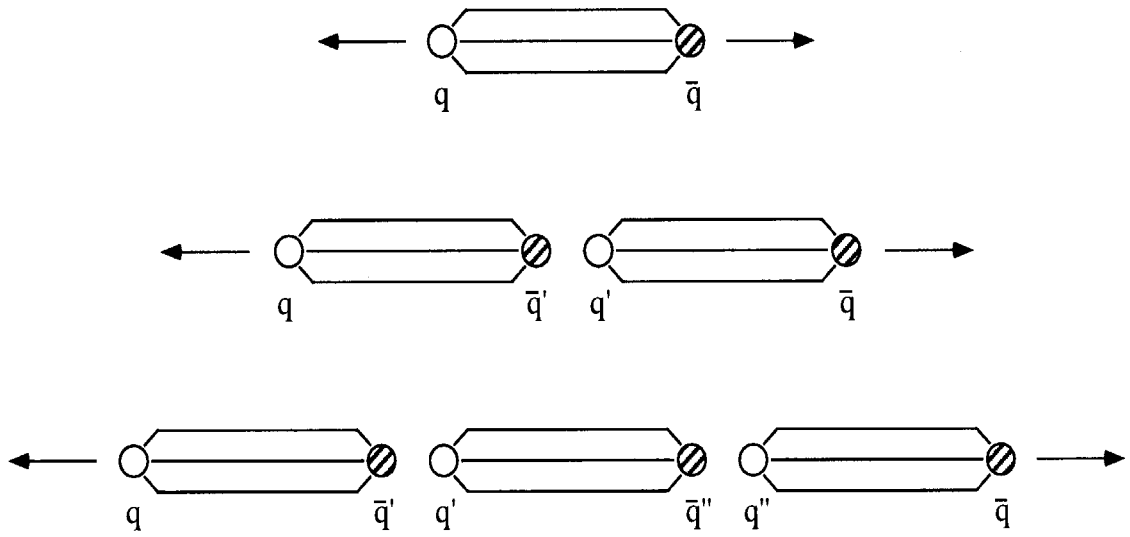

Figure 2.4: A color tube (string) stretching between q and $\bar{q}$. as the q and the $\bar{q}$ separate, the potential energy in the string increases. When this energy is above threshold for creating a $q'\bar{q}'$, the string may break.

best with LEP and other experimental data. Thus, we have used the JETSET Monte Carlo in this analysis. In the following, we focus on the string fragmentation model. Detailed descriptions of independent fragmentation models and cluster fragmentation models can be found in [7, 8]

The string fragmentation model was first introduced in a Monte Carlo model by Artru and Mennessier [9], and extended in the popular JETSET event generator of Andersson, Gustafson, and Sjöstrand at Lund University [10, 11]. In the string fragmentation model, the primary partons move apart, a color flux tube stretches between them. Consider the field lines connecting two color charges (Figure 2.4). This is analogous to the electromagnetic field lines connecting two electrically charged objects. However, due to the coupling between gluons, the field lines are pulled together to form a color "string" between the two partons. If the string has a constant energy density per unit length (estimated to be $\sim$ 1 GeV/fm) then the potential energy of the string rises linearly as the color charges are separated. Once

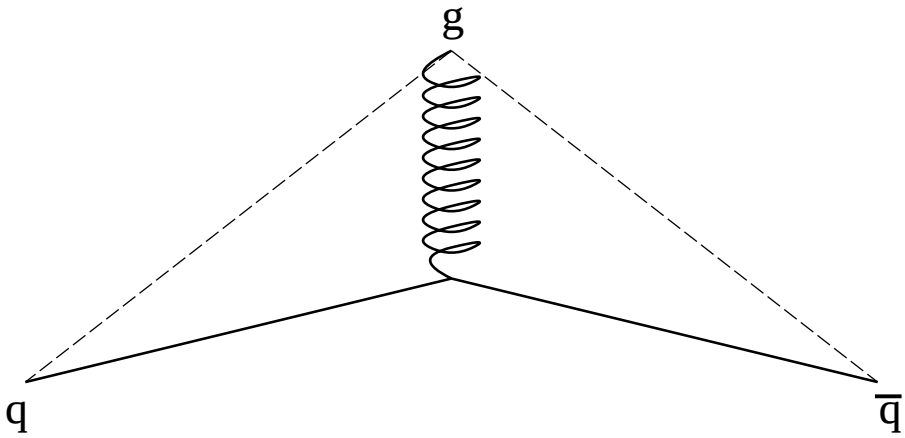

Figure 2.5: The string model for a $q\bar{q}g$, with the g causing a "kink" in the string

the potential energy has grown sufficiently to produce $q\bar{q}$ pairs, the string breaks to form two separate string objects. This break typically occurs when the string is 1-5 fm long in its rest frame [12]. If the invariant mass of a string object is large enough (i.e. $\geq$ hadron mass), further breaks may occur until ordinary hadrons remain. Actually, massive quarks must be produced some distance apart so that the field energy between them can be transformed into mass and transverse momentum. This can be accomplished by creating them at a point allowing them to "tunnel" quantum mechanically out to the allowed region. This tunneling process occurs with a probability proportional to [12]

$$P = e^{-\frac{\pi m_T^2}{\kappa}} \tag{2.23}$$

where κ is the string constant and $m_T^2 = m^2 + p_T^2$ with quarks mass of m and transverse momentum of p_T. This formulation serves to generate the transverse momentum spectrum of hadrons relative to the original quark direction, and gives by virtue of the relative quark masses the flavor composition of $q\bar{q}$ pairs created when the string is broken. For example, charm quarks are suppressed by a factor of $\sim 10^{-11}$ relative to the light u and d quarks and are essentially never produced in the string breakup.

The gluon is treated as a "kink" in the string that is stretched between the two quarks (see Figure 2.5). This makes sense intuitively, since the gluon carries two color charges.

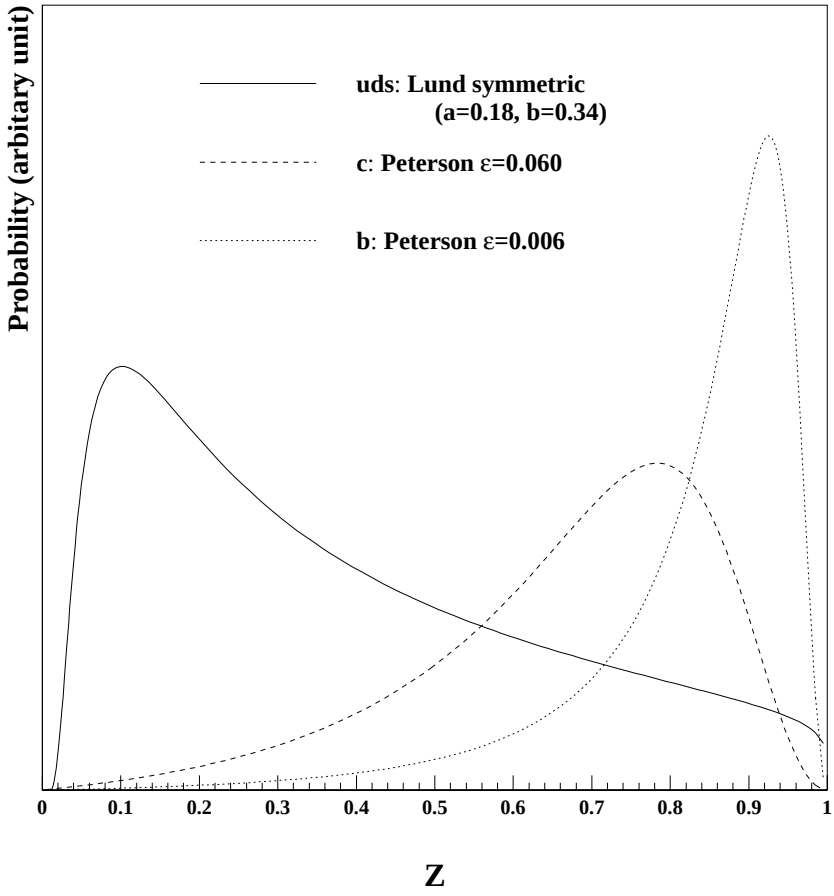

Figure 2.6: The fragmentation functions for uds, c, and b. The value of m_T in the Lund fragmentation function is chosen to be 300 MeV/c^2.

2.4.2 Fragmentation Functions

The fragmentation function is the probability for a second string to be formed, in other words, the probability which governs the sharing of energy between the daughter hadron and the remnant jet that remains as the fragmentation process is in progress.

In light-quark (uds) events, the fragmentation function $f(z)$ is well described by the Lund symmetric function, which can be derived by requiring the left-right symmetries involved in breaking a string starting at the quark or antiquark side,

$$f(z) \propto \frac{1}{z}(1-z)^a e^{-\frac{bm_T^2}{z}}, \tag{2.24}$$

where $z = 2E(hadron)/\sqrt{s}$, a and b are the parameters which must be determined from experimental data. The measured parameters a and b typically have values of 0.18 and 0.34 GeV^{-2} [13].

Although this Lund symmetric function has been very successful at a wide momentum range, it does not describe heavy flavor production very well. The actual fragmentation for c and b quarks occurs in much harder than that for the light flavors since the heavy hadron carries a larger fraction of the available energy. For $c\bar{c}$ and $b\bar{b}$ events so-called Peterson function is often used;

$$f(z) \propto \frac{1}{z(1-(1/z)-\epsilon/(1-z))^2}, \tag{2.25}$$

with the parameter ϵ chosen to be 0.060 for c quarks, and 0.006 for b quarks [13].

These fragmentation distributions are shown in Figure 2.6.

2.4.3 Leading Particle Effect

The leading particle is defined to be the fastest final state hadron which is supposed to carry the consistent property with primary quark and tends to have a sizable fraction of the energy of the resulting jet [14]. In the JETSET Monte Carlo simulation, the leading effect can be predicted. For example, Figure 2.7 shows the ratio of the number of charged kaon in $s\bar{s}$ events to the total number of charged kaon as a function of kaon momentum. Obviously, the fraction of $s\bar{s}$ events increases as momentum. Moreover, Figure 2.8 shows the analyzing

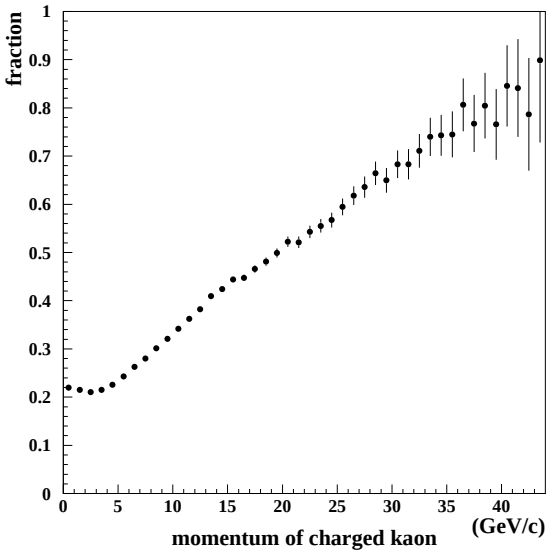

Figure 2.7: The fraction of $K^{\pm}$ at a given momentum in Z^0 generated by that are from $s\bar{s}$ events.

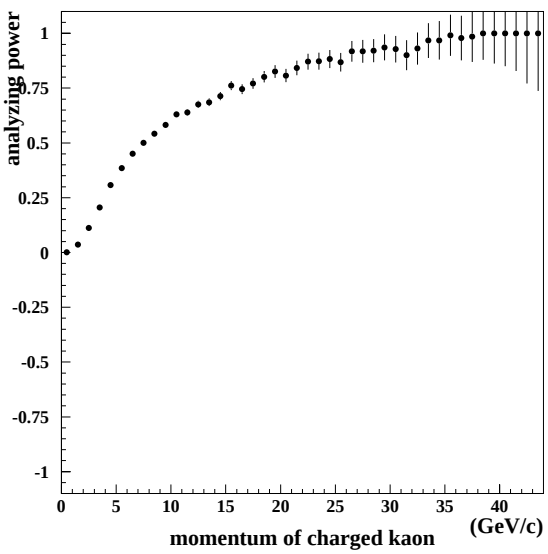

Figure 2.8: The analyzing power for $K^{\pm}$ which is interpreted to the fraction of K^- from s quark. This is calculated in the JETSET model.

power α as a function of momentum, defined by

$$\alpha \equiv \frac{N^{K^- \leftarrow s} - N^{K^- \leftarrow \bar{s}}}{N^{K^- \leftarrow s} + N^{K^- \leftarrow \bar{s}}}, \tag{2.26}$$

where $N^{K^- \leftarrow s(\bar{s})}$ is the number of K^- from $s(\bar{s})$. This implies that K^- is likely to come from s quark rather than $\bar{s}$ quark. This is a quite useful property which allows to determine the initial quark direction by the strangeness of tagged strange particle. In e^+e^- experiments, the leading particle effect in $c\bar{c}$ and $b\bar{b}$ events have been studied by observing the multiplicities and the longitudinal momentum fraction of the heavy hadrons [15]. In light flavor events, it has been studied [16] using the tagged light quark (and antiquark) jets by utilizing the large electroweak production asymmetry in polar angle induced by the electron beam polarization. In the previous measurement at the SLD, an excess of Λ over $\bar{\Lambda}$, and an excess of p over $\bar{p}$ were observed in the light quark jets. These differences increase with the increasing momentum, and can be considered as direct evidence of the leading particle hypothesis that faster baryons are more likely to contain the primary quark. The analysis also showed there is no such

difference between π^- and π^+ production. For kaons, a significant excess of K^- over K^+ was observed, indicating that a fast kaon is likely to contain a primary quark (or antiquark) from the Z^0 decay, and that leading $K^\pm$ are produced predominantly in $s\bar{s}$ events rather than $u\bar{u}$ events. This makes it possible to study A_s.

Chapter 3

Experimental Apparatus

The data used in this analysis was collected at the Stanford Linear Accelerator Center (SLAC) in Stanford, California. The SLAC Linear Collider (SLC) is the unique e^+e^- collider that produces longitudinally-polarized Z^0's. The SLAC Large Detector (SLD), placed at the interaction region, is a multi-purpose device for measuring the properties of the decay products of the Z^0 boson. This chapter presents an over view of the main features of the SLC and the SLD.

3.1 The SLAC Linear Collider

The SLC is the world's first linear collider. The layout of the SLC is shown in 3.1. The electron beam starts from an electron gun containing a strained-lattice gallium-arsenide, which photon emits longitudinally polarized electrons when illuminated by circularly polarized laser light (described below).

At the start of each 120 Hz cycle, the polarized electron source produces two bunches of approximately 6×10^{10} electrons. These bunches, approximately 1 mm in length, are accelerated in the linac to 1.19 GeV and stored in the north damping ring of the SLC. Damping rings are used to compress the bunches and reduce energy fluctuations. Just before each electron bunch enters the damping ring, the polarization of the bunch is rotated from the horizontal(longitudinal) direction to the vertical direction. This is done so the electrons are not depolarized by the natural spin dynamics of the ring.

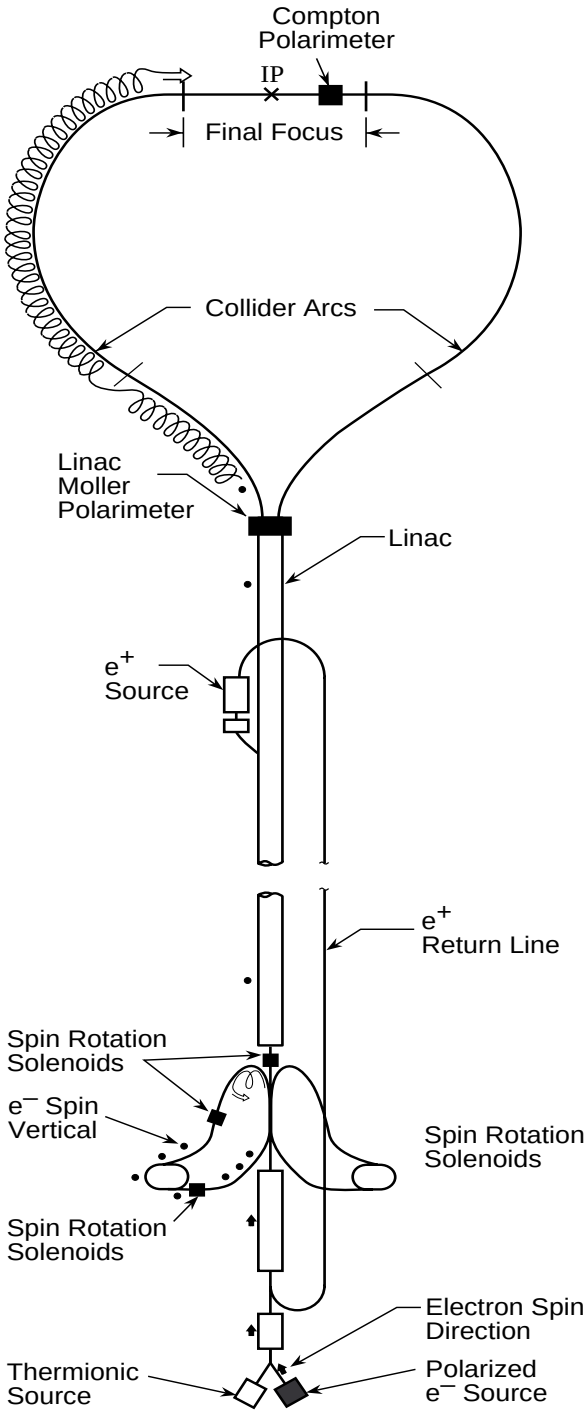

Figure 3.1: The SLC layout

After damping, the two electron bunches and a positron bunch are extracted from the damping rings and further accelerated by the linac. The positron bunch and the first electron bunch are both accelerated to 46.7 GeV and at the exit of the linac, are directed by dipole magnets into a pair of 1 km long arcs, after which they then intersect at the interaction point (IP) located in the center of the SLD. During their travels through the arcs, the electrons and positrons lose energy through synchrotron radiation, and by the time, the two bunches collide the mean energy per bunch $\sim$ 45.6 GeV.

The second electron bunch that is extracted from the damping ring is accelerated to 30 GeV and then diverted onto a Tungsten-Rhenium alloy target. The resulting shower is filtered for positrons, which are brought back to the front-end of the linac to be used in the next cycle.

In addition to the damping rings, the arcs also have the potential for depolarizing the electron bunch. To counteract this, the electrons are *launched* into the arcs with the polarization tilted to a specific angle. After spin precession, mostly due to coupling between vertical betatron oscillations and dipole bending, the electron bunch arrives at the IP longitudinally polarized. This launch angle is optimized to produce the best longitudinal polarization at the IP.

SLC has constantly improved its luminosity since it started producing Z^0 bosons in 1989, by a combination of shrinking beam waists at the collision point, increasing the electron and positron bunch populations, and increasing the reliability of operation. The reliability factor includes not only the fraction of the time the accelerator is on and delivering bunches to the IP, but also the fraction of the time it is optimally tuned. Feedback mechanism have greatly reduced the need to dedicate time to tuning the beams [17]. In addition, reduced deadtime from the SLD increased the effective luminosity. This was achieved by piplining the data acquisition, suppressing readout on beam crossing for which the detector was saturated with noise, buffering the logging stream, and streamlining the run switchover procedure. During the 1994-1995 run, typical luminosities achieved were 50-60 Z^0/hour, while in 1992, 30 Z^0/hour was more common. A history of the SLC luminosity for the time the SLD was running is shown in Figure 3.2.

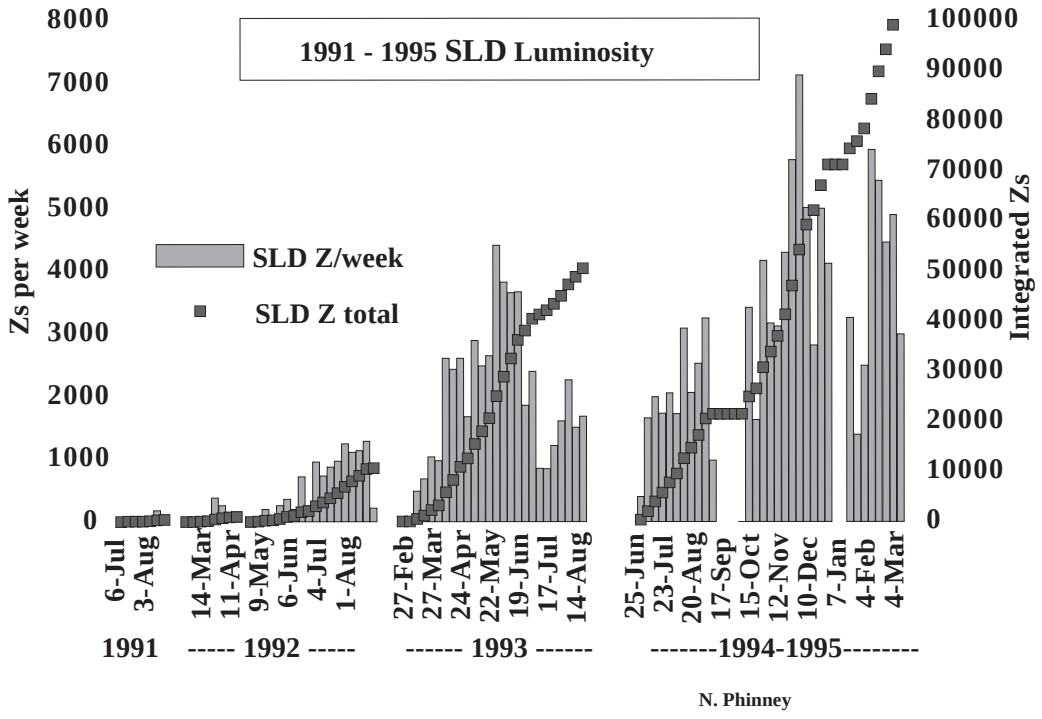

Figure 3.2: Luminosity history of SLC

3.1.1 Polarized electron source

The SLC has the unique capability of colliding longitudinally polarized electrons with positrons to produce polarized Z^0's. This is made possible by the use of Gallium-Arsenide(GaAs) photo-cathode in the electron gun[18]. Circularly polarized laser-light(from a Nd:YAG-pumped Ti:sapphire laser) is used to selectively excite electron transitions into longitudinally-polarized states in the conduction band. An energy state diagram is shown in Figure 3.3.

For the 1992 physics run, a bulk GaAs cathode was used. This cathode had a theoretical maximum polarization of 50%; the average polarization measured [19] was 22%. For the 1993 and 1994/95 runs, a strained-lattice cathode consisting of GaAs "grown" on a GaAsP (Gallium-Arsenide-Phosphide) substrate was used. This strained lattice had a theoretical maximum polarization of 100%, and for the 1993 run produced approximately 65% polarization at the source [20]. A still-newer cathode with an extremely thin layer of GaAs was

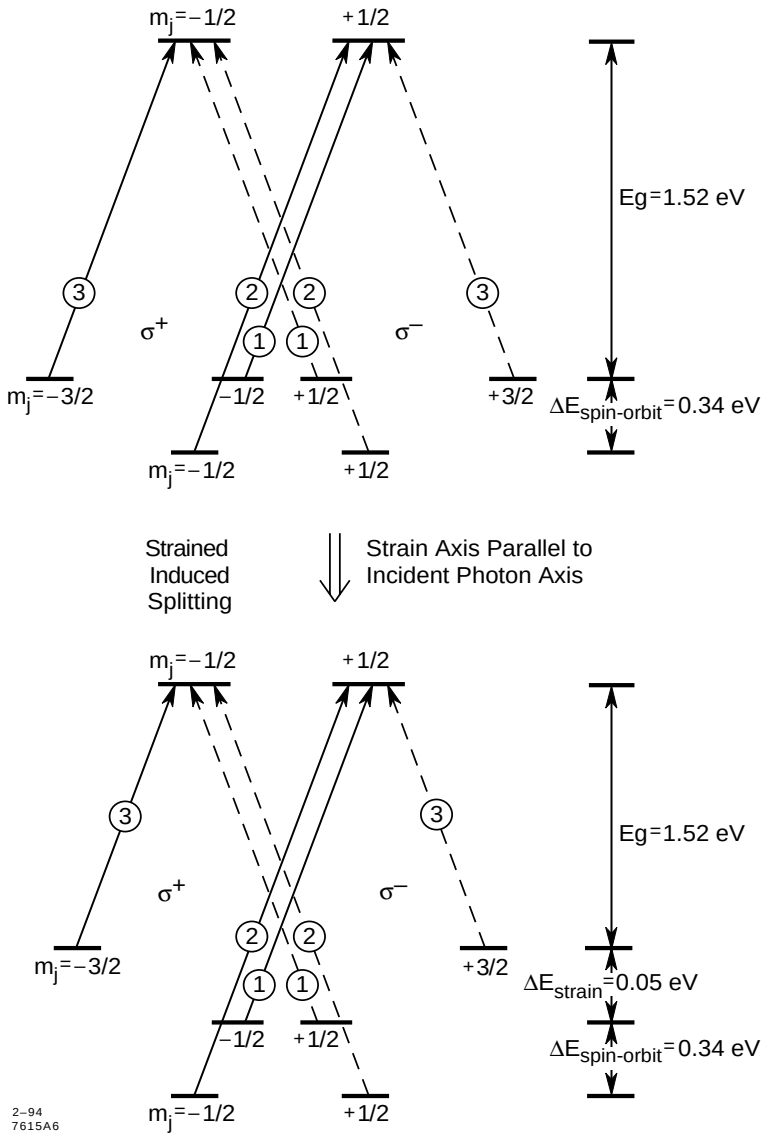

Figure 3.3: The energy state diagram for bulk GaAs(top) and the changes it undergoes when the lattice is strained (bottom). The polarization is due to the performance of certain excitation modes; the relative sizes of the matrix elements are shown in the circles. for the bulk GaAs, the maximum theoretical polarization is 50%. for the strained lattice, the maximum theoretical polarization is 100%.

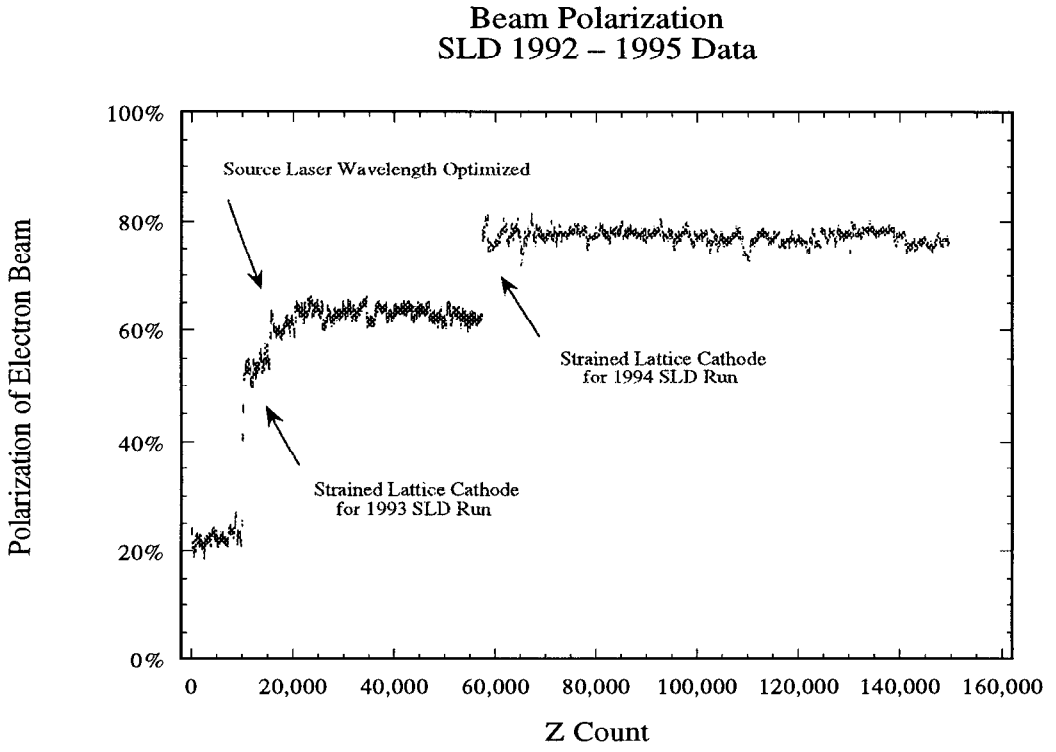

Figure 3.4: History of the electron beam polarization as a function of the count of collected Z^0s. Large discontinuities correspond to cathode changes for the different running years.

used for the 1994-95 physics run; it produced ~80% polarized electrons. The history of the polarization as a function of the count of collected Z^0 bosons is shown in Figure 3.4.

3.1.2 Beam Energy Measurement

The beam energy is measured on every pulse by two spectrometers that are placed just prior to the outgoing beam dumps where the spent beams arrive after the collision. The actual energy measurement is performed by deflecting each beam horizontally, then vertically by a precisely-calibrated bend magnet, then horizontally again. The horizontal bends produce two synchrotron radiation swaths whose positions are measured by the Wire Imaging Synchrotron Radiation Detector (WISRD) [22]. the vertical distance between the two stripes is inversely proportional to the beam energy, which can be extracted given the integrated field

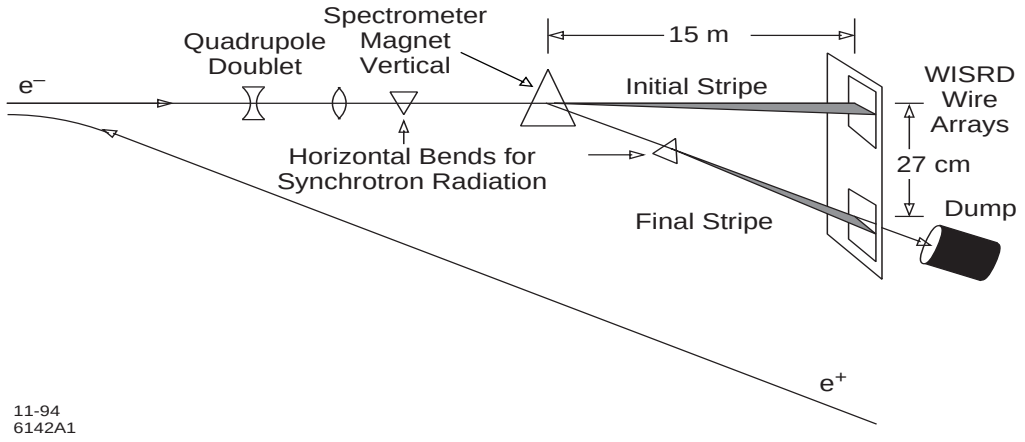

Figure 3.5: The Wire Imaging Synchrotron Radiation Detector (WISRD)

of the precision bend and the distance to the detector. A schematic view of the WISRD spectrometer is shown in Figure 3.5

3.1.3 Beam Poralization Measurement

It is important to measure the electron beam polarization as close to the interaction region as possible to reduce systematic error on asymmetry measurements, and to measure it continuously, so that a luminosity-weighted average may be performed. Two polarimeters are used to measure the electron polarization. A Compton polarimeter [23] provided the main measurement of the polarization during the run. There is a Møller polarimeter at the end of the Linac. This was only used as a cross-check at selected time. Therefore, we focus on a Compton polarimeter here.

The Compton polarimeter brings circularly polarized photons into collision with the SLC electron beam and measures the rate of Compton scattered electrons as a function of their energy. The polarimeter is shown schematically in Figure 3.6. It has two main components: a laser with polarizing optics, and an electron spectrometer. A circularly polarized laser beam is focussed onto the electron bunches just after they pass through the interaction point (approximately 30 m downstream). Polarized photons undergo Compton scattering

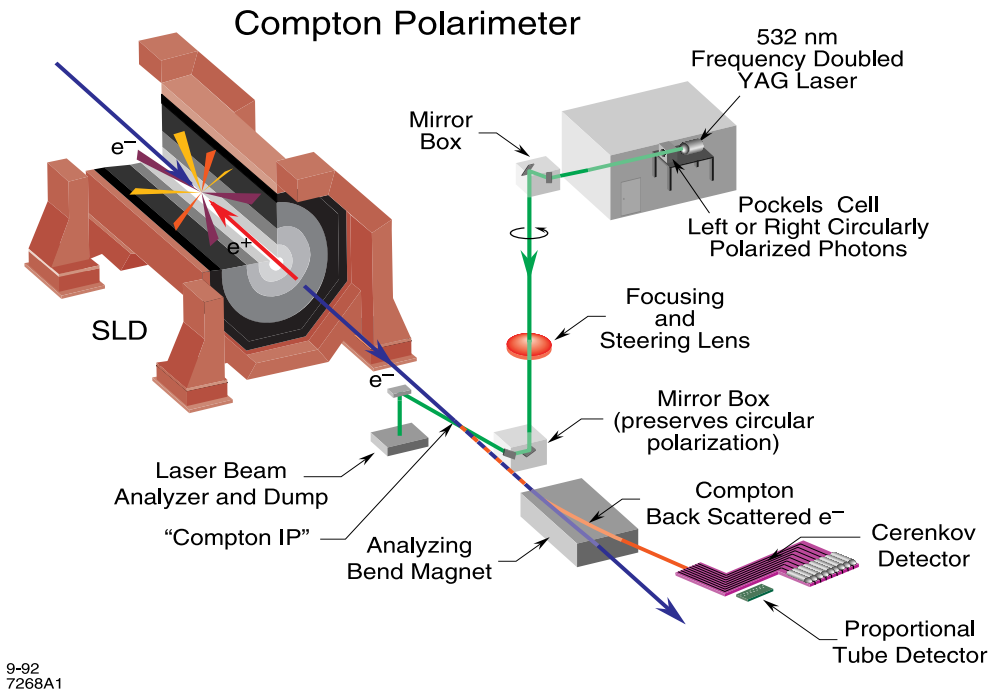

Figure 3.6: The compton polarimeter

with some of the electrons, causing them to lose momentum. Then, the electrons pass through a precision dipole magnet, where the scattered electrons are bent away from the main bunch. The momentum spectrum of the scattered electrons is determined by measuring their deflection angle with Cherenkov and proportional tube chambers.

The differential cross section for the Compton scattering of polarized electrons and polarized photons can be written as:

$$\frac{d\sigma}{dE} = \frac{d\sigma_u}{dE}[1 + P_\gamma P_e A_c(E)], \tag{3.1}$$

where σ_u is the unpolarized Compton scattering cross section, P_γ is the measured photon polarization, P_e is the unknown electron polarization, and A_c is the Compton asymmetry. The shape of this asymmetry A_c does not depend on the incident polarizations P_e or P_γ; it is only a function of the energy in the center-of-mass system and can be calculated from quantum electrodynamics. Thus, unknown electron beam polarization P_e can be extracted

from

$$A_m \equiv \frac{N^{obs}(J_z = \frac{3}{2}) - N^{obs}(J_z = \frac{1}{2})}{N^{obs}(J_z = \frac{3}{2}) + N^{obs}(J_z = \frac{1}{2})} = a_d P_\gamma P_e \, A_c(E), \tag{3.2}$$

where A_m is the observed asymmetry, N^{obs} represents the number of events observed in the two possible spin configurations, a_d is the analyzing power of the detector used to measure the scattered electron energy. This analyzing power depends on the transport optics of the electron beam from the Compton IP to the Compton polarimeter detectors.

One of the difficulties with the polarization measurement is that the polarization is measured at the Compton IP that is some 33 m downstream from the SLC IP. Because of the chromatic terms in the SLC final focus optics and the fact that spin-precession on the SLC arcs depends on electron energy, the measured polarization at the Compton IP is systematically different from the luminosity-weighted polarization at the SLC IP. In the 1993 run, this effect was estimated to be less than $1.7 \pm 1.1\%$. Due to tighter energy collimation on the SLC electron beam and fewer spin precessions in the SLC arcs, the effect was reduced to less than $0.2 \pm 0.2\%$ in the 1994-95 run [8].

3.2 The SLC Large Detector

The SLC Large Detector (SLD) was first proposed[25] in 1984 and was completed in 1991. It is a multi-purpose device for measuring the properties of the decay products of the Z^0 boson. It consists of subsystems which do tracking and precision vertex measurement, particle identification, calorimetry, muon identification, and luminosity measurement. An isometric view of the SLD is shown in Figure 3.7 and a quadrant view is shown in Figure 3.8.

3.2.1 The Luminosity Monitor (LUM)

The SLD luminosity monitor[26], shown in Figure 3.9 consists of two distinct subsections: the Luminosity Monitor and Small Angle Tagger (LMSAT), which covers the angular region from 23 mrad from electron beam to 68 mrad, and the Medium Angle Silicon Calorimeter (MASiC), which covers the region from 68 mrad to 190 mrad.

The LMSAT is used primarily to detect e^+e^- pairs that have undergone Bhabha scattering at the SLC interaction point (IP). As Bhabha scattering is exactly calculable to high

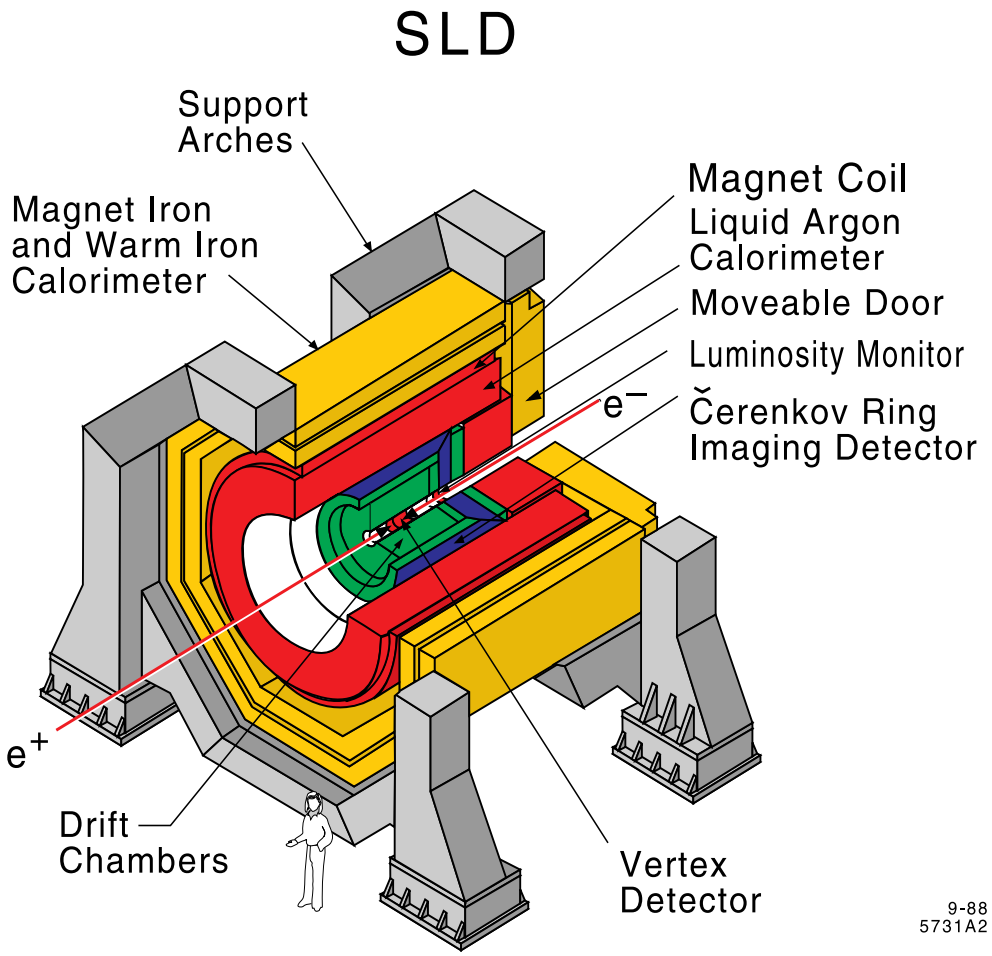

Figure 3.7: An isometric view of the SLD

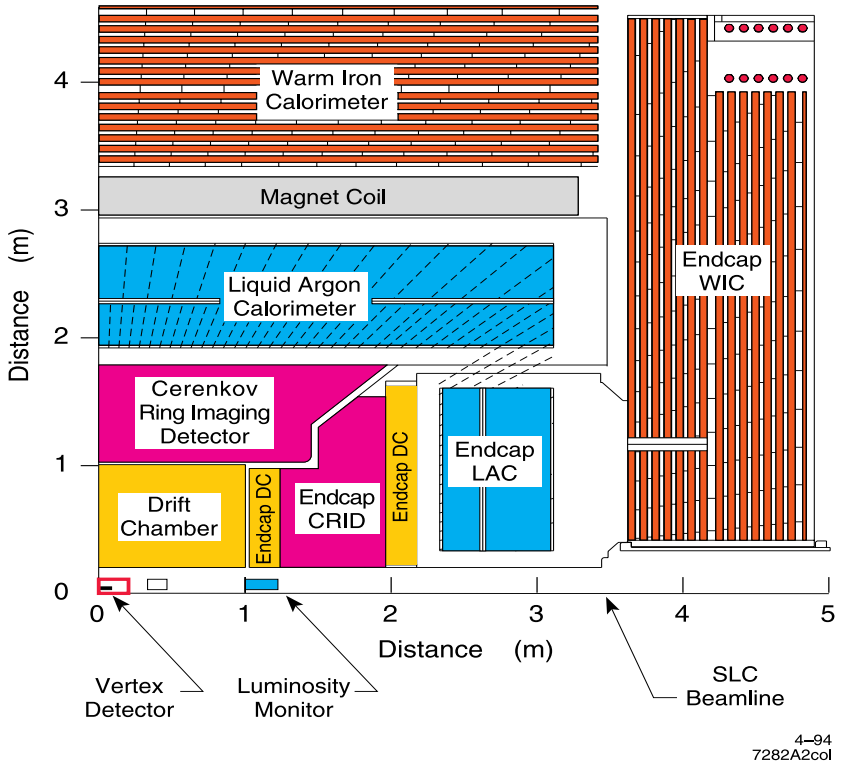

Figure 3.8: A quadrant view of the SLD

precision in QED, and because it occurs much more often than Z^0 production, it provides a precise measurement of the accelerator luminosity.

The LMSAT detectors are segmented into 32 sections in ϕ and 6 sections in θ (LMSAT). It is segmented into two longitudinal segments of 5.5 and 15.6 radiation length. The detectors are composed of tungsten radiator plates interleaved with silicon junction devices maintained in reverse bias. The energy resolution of the detector has been measured [27] to be 6 % at 50 GeV.

3.2.2 The Vertex Detector (VXD)

The VXD uses Charge-Coupled Devices (CCDs) as the medium for detecting the deposition of ionization from through-going charged particles. Since a single CCD is composed of a large number of tiny pixels, a detector based on this technology is a source of three dimensional

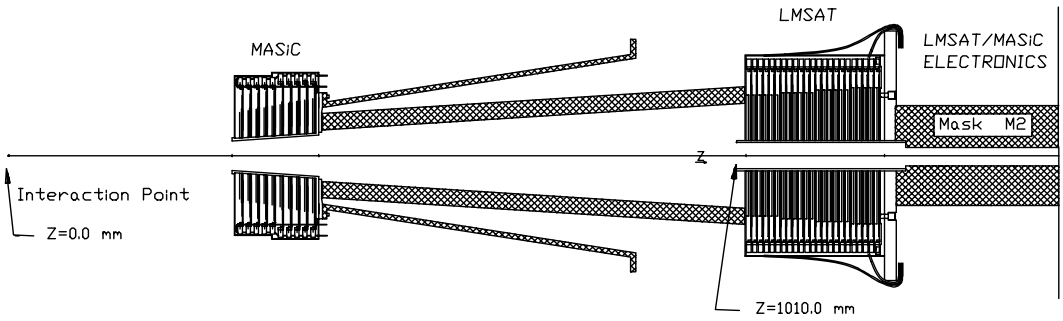

Figure 3.9: The SLD LUM, showing the LMSAT and the MASiC

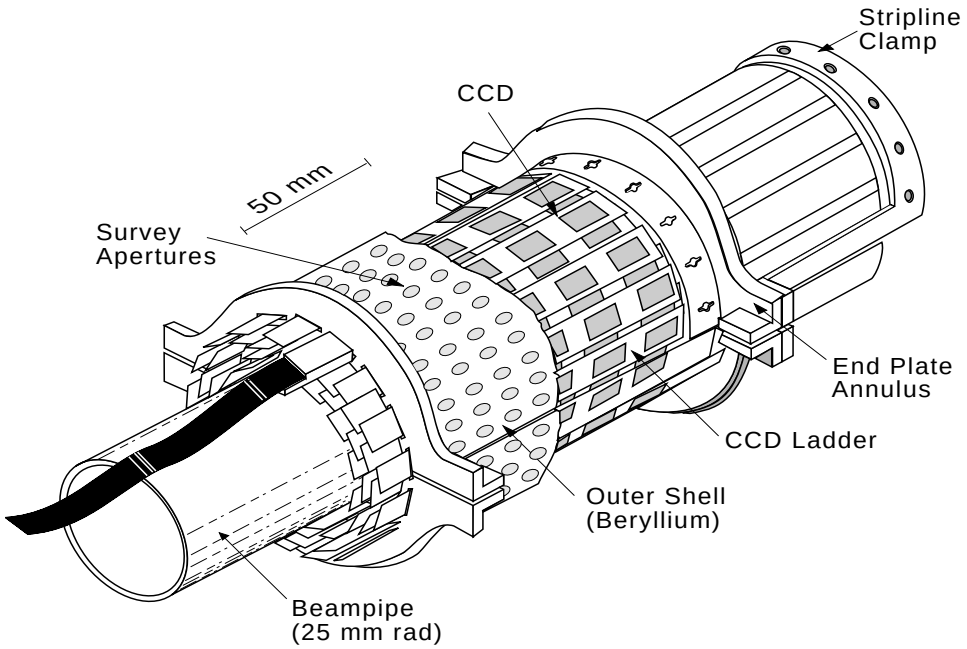

Figure 3.10: The SLD vertex detector (VXD)

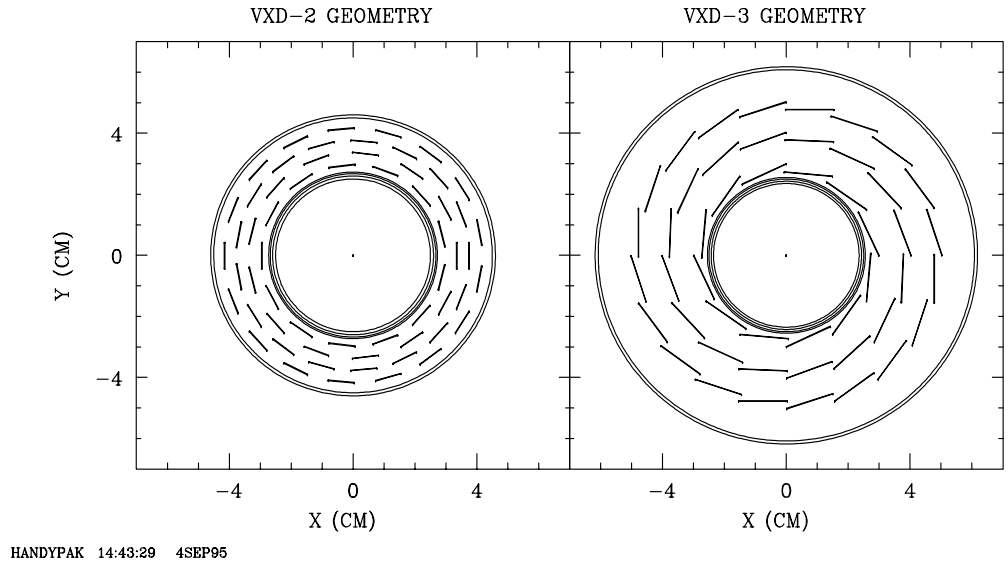

Figure 3.11: An end view of the VXD2 and the new VXD3

space points along the track trajectory.

The VXD, shown in Figure 3.10, is constructed from sixty 9.2 cm long ladders arranged in four concentric cylinders which are held in place by a beryllium shell. Eight CCDs are mounted on each ladder, with four on each side to maintain full coverage in $\cos\theta$. The inner layer of CCDs is 29.5 mm from the IP, and the outer layer is 41.5 mm away. Each layer is 1.1% of a radiation length(X_0) in a material. On the average, 2.3 VXD hits are obtained for each charged track passing through the detector. Each CCD is approximately 1cm square, and contains 375×578 pixels, each 22 μm-square. Each pixel has a depletion depth of 20 μm.

The measured single hit resolutions are 5.5 μm in the $r\phi$ plane, and 5.5 μm up to 9 μm in the rz plane. For high momentum track (muons from $Z^0 \rightarrow \mu^+\mu^-$ events), impact parameter resolutions of $\sim$ 12 μm in the $r\phi$ view and 38 μm in the rz view have observed [28].

The upgraded vertex detector (VXD3) has been installed and operated for the 1996 run. The VXD3 has fully-overlapping three layers of CCD ladders in order to provide at least three spatial hit points for each charged track. The ladder length is also being increased to

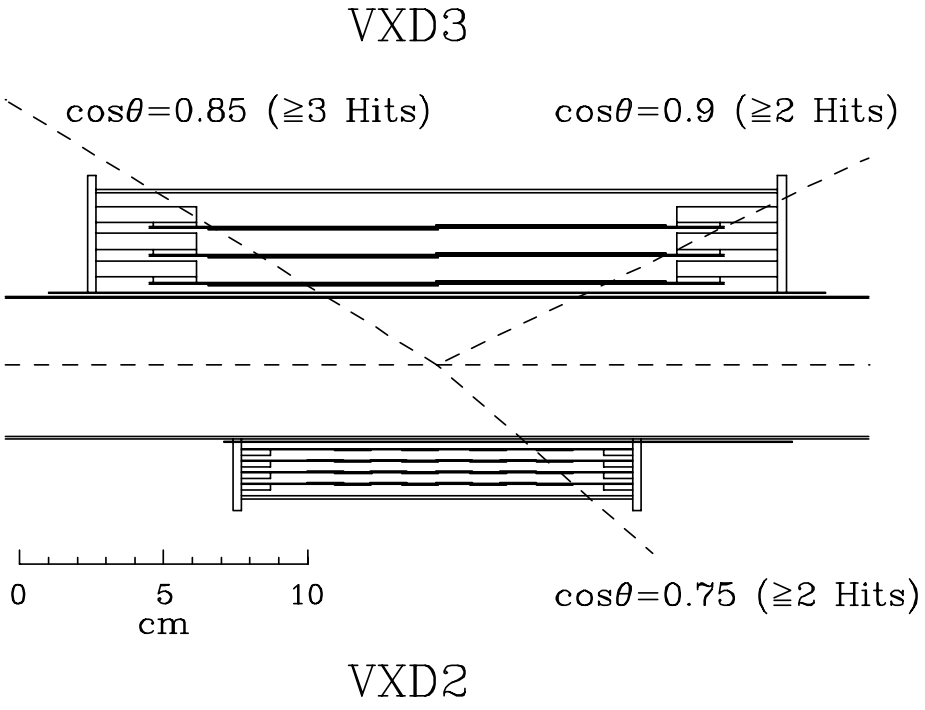

Figure 3.12: A side view comparison of VXD2 and VXD3

provide coverage at lower polar angles. Figures 3.11 and 3.12 show the end and side views of the older VXD2 and the new VXD3 tracker.

3.2.3 The Central Drift Chamber (CDC)

The CDC is the primary tracking device of the SLD. It is constructed in the form of a cylindrical annulus with an inner radius of 20 cm, an outer radius of 1 m, and total length of 2 m. It is composed of 5120 sense wires. The sense wires arranged in 80 layers which are organized into drift cell of 10 superlayers. Each cell is approximately 6 cm wide and 5cm high and contains eight sense wires, two dummy sense wires, 18 guard wires, and 25 field wires (Figure 3.13). The sense wires are 25 μm gold-coated tungsten, and the guard and field wires are 150 μm gold-coated aluminum. The sense and guard wires are mounted together in Lexan blocks, which are precisely positioned and tensioned in the aluminum

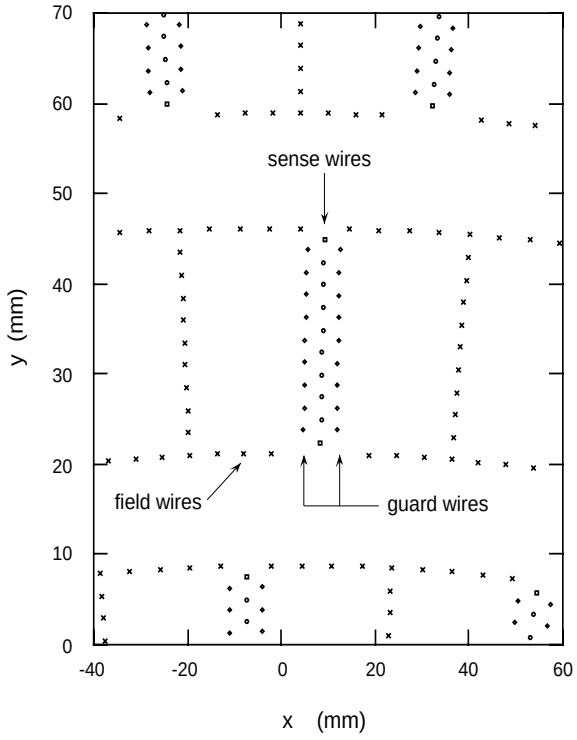

Figure 3.13: A schematic of CDC cell layout

endplate. The inner and outer walls (in radius) of the CDC are made from an aluminum sheet-Hexcell fiberboard laminate, which comprises 1.8% and 1.6% radiation length for the inner and outer wall, respectively. A schematic view of CDC endplate is shown in Figure 3.14. Six of superlayers (U,V layers) have a stereo angle of ± 42 mrad with respect to the beam axis to allow a measurement of the z position of the track hits. In addition, the two end of the sense wire are read out into separate amplifiers, allowing reconstruction of the z position by using charge division.

The CDC drift gas is 75% CO_2, 21% Ar, and 4% isobutane, with a 0.3% admixture of H_2O. The CO_2 base gas provides low drift velocity and low diffusion, which aid the spatial resolution. Argon is added to increase the avalanche gain, and isobutane aids quenching. The water is added to suppress the effects of wire aging [29]. The drift velocity of the final gas mixture is 7.9 μm/ns at the mean drift field of 0.9 kV/cm.

The global and local resolutions are shown in Figure 3.15. The global resolution is found

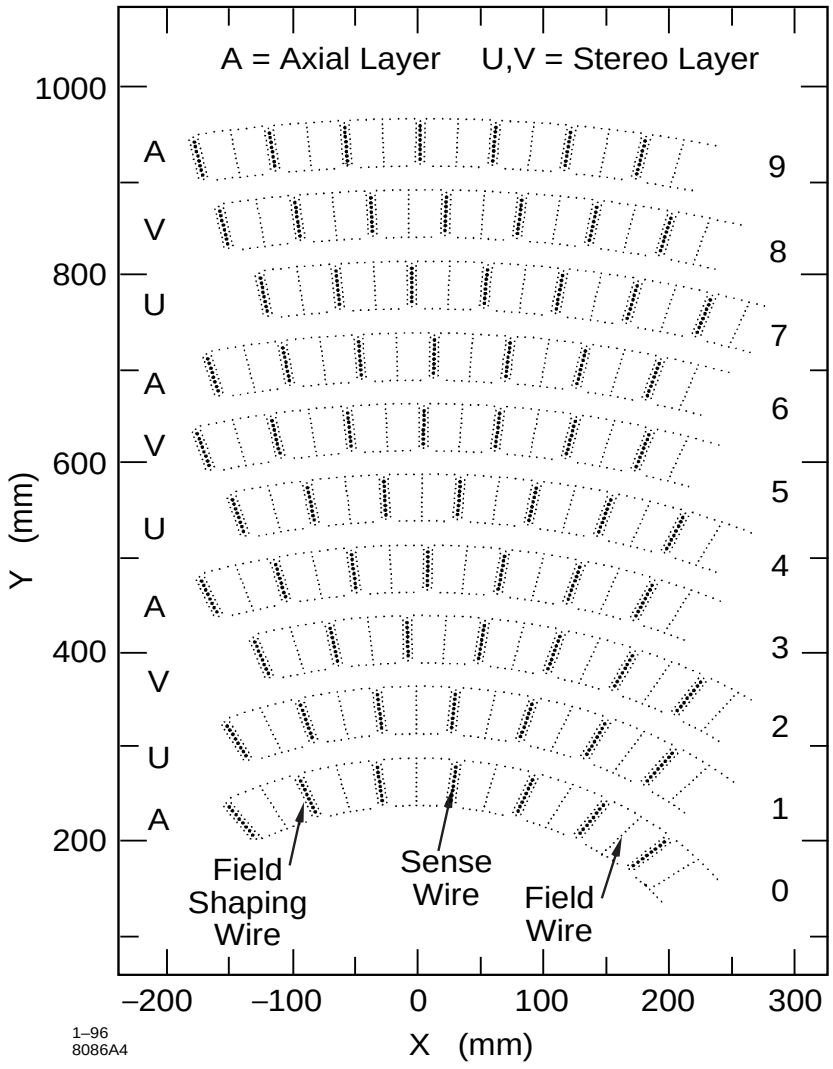

Figure 3.14: Cross-section of a portion of the CDC in the plane perpendicular to the beam.

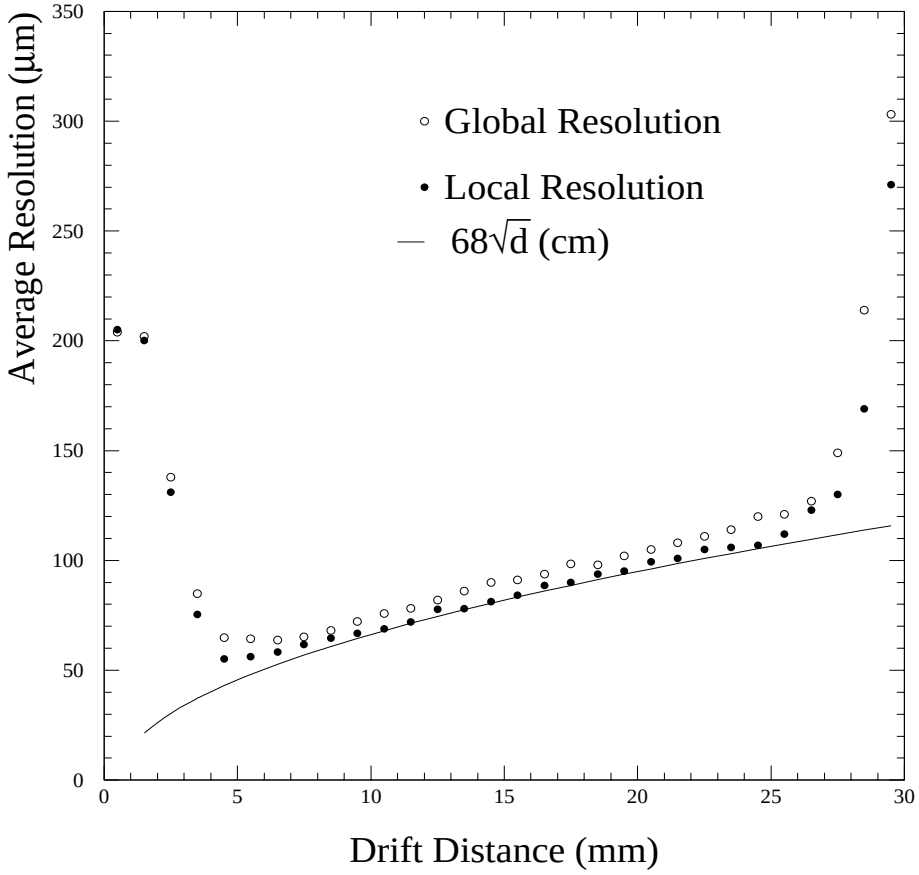

Figure 3.15: The global and local CDC drift distance resolution measured with tracks in hadronic events from the 1994–95 run. Also shown is the resolution expected due to diffusion effects for the CDC gas composition. This diffusion curve has been normalized to the minimum local resolution.

by finding the width of the distributions of track fit residuals as a function of drift distance. The local resolution is obtained by comparing the fit residuals between neighboring hits in a cell. The local resolution is slightly better than the global resolution owing to residual alignment effects arising from the locations of the feedthrough holes in the endplate within their machining tolerances, and tilting of the Lexan blocks within their holes. The resolution worsens at the edge of the cell due to the larger electric fields near the field wires and sense wires, the non-uniformity of the field near the wires, and ionization statistics. The resolution in the central portion of the cell is governed by diffusion. The momentum resolution function for the CDC has been measured to be $(dp_t/p_t)^2 = 0.0050^2 + (0.010/p_t)^2$, where p_t is the momentum of the charged track in the plane perpendicular to the beam axis.

3.2.4 The Cherenkov Ring Imaging Detector (CRID)

The Cherenkov Ring Imaging Detector (CRID) is the particle identification system situated directly outside of the CDC. Since the CRID is playing an important role in the analysis presented in this thesis and we worked much on offline improvements of the barrel CRID, details about the CRID are described in the next chapter.

The barrel portion of the CRID provides the SLD with excellent particle identification over the central 70% of its solid angle. A combination of gaseous and liquid Cherenkov radiators, together with momentum measurement from the CDC, allows $\pi/K/p$ separation up to 30 GeV/c and e/π separation up to 6 GeV/c.

3.2.5 The Liquid Argon Calorimeter (LAC)

Calorimetric energy measurements are provided by the Liquid Argon Calorimeter (LAC), a sampling calorimeter whose basic module consists of lead plate immersed in liquid argon[30]. The argon is the active medium, being ionized by charged particles passing through the calorimeter. The lead serves not only to induce particle showers but also to collect the charge. The layers of lead are broken up into alternating grounded plates tiles held at high voltage. As the lead is stacked, the tiles are arranged into projective towers whose longitudinal depth depends on how many layers have been ganged together for readout.

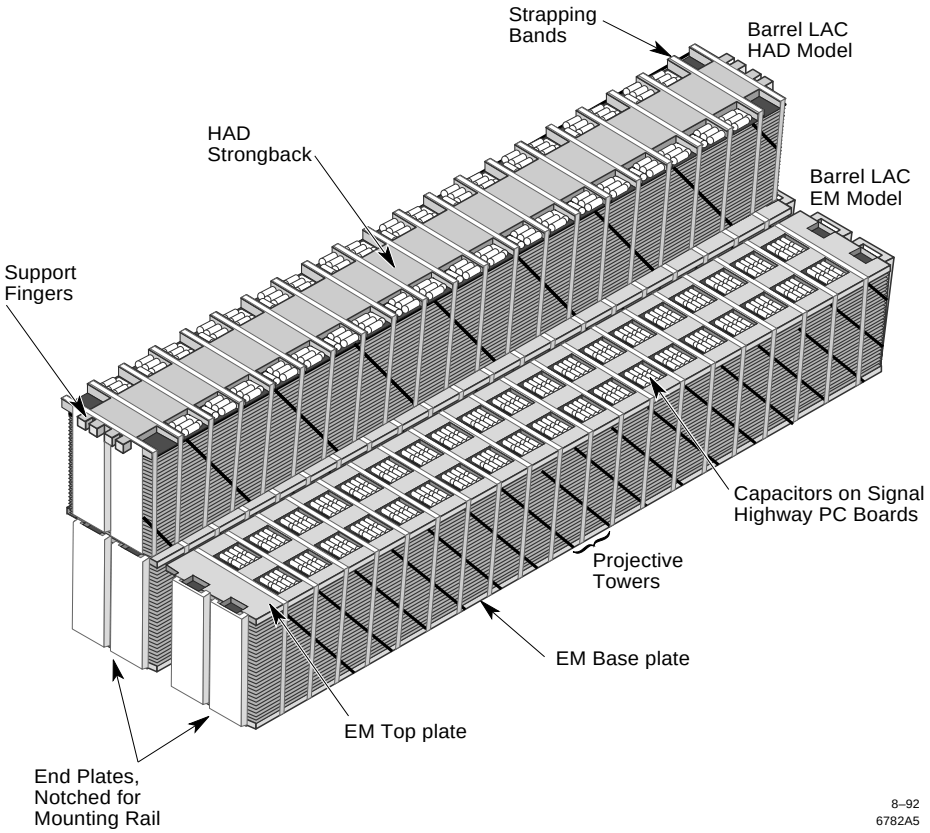

Figure 3.16: View of LAC module, showing the inner EM and outer HAD sections

	EM1	EM2	HAD1	HAD2
ϕ Segmentation	192	192	96	96
θ Segmentation	102	102	48	48
Pb Thickness (mm)	2.0	2.0	6.0	6.0
Ar Gap (mm)	2.75	2.75	2.75	2.75
Radiation Length (X_0)	6.0	15.0	13.9	13.9
Interaction Length (λ_0)	0.24	0.60	1.00	1.00

Table 3.1: Specifications of the LAC

The LAC is segmented longitudinally into four layers, EM1, EM2, HAD1, and HAD2. The EM section is formed of 2 mm thick lead plates separated by 2.75 mm of liquid argon. The HAD section is formed of 6 mm thick lead plates, and the 2.75 mm argon gap is also maintained. The parameters of the four layers are described in Table 3.1. The EM towers subtend one quarter of the solid angle of the HAD tower. The EM sections contain approximately 99% of the energy from 45 GeV electron, while the LAC as a whole contains 85-90% of the total energy in a hadronic Z^0 decay [31]. The measured energy resolution of the EM and HAD sections are $15\%/\sqrt{E}$ and $60\%/\sqrt{E}$, respectively [32].

3.2.6 The Warm Iron Calorimeter (WIC)

Figure 3.17. The Warm Iron Calorimeter (WIC) serves four functions within the SLD: flux return for the solenoid, a backing calorimeter to measure the residual hadronic energy which has leaked out of the LAC, a muon-identification system, and the structural support for the rest of the detector components. The WIC is made of 18 layers of Iarroci tubes sandwiched between 5 mm thick steel plate [33]. The tubes are instrumented with square pad readout for calorimetric purposes and long strips for reading out the individual tubes in order to use the WIC as a muon tracker. The WIC geometry is shown in Figure 3.17. The WIC strips which provide the muon-tracking information are arranged in two separate arrays 90° from each other to enable the trajectory of a muon in two dimensions.

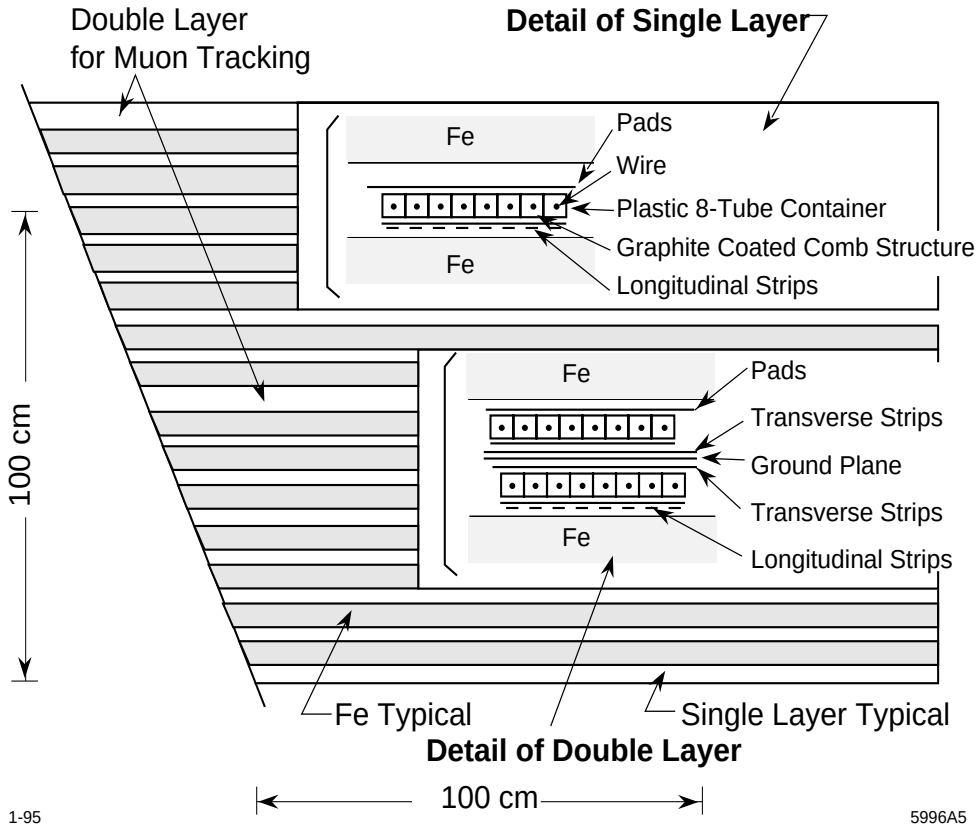

Figure 3.17: Diagram of a section of the WIC, showing the single layers containing longitudinal strips for muon tracking as well as pad tower readout. Also shown are the double layers with crossed strips for tracking in the other plane.

Chapter 4

SLD Monte Carlo

This analysis, as well as many other physics analyses, relies on Monte Carlo models of both underlying physical processes and the detector. In particular, the non $s\bar{s}$ background estimation is sensitive to the A_f ($f = u, d, c, b$), quark production rate, and the fragmentation process. Hence, these physics parameters of electroweak and the fragmentation processes should be input correctly into the Monte Carlo generator. Also, the modeling of acceptances, efficiencies, and resolutions of the detector is incorporated properly since measurement biases are induced by the detector performance.

The SLD Monte Carlo consists of two separate units: one is the event generator which models the underlying Z^0 decay and its products, and the other is the detector simulation model.

4.1 The Event Generator

The event generator chosen for this analysis is the JETSET 7.4 model, incorporating LUND string fragmentation since the parameters in JETSET have been well tuned with many experimental results.

For electroweak parameters, Lund default values are used in the SLD Monte Carlo generator as they have been measured well and have good agreement with Standard Model. Several important electroweak parameters and input values are shown in Table 4.1.

Input parameters in QCD process are determined with the following procedure. The

Parameter	Input value
$\sin^2\theta_w$	0.2319
Z^0 mass	91.187 GeV/c^2
Z^0 width	2.490 GeV/c^2
Higgs mass	300.0 GeV/c^2
Top quark mass	174.0 GeV/c^2

Table 4.1: Electroweak parameters input SLD Monte Carlo

fragmentation process depends on the phenomenological model. Therefore, in the SLD Monte Carlo, the parameters for the QCD process were optimized by experimental results. In the following, we describe the optimization procedure.

The JETSET parameters are divided into three groups and there are 14 parameters to be tuned [13]:

1. Main QCD/fragmentation parameters,
   - Λ_{PS}: the scale of strong interactions used in parton showers.
   - Q_0: invariant mass cut-off value of parton showers, below which partons are not assumed to radiate.
   - a and b in the symmetric Lund fragmentation function (see Eq 2.24).
   - σ_q: the width of Gaussian spectrum of transverse momentum given to hadrons produced in the string break up, to the local string direction.
2. Heavy hadron fragmentation parameters,
   - Peterson fragmentation function option for charm and bottom hadrons, with parameters ϵ_c, ϵ_b.
3. Hadron species production parameters,
   - Diquark relative probability factor: controls global baryon production rates.

- Strange quark relative probability factor: controls strange particle production rates.
- Strange diquark relative probability factor: controls strange baryon production rates.
- Vector meson relative probability factor for light mesons: controls ρ, ω production rates.
- Vector meson relative probability factor for strange mesons: controls K^*, ϕ production rates.
- Vector meson relative probability factor for charm and bottom mesons: controls D^*, B^* production rates.
- η': extra suppression factor. if an η' is rejected a new flavor pair is generated and new hadron formed.

The strategy for tuning Monte Carlo is as followings:

- JETSET 7.4, with the SLD heavy flavor decay modifications but all parameters left at default values, was compared with MCLUND, the existing modified version of JETSET with the SLD standard parameter settings, in terms of hadronic event shapes and single particle inclusive distributions.
- Then, Λ_{PS}, Q_0, σ_q, a, b were fixed to TASSO ($\sqrt{s} = 35$ GeV) tuned values. This choice is motivated by the assumption that, if hadronization is a universal low-energy process that sets in at a Q^2 scale around 1 GeV, then these parameters should be independent of center of mass energy. With all parameters left at their default values, Monte Carlo events were generated and compared with LEP data in terms of the event shapes and single particle inclusive.
- With the above parameters fixed, ϵ_c, ϵ_b were varied so as to reproduce the values of $< x_E >_{had} = 2 < E_{had} > /\sqrt{s}$, where *had* represents either D^* mesons or weakly-decaying B hadrons, determined from Z^0 decays measured at LEP. Monte Carlo events were then generated with these optimized values of ϵ_c and ϵ_b and the event shape observables were re-checked for consistency with LEP data.

Parameter	Default	Optimized
Λ_{PS}	0.29 GeV	0.26 GeV
Q_0	1.0 GeV	1.0 GeV
σ_q	0.36 GeV/c	0.39 GeV/c
a	0.3	0.18
b	0.58 GeV^{-2}	0.34 GeV^{-2}
ϵ_c	-0.05	-0.06
ϵ_b	-0.005	-0.006
diquark prob.	0.10	0.08
s quark prob.	0.30	0.28
s diquark	0.40	0.60
vector meson prob. (u,d)	0.50	0.50
vector meson prob. (s)	0.60	0.45
vector meson prob. (c,b)	0.75	0.53
η' prob.	0.40	0.20

Table 4.2: Default and optimized values of JETSET 7.4 parameters.

- With all of the above parameters fixed, the vector meson relative production probability for charm and bottom mesons was set to 0.53, corresponding to the inclusive D^*/D production ratio measured at LEP. The remaining of 6 hadron species production rate parameters were then varied separately in an attempt to reproduce the mean number per hadronic event of: charged and neutral K, protons, Λ, η and η', subject to the requirement that total charged multiplicity sum to the world-average value at Z^0.

The default and the optimized values of JETSET 7.4 parameters are shown in Table 4.2. Table 4.3 shows the results of parameters measured at several experiments.

The SLD Monte Carlo generates half of its events with an electron beam polarization of +100%, and half with -100%, with the positron beam unpolarized in both cases. In order to simulate properly left-right asymmetry, the number of of left- and right-handed events are adjusted. Also, the polarization in the Monte Carlo is diluted to real data. These adjustment

Experiments	Parameters						
	Λ_{PS}	Q_0	σ_q	a	b	ϵ_c	ϵ_b
Mark II/PEP [34]	0.40	1.0	0.33	0.45	0.90	-	-
TASSO [35]	0.26	1.0	0.39	0.18	0.34	-	-
OPAL [36]	0.29	1.0	0.37	0.18	0.34	-	-
ALEPH [37]	0.32	1.4	0.36	0.50	0.92	0.05	0.006
L3 [38]	0.30	1.0	0.39	0.50	0.76	0.07	0.008

Table 4.3: JETSET 7.4 parameters obtained by other experiments

are made by mixing left-handed events and right-handed events properly:

$$N_L = \frac{1}{4}(1+P_e)(1+A_{LR})N'_L + \frac{1}{4}(1-P_e)(1-A_{LR})N'_R \tag{4.1}$$

$$N_R = \frac{1}{4}(1-P_e)(1+A_{LR})N'_L + \frac{1}{4}(1+P_e)(1-A_{LR})N'_R \tag{4.2}$$

where P_e is the electron beam polarization and A_{LR} is the left-right asymmetry and the value 0.153 is used here. $N'_{L(R)}$ is the number of left(right)-handed events at generator, $N_{L(R)}$ is the number of events after adjustment.

4.2 Detector Simulation

The detector simulation is necessary to simulate the efficiency, acceptance, and resolution effects. The SLD simulation is based on the GEANT 3.21 package [39], which tracks particles from the Z^0 decay generator and calculate the probability of multiple scattering and energy loss according to a detailed description of detector material and a magnetic field map [40]. Hadronic interaction is simulated by GEANT GHEISHA package [41] and electromagnetic interaction is simulated by GEANT EGS4 package [42]. The output of the simulation process is in the same format as the data that is written to tape through the data acquisition system, so that the same reconstruction programs may be applied to simulated data as applied to the actual data. In each detector subsystem, the Monte Carlo parameter tuning has been attempted. Details of the simulation for the tracking systems and the calorimetry

can be found in [43] and in [27, 31]. Also in the CRID system, the simulation has been tuned to reproduce the observed particle identification efficiency considering Cherenkov angle smearing, variation in number of Cherenkov hits, the rate of tracks that are unambiguously identified as any of the available hadronic hypotheses ($\pi/K/p$), and background hits in TPC. A detailed discussion of the CRID Monte Carlo tuning can be found in [8] (see also Section 5.5).

In order to simulate the beam-induced backgrounds, as well as noisy electronics channels, raw data from random triggers is overlaid in the simulation data. The signals from random trigger are merged with the digitized signals from the Monte Carlo simulation, and the event is then processed through the standard SLD reconstruction package.

Chapter 5

Barrel CRID

As described in Chapter 2, the SLD Cherenkov Ring Imaging Detector (CRID) is one of the most powerful particle ID tools in the world. In this chapter, the design and performance are described. We also discuss in detail two important aspects of CRID reconstruction, the internal alignment of the 40 TPCs and the alignment of the 400 mirrors. A more complete description of the SLD CRID design can be found in [25].

5.1 Principles and design of the CRID

The particle identification of the CRID is based on measurement of the opening angle of the cone of Cherenkov light emitted as a charged particle passes through a dielectric medium with a velocity exceeding the phase velocity of light in that medium. The opening angle θ_c of Cherenkov radiation is given by

$$\cos\theta_c = \frac{1}{n\beta,} \tag{5.1}$$

where β is the velocity of the particle divided by the vacuum speed of light, and n is the index of refraction of the medium. In order to detect Cherenkov photons, time projection chambers(TPC) are used with large area transparent windows. A photocathode material Tetrakis(dimethylamino)ethylene (TMAE) is contained in the TPC gas. TMAE has an ionization potential of 5.4 eV and good quantum efficiency [44].

The components of the barrel CRID are shown in Figure 5.1 and Figure 5.2. There are 20 sectors; 10 each for the south and north side of the SLD. Each sector consists of 2 liquid

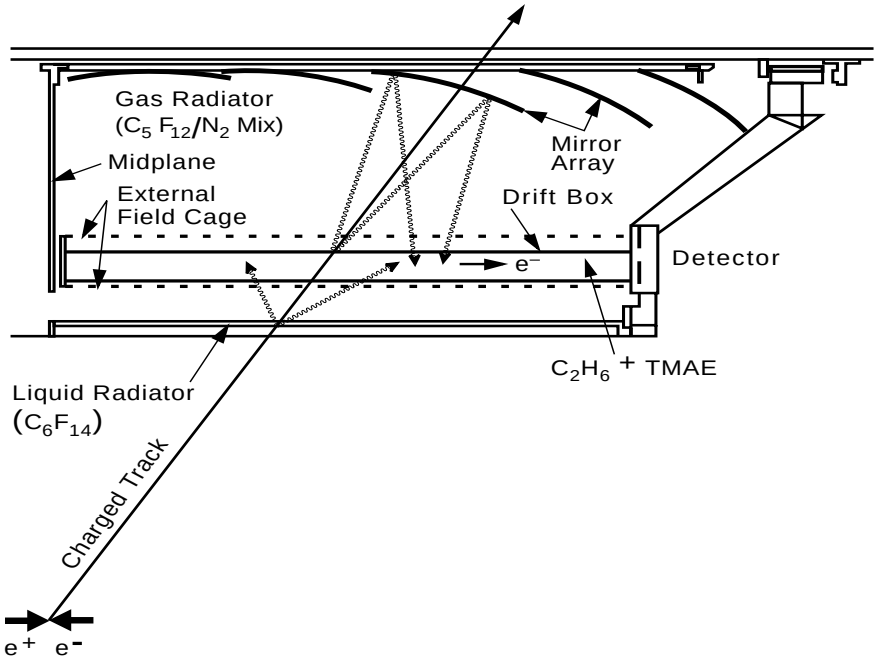

Figure 5.1: Sectional view of the barrel CRID. One sector is shown in the axial view. The layout is symmetric about the mid-plane.

Cherenkov radiator trays, 2 TPC boxes, and 20 mirrors. A gaseous radiator vessel contains all 20 sectors. The liquid Cherenkov radiator (C_6F_{14}) is contained in each quartz-windowed tray. A track passing through radiator emits a cone of Cherenkov light that expands over $\sim$ 12 cm and hits inner TPC window. The gaseous radiator (C_5F_{12}) fills the vessel and each spherical mirrors in the vessel is adjusted to focus the Cherenkov photons into a ring on a specific region of the outer window of one TPC. The quartz-windowed TPCs are filled with C_5F_{12} and 0.1% TMAE. The Cherenkov photons ionize the TMAE, and the resulting photoelectrons are drifted by an electric field to multi-wire proportional chamber (MWPC) detectors located at the outer end of the TPCs.

The barrel CRID is designed to provide particle identification over 70% of the available solid angle and for momenta up to 6 GeV/c (e/π) or 30 GeV/c ($\pi/K/p$). This is accomplished by the combination of liquid C_6F_{14} and gaseous C_5F_{12} radiators. Cherenkov angle curves for these two radiators are shown in Figure 5.3 as a function of momentum. The two

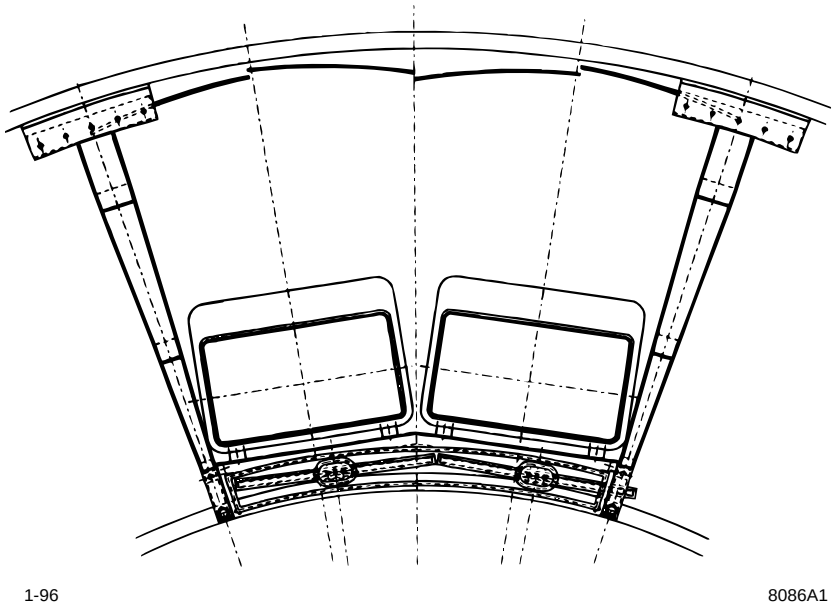

Figure 5.2: End-on view of the barrel CRID. One sector is shown in the radial view. There are 10 such sectors in each of the two halves (north and south).

fluorocarbon radiators used in the CRID were chosen for their refractive indices, so as to provide particle identification coverage with a minimal inefficiency gap in momentum. They were also chosen for their transmission at relevant UV wavelengths, for their relatively low chromatic dispersion, and for their compatibility with other materials used in the CRID. Furthermore, fluorocarbons are non-flammable, unlike isobutane (C_4H_{10}), for example, which was also considered at one time for use as a gaseous radiator.

The liquid C_6F_{14} is contained in quartz-windowed trays of thickness 1 cm and has an index of refraction $n = 1.2723$ at $\lambda = 190$ nm [45]. The Cherenkov light from the liquid radiator trays is imaged directly onto the TPCs.

The gaseous C_5F_{12} radiator is contained within the volume of the CRID vessel, which lies outside the TPCs. A total of 400 UV-reflective spherical mirrors [46] installed on the outer cylinder of the CRID vessel is used to reflect the Cherenkov photons onto the TPCs. A spherical mirror focuses parallel rays emitted at different points along a track's trajectory into a single point at a focal distance equal to half of the mirror's spherical radius [47].

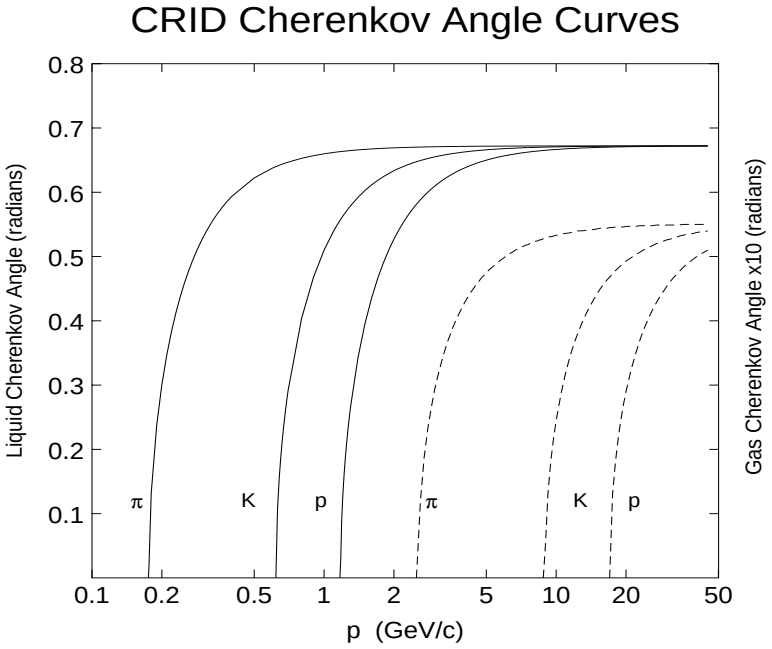

Figure 5.3: The Cherenkov angle as a function of momentum is shown for the two CRID radiators and for the three hadronic particle hypotheses.

Because of the restriction of temperature, the gaseous radiator is mixed with nitrogen in a ratio of roughly 85% C_5F_{12} to 15% N_2. The index of refraction of this mixed gas is about $n = 1.0017$ at $\lambda = 190$ nm [48].

The Cherenkov photons from the two radiators are imaged in the TPCs, where they photoionize the C_2H_6 drift gas with TMAE dopant. The resulting single photoelectron is drifted parallel to the SLD magnetic field by an electric field of 400 V/cm to proportional wire planes (MWPCs) at the outer edge of the CRID (Figure 5.4). The volume inside the TPCs is 126.8 cm long by 30.7 cm wide, with a thickness of 5.6 cm at high voltage end and 9.2cm at the detector end. This taper structure prevents transverse diffusion from causing electron losses near the faces of the TPC.

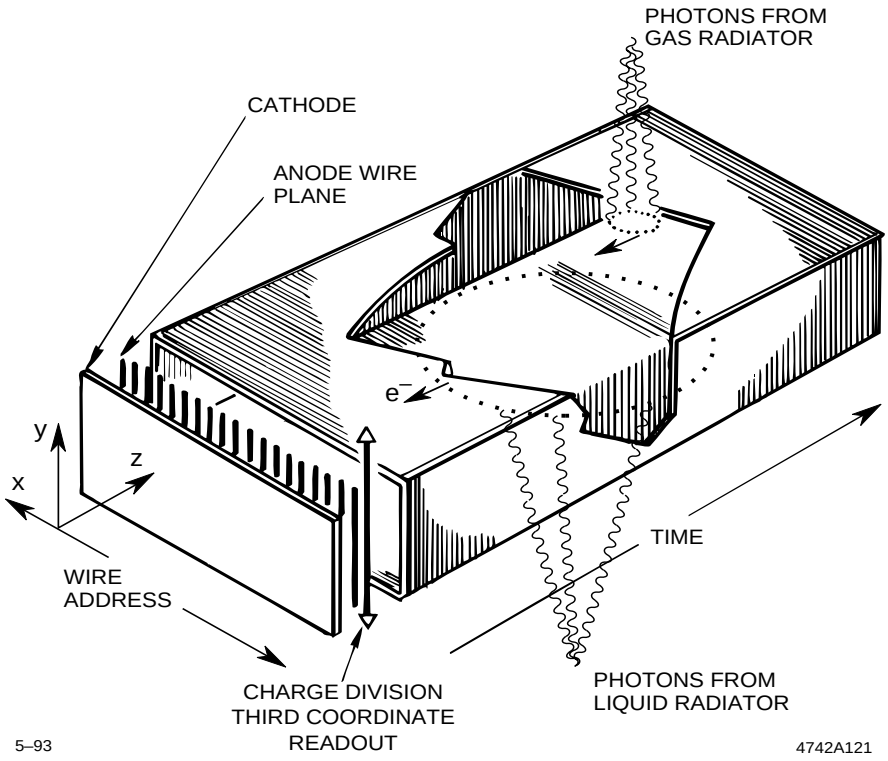

Figure 5.4: Schematic view of a TPC and MWPC detector for the barrel CRID. Also shown is the standard TPC coordinate system employed in the CRID reconstruction.

5.2 Internal TPC alignment

In order to achieve the design angular resolution of the CRID, spatial resolutions of individual photoelectrons are required to be 1-2 mm. For this analysis, it is necessary to tag high momentum strange particles. Therefore, the improvement of the resolution of Cherenkov angle especially for gas radiator had been required as seen in Figure 5.3. For this purpose, two major improvements were performed; one is the alignment for the trajectory of photoelectrons in TPC discussed in this section, the other is the alignment of UV-reflective spherical mirrors described in the next section. Deviations from axial of photoelectron drift in the drift boxes are observed. The transverse shifts are caused by the radial component of the SLD magnetic field. In addition, the combination of small misalignment of the drift box axes and electrostatic distortions are observed at a few mm level [50].

5.2.1 UV Fiber

The UV fiber system used for this study consists of a UV flashlamp and an array of 600 μm core silica optical fibers. The fiber system injects UV light into the drift boxes at various points which serve as fiducial marks. It was designed to provide drift velocity monitoring and measurements of electron trajectories in the $x-z$ plane using the vertical fibers, shown in Figure 5.5. The 45° inclined fibers nearest the detector are used for charge division calibration. The three 45° inclined fibers in the middle are used for trajectory measurements in the $y-z$ plane; a right handed coordinate system is used.

The light is generated by the flashlamp[1] filled with xenon and triggered every beam crossing at 120 Hz. The trigger circuit consists of a silicon controlled rectifier(SCR) that fires the auxiliary electrode of the flashlamp which initiates the discharge of capacitor through the main electrode. The discharge capacitor was chosen to be 1 nF which results in a pulse width of 70 ns. The jitter intrinsic to the lamp is 200 ns. The light is transported over an average distance of about 12 m to the drift boxes by fused silica UV transmitting optical fibers[2] having 600 μm core diameter. At each drift box the 600 μm fibers illuminates a bundle of 19 silica fibers having 200 μm core diameter which in turn route the light to the appropriate position on the drift box.

The full angle of the cone of light emerging from the fibers is limited to 2° by a collimator. The collimators shown in Figure 5.6 were designed with a cavity in the middle because otherwise light would reflect at a grazing angle on the inside walls and widen the emerging light cone. The extreme variation in light intensity between the fibers is a factor of 10 due to the routing of each fiber, which causes different amounts of bending, and the transmission non-uniformity of short segments of optical fibers [51].

The fiber data are logged during the run together with the rest of the CRID data for monitoring of drift velocity. For this study, special runs were taken with cold TMAE and both magnetic field on and off. The intensity of the flashlamp is adjusted so that the probability for a photoelectron to be generated at each fiducial point is approximately 10%.

[1] Hamamatsu xenon flashlamp L2435.

[2] UV optical fiber by Fiberguide Industries, NJ 07980, U.S.A.

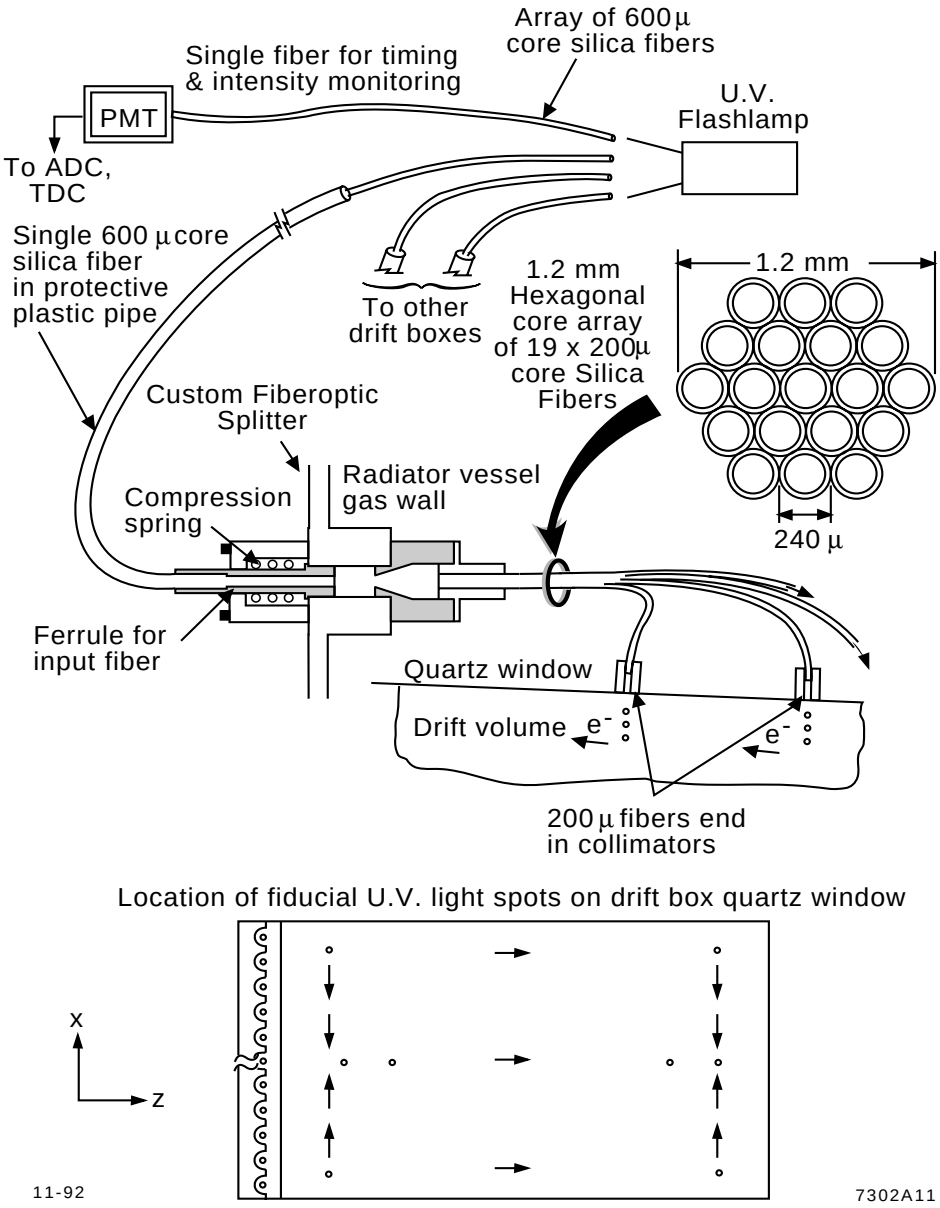

Figure 5.5: Diagram of the CRID fiber fiducial system. A xenon flashlamp provides UV light pulses, which are transmitted by optical fiber to known positions on the surface of the CRID TPCs. The positions of the 8 vertical (∘) and 11 inclined (→) fibers are shown in bottom.

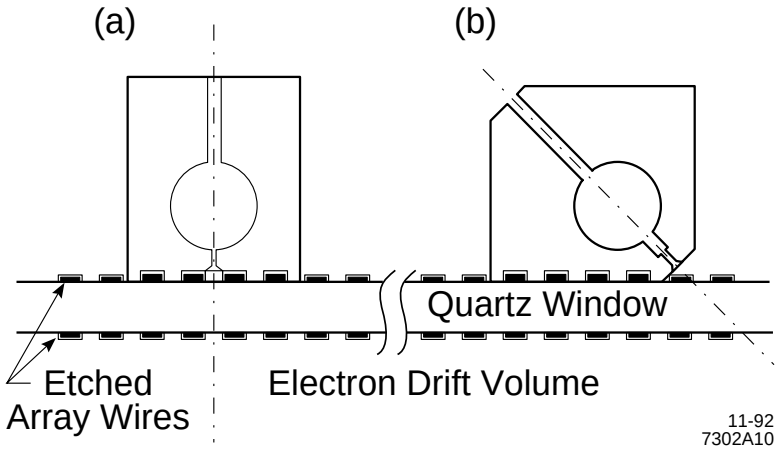

Figure 5.6: The collimators which mount the fibers onto the TPC surfaces

They account for 5% of the data in an event caused by colliding beams.

In this study, the trajectory of photoelectrons were measured by 5 fibers (4 vertical and 1 inclined) in the center region of TPC x.

5.2.2 Fiducial Fiber Locations on Drift Boxes

The first step of this drift distortion study is to understand the locations of the fiducials on the boxes. Fiber data taken with magnetic field off were used to study the positions of the five fiducials along the center-line of the drift boxes. The signal from these 5 fiducials were selected according to time delay windows using the average of all fiducials in the event to determine the flash time. Then, they were divided into 5 y-slices exactly covering the depth of the box for that fiducials. The position in y is measured by the charge division of the inner and outer signals.

The x-distribution of the hits in each slice was fitted with a gaussian plus constant. The fitted central values of the x-distributions, $\bar{x}(y)$ were found to be linear as a function of y for all fiducials. From linear fits to $\bar{x}(y)$, the fiducial beams were found to be vertical to the window surface on average with an root-mean-square of about 0.8°. This is consistent with the expected value of about 1°. The collimator positions x_{col} were taken to be the value of this fit at y just outside the outer quartz window (see Figure 5.6). The collimators along the

drift direction were found to be systematically shifted from their nominal positions. Figure 5.7 shows collimator position as a function of z for a typical TPC #1 for 1993 fiber runs.

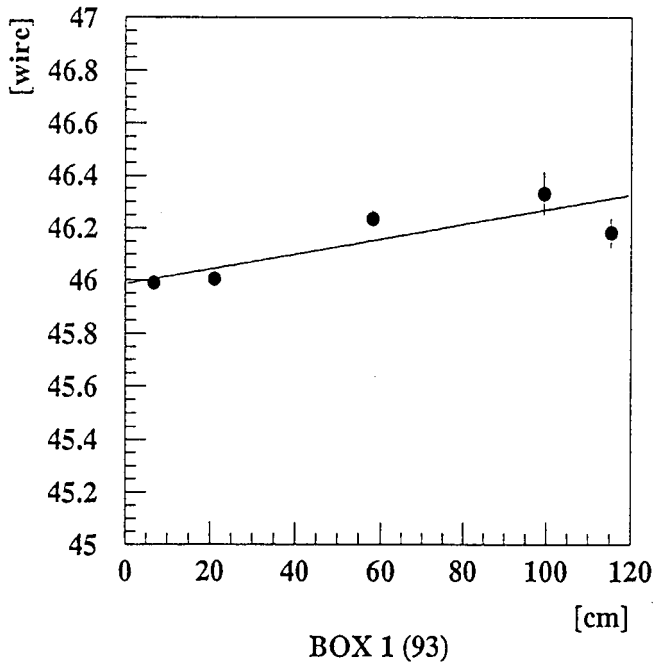

Figure 5.7: Collimator position of 5 fibers in center region of TPC #1

5.2.3 Magnetic Field Distortions

Because the SLD solenoidal field, $\vec{B}$, is not perfectly parallel to the CRID electric field, $\vec{E}$, the trajectory of a drifting photoelectron deviates from the electric field direction due to the small radial component of the magnetic field, B_r. Furthermore, any misalignment of the TPCs with respect to the SLD z-axis, and electrostatic focusing give deviation of the trajectory. By comparing fiducial positions with the SLD solenoid on against those with the magnet off, we can measure the shifts as a function of drift distance [8].

The basic relationship of the drifting electron in electromagnetic field is described in [49]. The drift velocity of an electron is given by

$$\vec{v}_d = \frac{\mu}{1+(\omega\tau)^2}\left[\vec{E} + \frac{\omega\tau}{B}(\vec{E}\times\vec{B}) + (\omega\tau)^2\frac{\vec{E}\cdot\vec{B}}{B^2}\vec{B}\right], \tag{5.2}$$

where μ is the electron mobility, ω is the Larmor frequency, and τ is the mean time between collisions. Working in the SLD coordinate system, the electric field is assumed to be along z, pointing towards the mid-plane, $\vec{E}\cdot\hat{z} = \mp E_z$. The magnetic field lies approximately along the z-axis $\vec{B} \simeq B_z\hat{z}$, but with a small radial component

$$\vec{B}\cdot\hat{r} = B_r(r,z) = B_r^0\frac{rz}{r_0 z_0}, \tag{5.3}$$

where the parameterization of $B_r(r,z)$ is based on a simple finite solenoid model, which has been confirmed by measurements of the actual field [25]. Integrating Eq (5.2) over z, we get

$$\begin{aligned} \delta r &= \frac{(\omega\tau)^2}{1+(\omega\tau)^2}K\left(z_1^2 - z_2^2\right) \\ r\delta\phi &= \frac{\omega\tau}{1+(\omega\tau)^2}K\left(z_1^2 - z_2^2\right), \end{aligned} \tag{5.4}$$

where z_1 (z_2) is the z coordinate of the start (end) of drift considered, and $K = r_c B_r^0/(2r_0 z_0 B_z)$ with r_c, the radius at the CRID TPCs. Including the effects of electrostatic focusing (discussed in detail in 5.2.4) and of small misalignments of the TPCs, these shifts can be parameterized by a quadratic function of drift distance (in TPC coordinates) [50]:

$$\begin{aligned} \delta x &= (\sin^2\alpha\epsilon_x \pm \sin\alpha\cos\alpha\epsilon_y)z \pm \sin\alpha\cos\alpha f(y-y_c) \pm \sin\alpha\cos\alpha K z(2z_0 - z) \\ \delta y &= (\sin^2\alpha\,\epsilon_y \mp \sin\alpha\cos\alpha\epsilon_x)z - \cos^2\alpha f(y-y_c) + \sin^2\alpha K z(2z_0 - z), \end{aligned} \tag{5.5}$$

where the upper (lower) signs stand for south (north) TPCs, α is the Lorenz angle, $\tan\alpha = \omega\tau$ (41° for C_2H_6), y_c is the center of the anode wire, z_0 is anode wire position in SLD-z, f is the focusing strength, and ϵ_x, ϵ_y are the angular misalignments of the TPCs. The first term in Eq (5.6) comes from the misalignment of the TPC, the second term from the electrostatic focusing, and the third term from the radial component of magnetic field.

The focusing is not expected to affect the fiducial beam at the center in y of the drift box. The difference between the measured $x_c = \bar{x}(y_c)$ values with magnetic field on and off is therefore taken to be the shift due to misalignments of the TPCs and radial components of the SLD magnetic field. For each box these shifts were plotted as a function of z and fitted with the form $\Delta x_c = \lambda z(2z_0 - z)$ with λ as free parameter. In addition, linear term

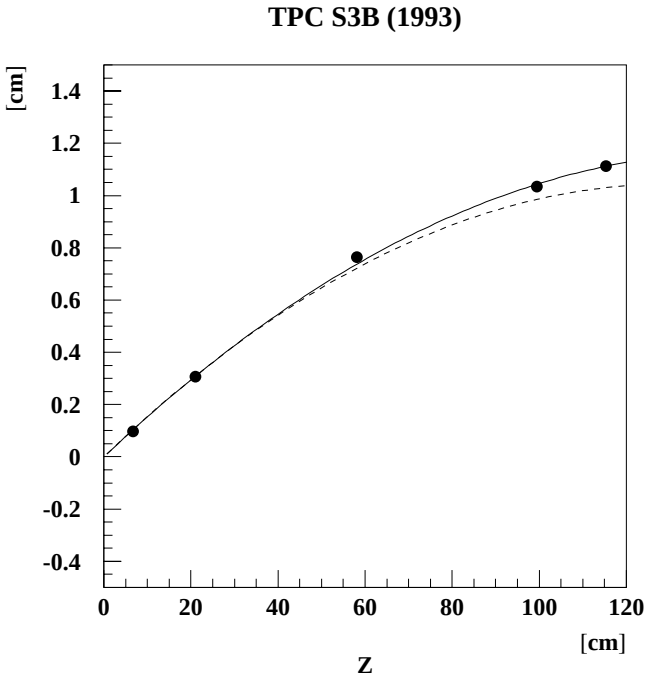

Figure 5.8: The δx shift in positions of fiber fiducials with the SLD magnetic field as a function of TPC-z for one TPC on the south barrel. The dashed curve is the quadratic shift expected from the radial magnetic field B_r. The solid curve includes a linear term for misalignments of the TPC drift direction with respect to the axis of the SLD $\vec{B}$ field.

was taken into account to obtain good fits. Figure 5.8 is the typical plot for x_c and fitted with

$$\delta x_c(z) = az + \lambda z(2z_0 - z). \tag{5.6}$$

There is box-to-box variation for a although the average is 0.0019 for 1993 fiducial run data. This is consistent with the assumption of an end-plate rotation of 3 mrad on which the TPCs are fixed.

5.2.4 Electrostatic Focusing

Distortions from the expected electron trajectory can arise from several electro static causes. One of these causes is non-uniformity of the electric potential gradient along the TPC, which gives a non-linear time-to-distance relationship. Another source of the distortions comes from the perturbations in the drift field due to a buildup of positive ions on the walls of the chambers or in the gas volume. This had been studied for long time using the CRID prototype, and the former build-up found to be minimal [52].

The major distortion in the CRID TPCs comes from the "focusing" effect due to nonuniform electric fields in the transition region between the TPC active volume and the MWPC detector region.

Linear fits for fitted centers of the x-distributions for 5 y-slices were performed on all fiducials to find the slopes with and without magnetic field. The differences in slope were considered as focusing term(f). The slope changes for the fiducials in each box were averaged and the results shown in Figure 5.9. For 1992 fiducial fiber run, the averaged angular shifts was $f \simeq 0.15$. For 1993, this f were uniformly reduced. This is due to the reduction of nominal voltage of drift boxes by about 100 V.

5.3 Mirror alignment

In the CRID, a photon emitted in the gas radiator is reflected by a spherical mirror and a Cherenkov ring image is focused onto the photosensitive detector plane. In the barrel, each spherical mirror covers 9° in polar angle and a set of five mirrors installed on one ladder covers from 90° (mid-plane of the barrel) out to 46° in polar angle. There are 400 mirrors in total, each about 30 *cm* by 27 *cm* with radii of curvature near 1 m. The construction of the mirrors used in the CRID is described in detail in [53]. We aligned those 400 mirrors by fitting the gas rings for a sample of isolated tracks with momentum above 4.5 GeV/c from all available hadronic and leptonic Z^0 decays [54]. In the fits, the Cherenkov radius, r_c, as well as the position of the center of the ring (x_c, y_c) in Cherenkov angle space is allowed to vary.

At first, five mirrors on the same ladder were grouped since survey had been done on

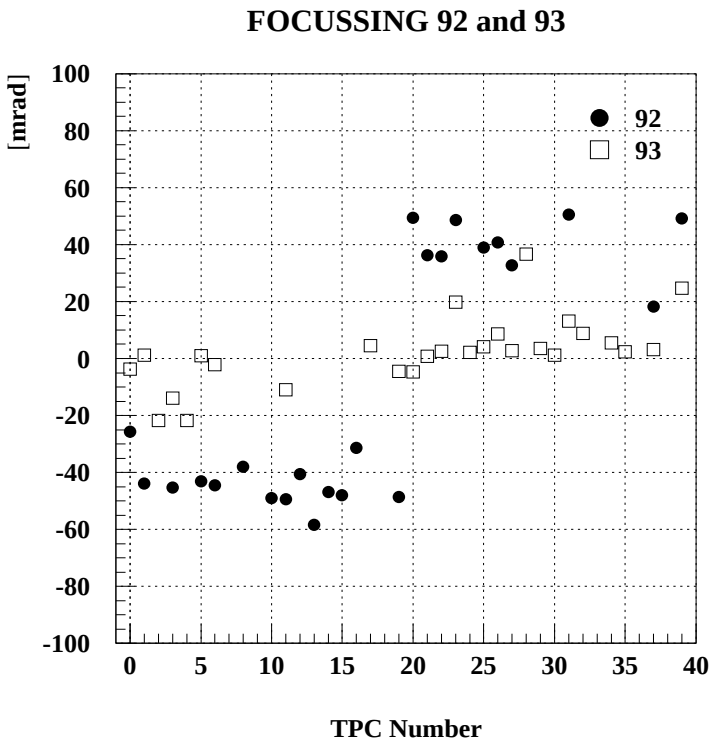

Figure 5.9: The electrostatic focusing measured in fiber fiducial data as a function of the TPC number for the 1992 (dots) and 1993 (squares) data. The effects of the adjustment of the voltage V_B are clearly visible.

ladders. For tracks pointing to any of the five mirrors, the difference between the fitted ring center and corresponding track center are investigated to correct for the offset in x and z directions in the reconstruction. There are four types of ladders in each sector as seen in Figure 5.2. A systematic dependence on mirror type was found even after ladder alignment (Figure 5.10). This indicates that some mirrors within the ladder are aligned differently from others. So, all 400 mirrors were aligned individually.

In this fit, rings with 5 or more hits are used, and typically 100-200 entries (ring found) per mirror. There are 4 mirrors which have no entries and another four which had fewer entries. These mirrors are hypothesized to be badly installed or to have poor reflectivity and have been flagged as not to used for particle identification.

Figure 5.11 shows the deviations measured for individual mirrors before and after align-

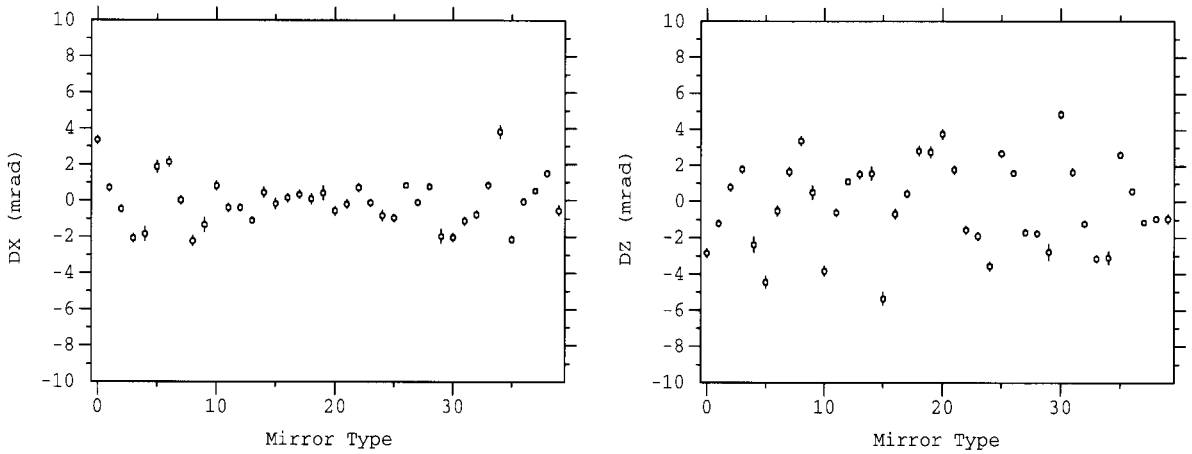

Figure 5.10: The average shift of ring centers in TPC-x (left), DX, and TPC-z (right), DY, from the corresponding track center for the 80 mirror types. Mirrors with type number (4n+1,n=0,1,...19) are categorized to the same group.

ment. Inclusive deviations in TPC-x and TPC-z for all mirrors are shown in Figure 5.12. Before mirror alignment, the spread of ring centers was a dominant contribution to gas ring resolution. The alignment reduced the σ in gaussian fits from $\sigma_x = \sigma_z = 5.0$ mrad to $\sigma_x = 4.2$ mrad and $\sigma_z = 3.6$ mrad respectively.

5.4 Particle Identification Method

After Cherenkov angle reconstruction, the particle identification is performed by calculating likelihood functions for five possible particle hypotheses $e/\mu/\pi/K/p$ for each track. For now, we only consider charged hadrons (π, K, p). The maximum-likelihood method which is used in this analysis gives smooth behavior as a particle's momentum crosses the Cherenkov threshold for a particular hypothesis and provides a simple framework for combining liquid and gas Cherenkov information. The CRID likelihood algorithm is described in [55] and [56]. For each hypothesis, a likelihood L_i $(i = \pi, K, p)$ is calculated based upon the number of detected photoelectrons and their measured angles, the expected number of photons, the

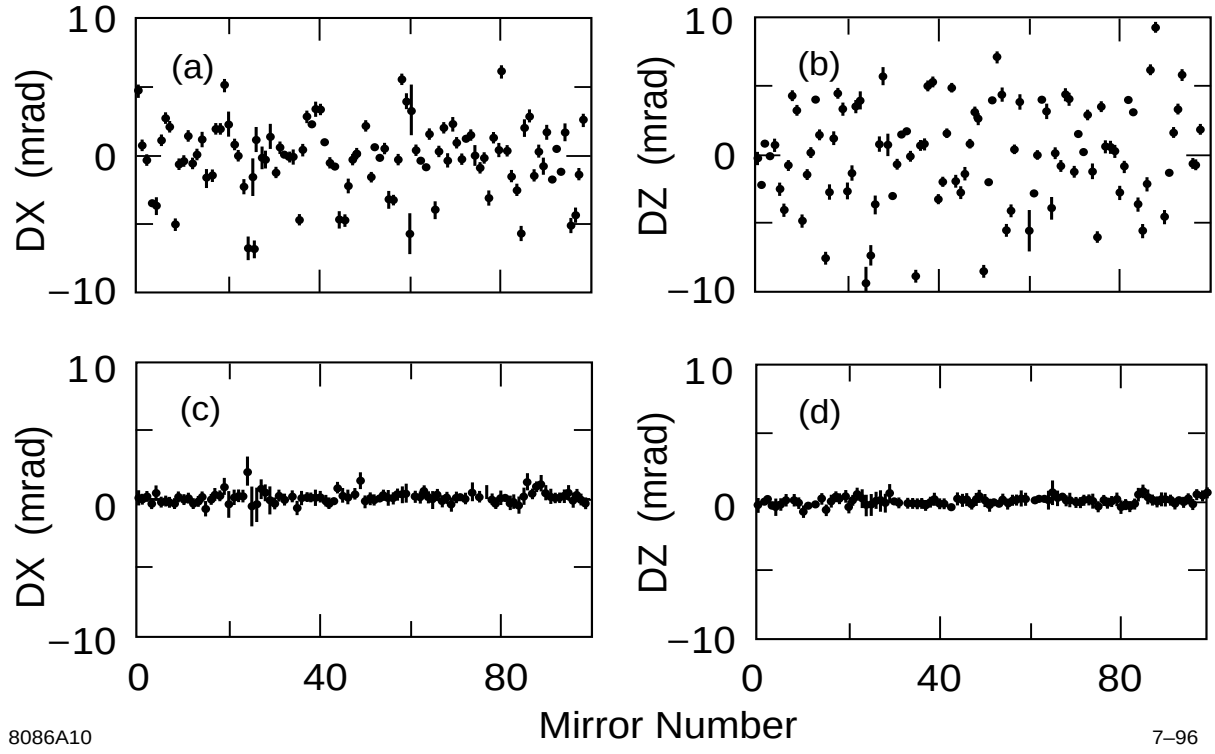

Figure 5.11: The average shift of ring centers in TPC-x (a) and TPC-z (b) for mirrors 0-100. The results of the fits after mirror alignment are shown in (c) and (d).

expected Cherenkov angle, and a background term[1]. The background includes the effects of Cherenkov radiation from other tracks in the event as well as constant term normalized to the number of hits in the TPC in question that is not associated with any tracks.

Particle separation is based upon differences between logarithms of these likelihoods, $\mathcal{L}_i = \ln L_i$. In the "standard" cut, we define a particle to be identified as type i if $\mathcal{L}_i$ exceeds both of the other log-likelihoods be at least 5 (3), for the liquid (gas) analysis.

$$\mathcal{L}_i - \mathcal{L}_j > 5(3) \quad \& \quad \mathcal{L}_i - \mathcal{L}_k > 5(3) \quad (i \neq k,\ i \neq j) \tag{5.7}$$

The difference of log-likelihood 5 (3) corresponds to 3.2σ (2.4σ) particle separation.

[1] a detailed discussion in Appendix A

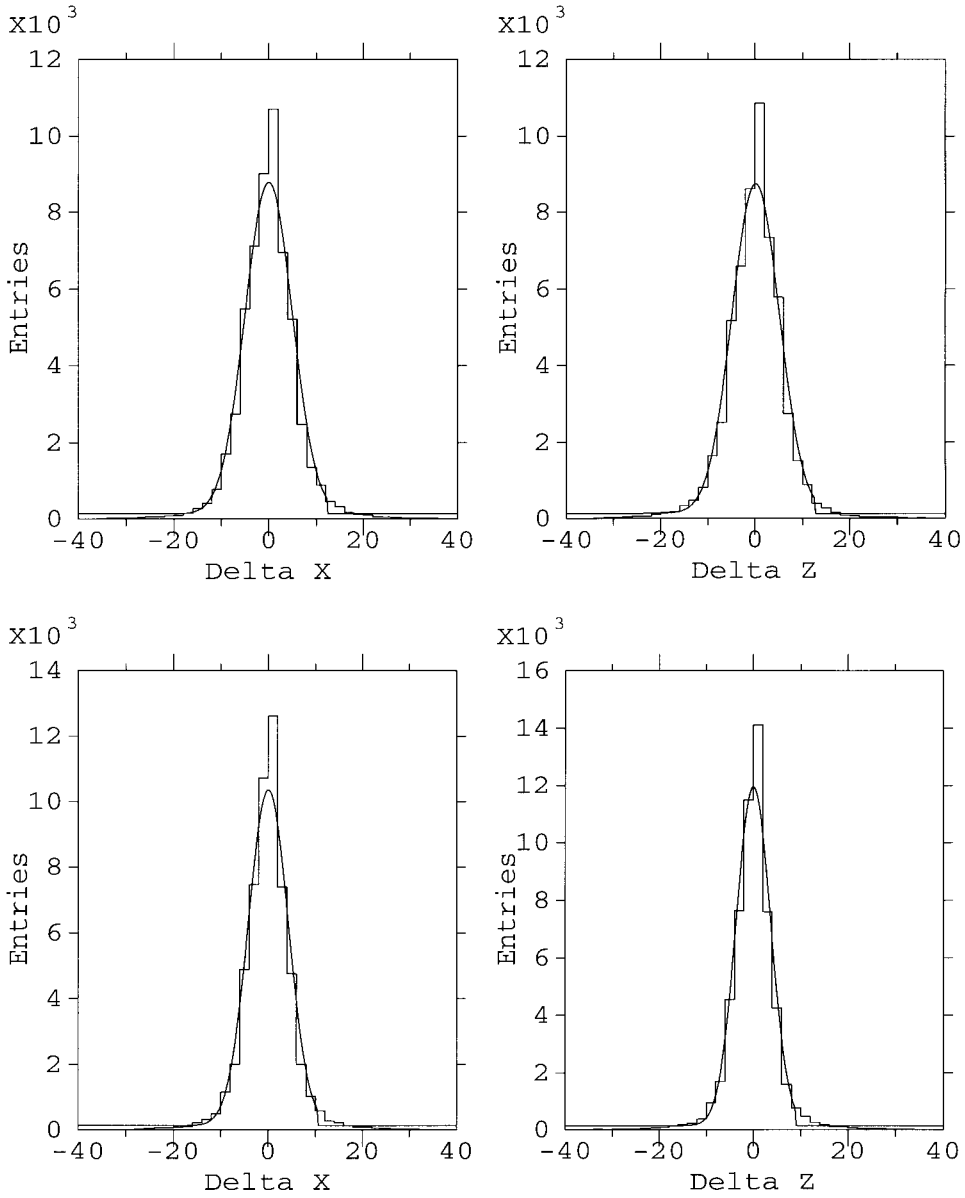

Figure 5.12: Inclusive shift of Cherenkov ring center in TPC-x and TPC-z for before (top two) and after (bottom two) mirror alignment. The curves are the result of a gaussian+constant fit.

5.5 CRID performance

The tracks from selected $K_s \to \pi^+\pi^-$ decays in hadronic events and from $Z^0 \to \tau^+\tau^-$ events are used to calibrate the identification efficiency [58]. The pion identification efficiencies for data and the Monte Carlo are shown in Figure 5.13. The simulation describes the momentum dependence well and reproduces the measured efficiencies to within $\sim 3\%$ [8]. By fitting curves to data and Monte Carlo efficiencies from K_s and τ samples, corrections were derived to Monte Carlo hadronic efficiencies for kaons and protons as well as pions.

Figure 5.14 shows the identification efficiency matrix. After CRID alignment study including TPC and mirror alignment described in 5.2 and 5.3, we have achieved great particle identification efficiency. For both liquid and gas, the efficiency curve rises to typically $\geq 80\%$, then falls down as the ring radius becomes indistinguishable from the next heavier species. Misidentification is as high as $\sim 8\%$. This efficiency depends on how we select the input sample and what criteria we use to define identification [8, 57]. In this efficiency matrix, we use the selection requirements, which is described in Section 7.1, for high momentum $K^{\pm}$ tags for A_s measurement.

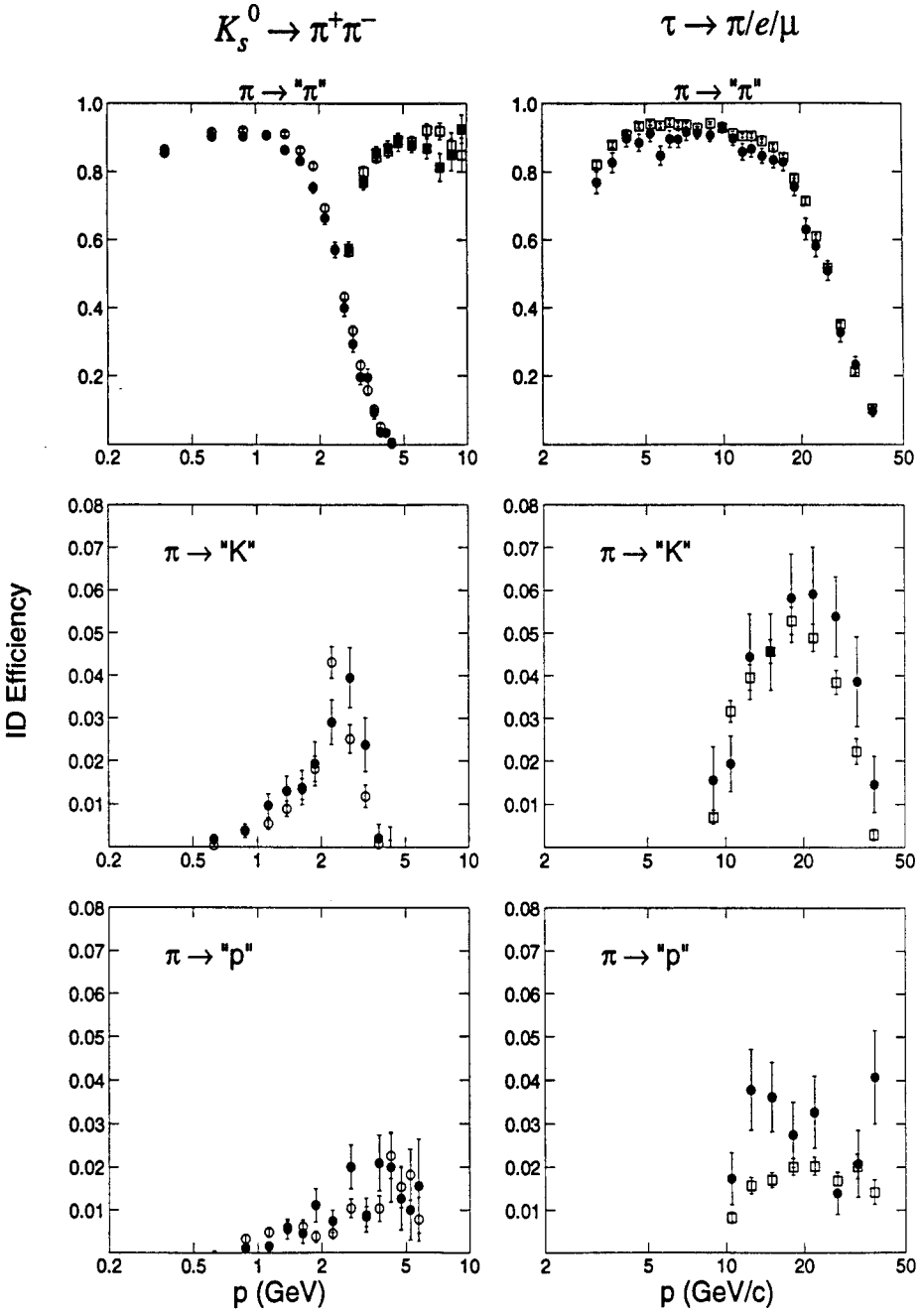

Figure 5.13: Identification efficiencies for charged pions measured with tracks from K_s and τ decays in the data (solid symbols). The open symbols are for the same analysis of simulated samples. The circles are for the liquid analysis and the squares for the gas analysis.

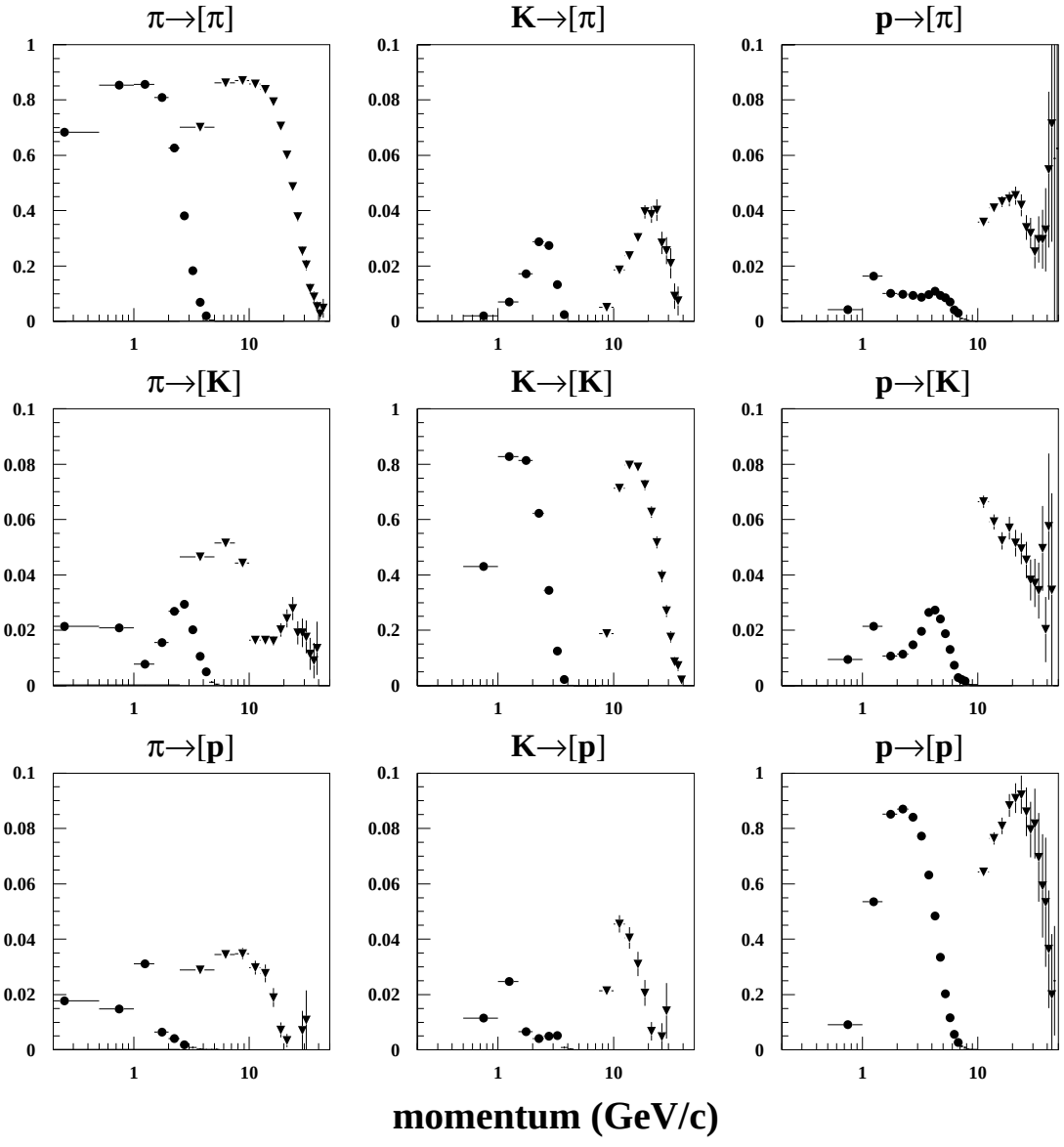

Figure 5.14: The matrix of hadronic particle identification efficiencies, as predicted from CRID simulation, is shown as a function of momentum. The circle points are those coming from the liquid radiator, and the triangle points are those from gas radiator. $A \rightarrow [B]$ means a true track A is identified as B.

Chapter 6

Event Selection

This chapter describes the SLD triggers, the hadronic event selection, and the flavor tagging. Also, the study of tagging initial quark flavor is performed in order to enhance $Z^0 \to s\bar{s}$.

6.1 The SLD triggers

The first stage of event selection takes place in the triggering of the detector which is applied online before the data is read out from the detector. The trigger criteria and the summary are described in detail in [59], and summarized here. The SLD has several independent triggers; energy trigger, charged tracking trigger, Bhabha trigger, and combinations of these triggers. In addition, there is a random trigger, which periodically reads out from the entire detector regardless of its contents, and is used for the background overlay events.

The energy trigger requires that the total deposited energy is greater than 8 GeV for the EM and/or HAD calorimeter towers in the LAC. Only the energy in towers above a given threshold are recorded. The thresholds are defined to be 60 ADC counts for the EM towers (corresponding to 246 MeV) and 120 ADC counts for the HAD towers (corresponding to 1.296 GeV) Prior to October 1994, the calorimeter systems (LAC, WIC, LUM) were the only detector elements read out, when this trigger was fired, Since then, the entire detector is used to read out data for each energy trigger.

The charged track trigger was based on pattern map of the hit cells of CDC when a charged track with momentum greater than 250 MeV/c passes through the CDC. The hit

cell is taken if a cell whose 6 of 8 sense wires in the cell have pulses above a given threshold. Those events containing two tracks passing through at least 9 superlayers of the CDC and lying roughly 120° apart were passed by this trigger, and all of SLD was read out if it fired.

The "hadron" (HAD) trigger is a combination of the previous two triggers, as it required one charged track of 9 or more superlayers and a large energy deposition in the LAC. As it was expected that most Z^0 events would satisfy this trigger, the entirety of SLD was read out when this trigger was satisfied. The combined efficiency of the three hadronic triggers (energy, track, hadron) is estimated to be $\geq 96\%$ for accepting hadronic Z^0 decays [60].

The "wide-angle" Bhabha (WAB) trigger was designed to insure that all wide-angle e^+e^- pairs were recorded, even those at angles where the track stubs in the CDC were not long enough to satisfy the track trigger requirements. This trigger also initiated readout of all of SLD. The muon trigger required a combination of a charged track in the CDC and hits in opposite WIC octans, as this would be the signature for a $Z^0 \to \mu^+\mu^-$ event. All of SLD was read out if this trigger was satisfied. The Bhabha trigger required to have a total energy (EM scale) in the EM2 section of the LUM to be above 12.5 GeV in both the north and south detectors, where the energy sum is more than 1.25 GeV. This energy deposition is what one might expect as a signature for an e^+e^- pair above some splash of background.

6.2 Hadronic Event selection

The second stage of event selection is "EIT filter" which requires that the events are relatively spherical and have good forward-backward momentum balance, using calorimetry information. It is based on three LAC quantities, $NEMHI$, EHI, and ELO with the following requirements,

1. $NEMHI \geq 10$
2. $EHI > 15$ GeV
3. $ELO < 140$ GeV
4. $EHI > 1.5 \times (ELO - 70)$,

where NEMHI is the number of EM towers passing the high threshold, EHI is the total summed energy in the EM and HAD sections for towers passing the high threshold, and ELO is the same sum, but for towers passing the low thresholds. The high(low) threshold is 60(8) counts for EM and 120(12) counts for HAD sections. The combined trigger and EIT filter efficiency for a hadronic Z^0 decays. is estimated to be $\sim 93\%$ [60].

In order to reduce the events applied EIT filter to a sample of hadronic events useful for physics analysis, we apply cuts designed to select events contained within the fiducial region of the SLD detector. Since we use charged tracks as a basis for much of the analysis, we define "good" charged tracks with the following criteria:

- transverse momentum relative to the beam axis $p_t > 150$ MeV/c
- total momentum $|\vec{p}| < 50$ GeV/c
- track polar angle $|\cos\theta| < 0.8$
- distance of closest approach in the xy plane $(doca_{xy}^{IP}) < 5$ cm
- distance of closest approach in the rz plane $(doca_{rz}^{IP}) < 10$ cm
- χ^2 per degree of freedom of the CDC track fit $\chi^2/DOF < 5$
- the number of CDC hits on the track $N_{hits} > 40$

For each event, these criteria define a set of tracks for the event. Then, a hadronic Z^0 decays is defined with the following three criteria:

- the angle of thrust axis relative to the beam direction $|\cos\theta_{thrust}| < 0.71$
- $E_{vis} > 20$ GeV, where the total visible energy calculated from the charged track assuming all tracks to be pions
- number of charged tracks ≥ 5

The thrust axis direction is determined from calorimeter clusters. This is to avoid biasing the thrust axis near the edge of acceptance of the CDC because the angular acceptance of the CDC is smaller than that of the calorimeter. The overall acceptance for hadronic Z^0

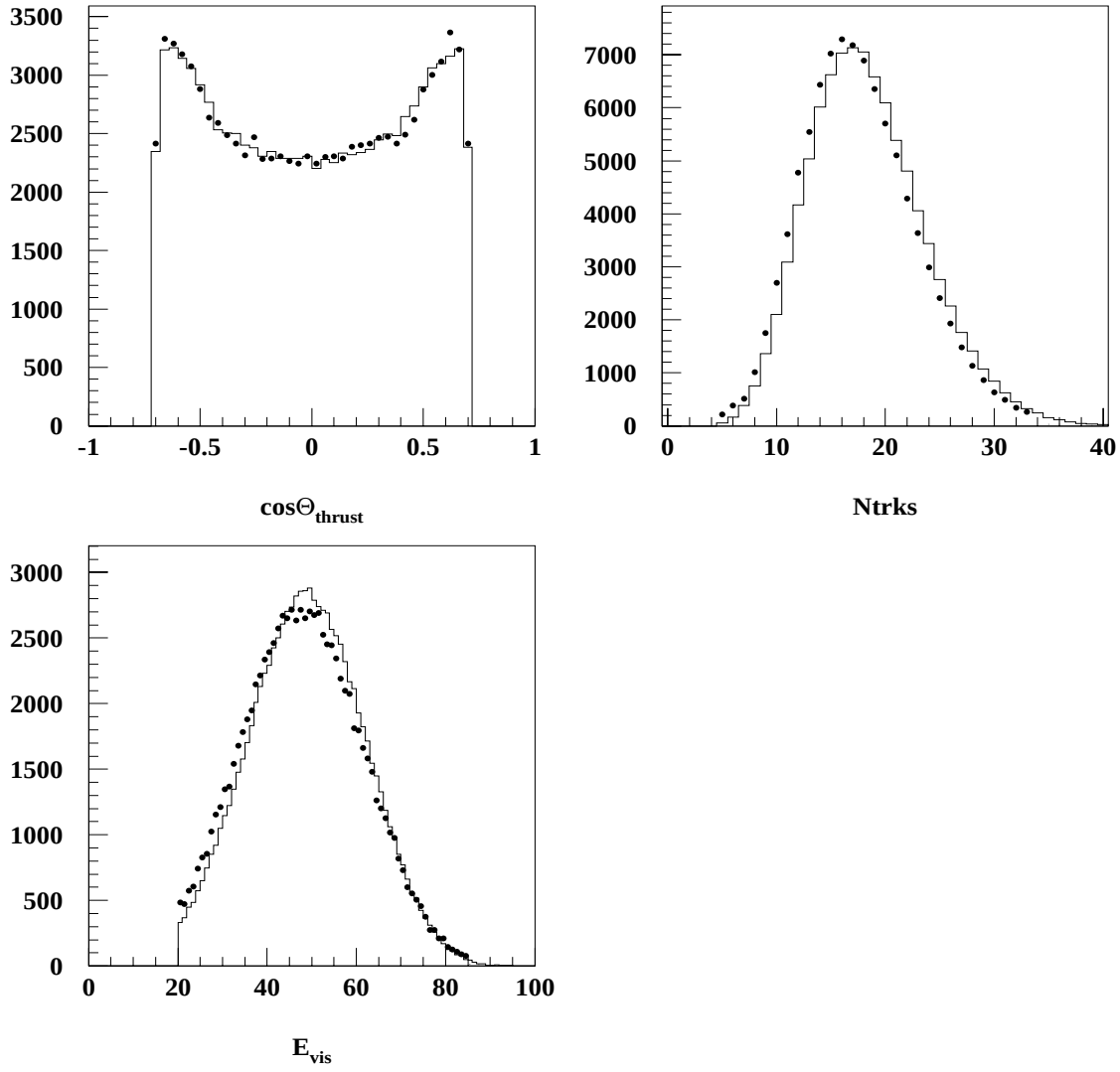

Figure 6.1: Data (dots) and the Monte Carlo (histogram) comparison for selected events.

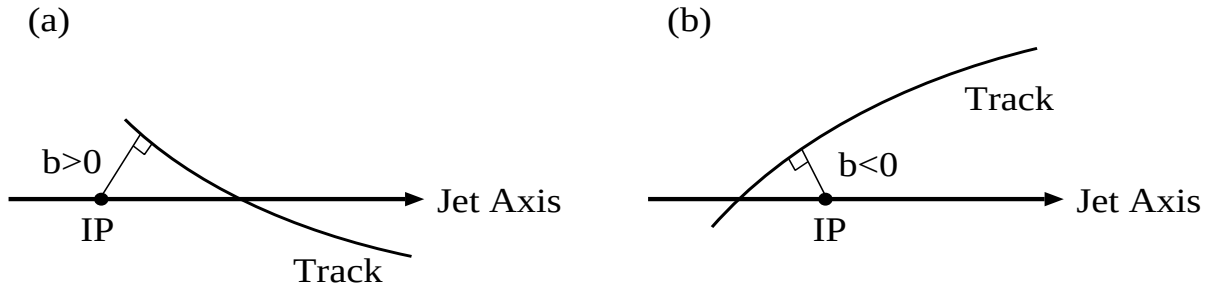

Figure 6.2: Definition of signed impact parameter. Tracks which cross the jet axis (a) "downstream" and (b) "upstream" of the IP are given positive and negative impact parameters respectively.

decays is $\sim 61\%$, with losses mainly due to the thrust axis cut. After the selection, the total numbers of hadronic events are 93729 for 1993-95 SLD runs and 309750 for the Monte Carlo. Figure 6.1 shows the $\cos\theta_{thrust}$, N_{trks}, and E_{vis} distributions for a comparison between the data and the Monte Carlo for some event variables. Good agreement can be seen between the data and the Monte Carlo.

6.3 Flavor tagging

The flavor tagging of the primary quarks was studied by the impact parameter technique. The SLD vertex detector which has excellent spatial resolution of tracks allows to measure impact parameter precisely. The technique is to use of the impact parameter of tracks with respect to the IP in the xy plane. The basis of the tag method, originally suggested by Hayes [61], is that tracks from the decays of mesons containing heavy quarks tend not to extrapolate back to IP. This is due to two factors; the long meson lifetimes and the large transverse momentum (p_T) relative to the meson flight direction which arises from the large available energy in the heavy quark decay. In contrast, light quarks (u, d, and s) typically produce very few tracks with significant impact parameter.

An improvement of this technique was suggested [62, 63] by introducing the signed impact parameter of the track based upon which side of the jet axis the charged track crosses. As shown in Figure 6.2, tracks crossing the jet axis in front of the IP get a positive sign, while

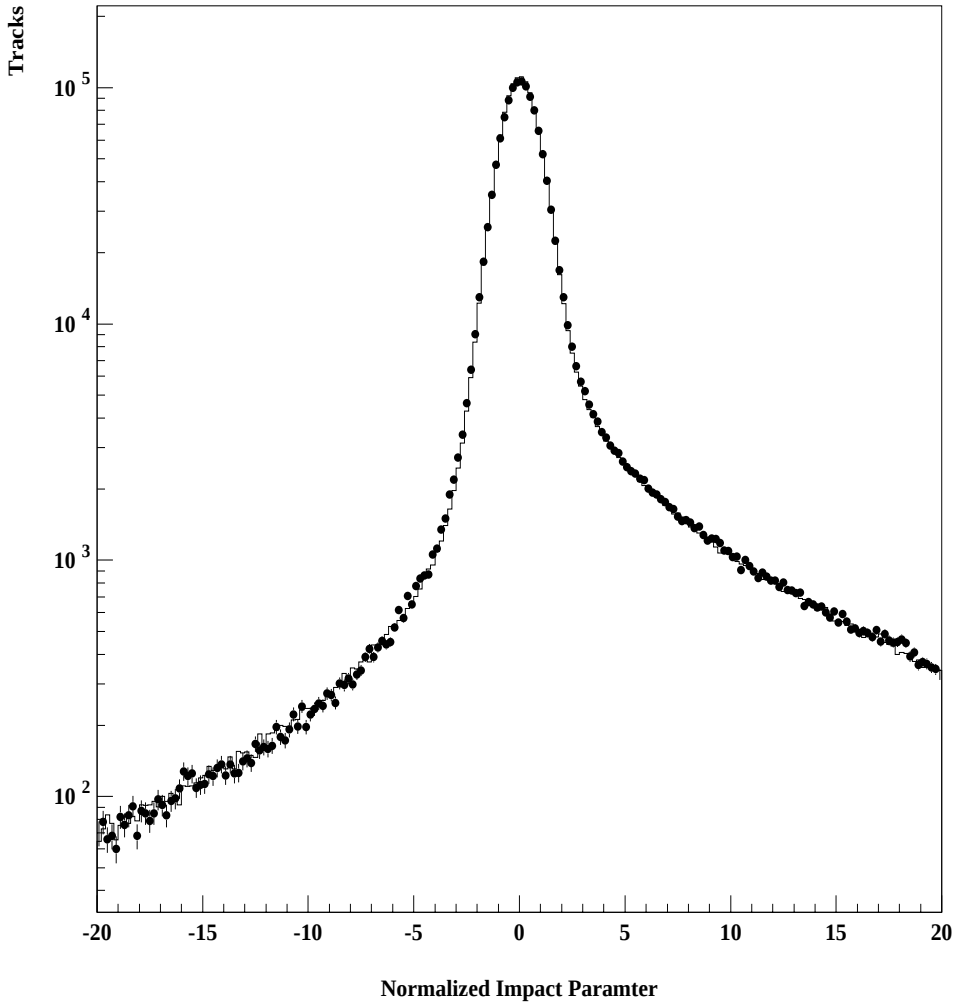

Figure 6.3: Comparison of the normalized 2D impact parameter in data (points) and the Monte Carlo (histogram).

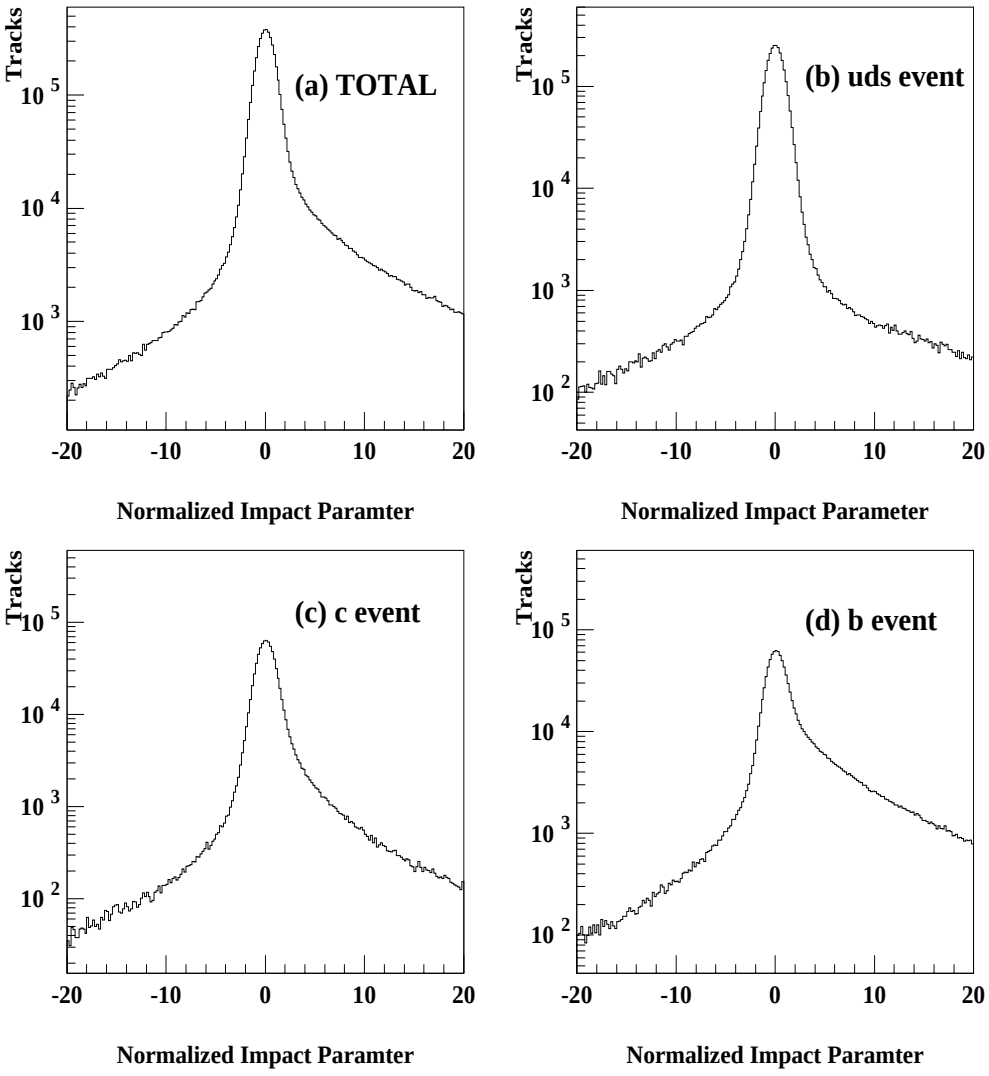

Figure 6.4: Normalized 2D impact parameter distributions estimated for each flavor in the SLD Monte Carlo.

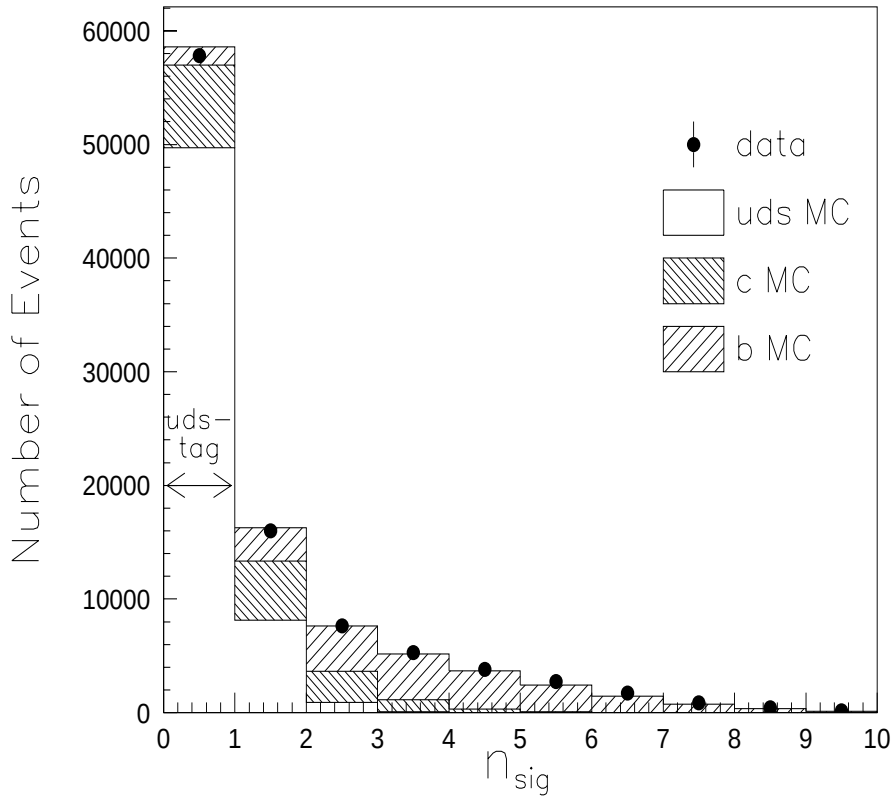

Figure 6.5: The number of tracks n_{sig} distribution. The points represent the data distribution, while the histogram represents the Monte Carlo. The flavor composition of the distribution is also shown.

those crossing behind the IP get a negative sign. Figure 6.3 shows the normalized impact parameter distribution from the Monte Carlo. A breakdown according to each flavor is showed in Figure 6.4. The track whose normalized impact parameter is greater than 3.0 is defined as *significant track*. Figure 6.5 shows the number of significant tracks per event, n_{sig}. A good agreement is observed between the data and the corresponding Monte Carlo points. The events are divided into three event samples by n_{sig} cut:

- *uds*-tagged events with $n_{sig} = 0$ (56470 events in 1993-95 data),
- *c*-tagged events with $n_{sig} = 1$ or 2 (22844 events),

- b-tagged events with $n_{sig} \geq 3$ (14415 events).

The efficiency and fraction for these event tags are shown in Table 6.1 and Table 6.2. For this analysis, uds events with $n_{sig} = 0$ were selected in order to reduce the background from c and b events. There were 56470 events with $n_{sig} = 0$ for 1993-95 data sets and 189203 events in the Monte Carlo.

	$n_{sig} = 0$	$n_{sig} = 1, 2$	$n_{sig} > 2$
uds	0.849	0.149	0.002
c	0.444	0.472	0.084
b	0.080	0.333	0.587

Table 6.1: Estimated event efficiencies for flavor tags.

	$n_{sig} = 0$	$n_{sig} = 1, 2$	$n_{sig} > 2$
uds	0.846	0.371	0.009
c	0.125	0.333	0.100
b	0.029	0.296	0.891

Table 6.2: Estimated event fractions for flavor tags.

Chapter 7

Strange Particle Tags

From the sample of the light flavor events selected with the impact parameter technique, $Z^0 \to s\bar{s}$ events are selected with high momentum $K^{\pm}$, Λ, and K_s^0. A high purity sample of $K^{\pm}$ is tagged using CRID. The $\Lambda^0/\bar{\Lambda}^0$ and K_s^0 were reconstructed in the $p\pi$ and $\pi^+\pi^-$ modes respectively, and the CRID identification of proton/anti-proton was used to obtain a pure sample of $\Lambda^0/\bar{\Lambda}^0$. In this chapter, details of the tagging methods for these strange particles are discussed.

7.1 $K^{\pm}$ tags

The charged kaon identification is based upon the CRID likelihood method described in Section 5.4. As shown in Figure 5.14, The CRID identification efficiency for charged kaons has a gap in the momentum range between 3 and 9 GeV/c. This is due to the limited momentum coverage for the liquid and gas radiators. Since the $s\bar{s}$ events produce a large fraction of the high momentum charged $K^{\pm}$ as discussed in Section 2.4, we use only the gas system whose momentum threshold for charged kaons is 9 GeV/c. Now, we focus on charged $K^{\pm}$ identification for the gas radiator.

In addition to good track selection described in Section 6.2, we apply to the CRID cuts for selected tracks to obtain particles identified with good quality;

1. Event Selection

   This selection requires the data taking period in which the barrel CRID was operational.

Cut	loss (%)
HV ON	9.1
Valid drift velocity	1.9
$\lvert\cos\theta\rvert < 0.68$	6.9
Tracks in bad TPC	2.4
NO liquid ring or track matching	1.2

Table 7.1: Losses due to extra CRID event and track selection. The losses are calculated by applying each cut independently.

- Barrel CRID high voltage ON.
- Good drift velocity calibration. Due to hardware problems with the Xe flashlamps in some periods of 1993 run, the drift velocity was not calibrated correctly. This requirements only applied for a part of 1993 data.

2. Track Selection

   The track selection is made in order to decrease the mis-identification by mis-tracking.

   - Track should have polar angle $\lvert\cos\theta\rvert < 0.68$. The value comes from the acceptance of the gas radiator and mirrors.
   - Removing tracks in the TPC which has some troubles, such as high voltage off or electronics problem.
   - Since the momentum coverage of the gas radiator is above that of the liquid radiator, tracks which have the gas ring are above the threshold in the liquid and should have the liquid rings to be detected. Therefore, we require gas tracks to have liquid Cherenkov ring.
   - Ionization deposit presents in a CRID TPC within a region of 3 cm from the extrapolated position of the track.

The loss rates of events and tracks from these CRID cuts are shown in Table 7.1.

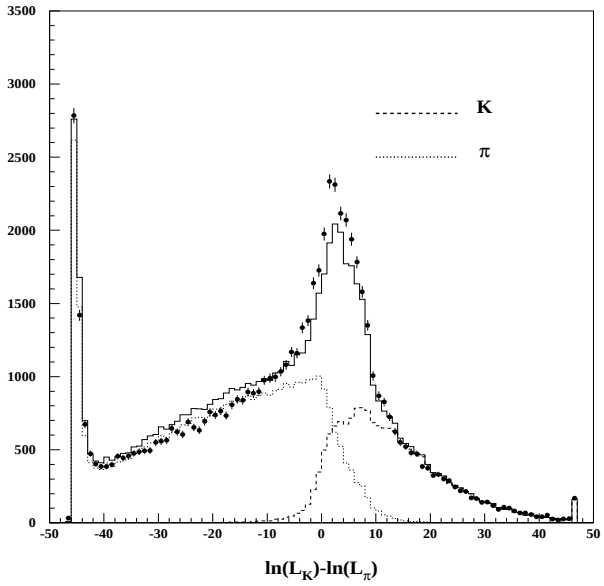

Figure 7.1: The difference of log-likelihood for $K^{\pm}$ and $\pi^{\pm}$, $\mathcal{L}_K - \mathcal{L}_\pi$. The points are the results for real data and the histograms are for the Monte Carlo. The dashed-line represents the Monte Carlo true $K^{\pm}$ and the dotted-line represents the Monte Carlo true $\pi^{\pm}$.

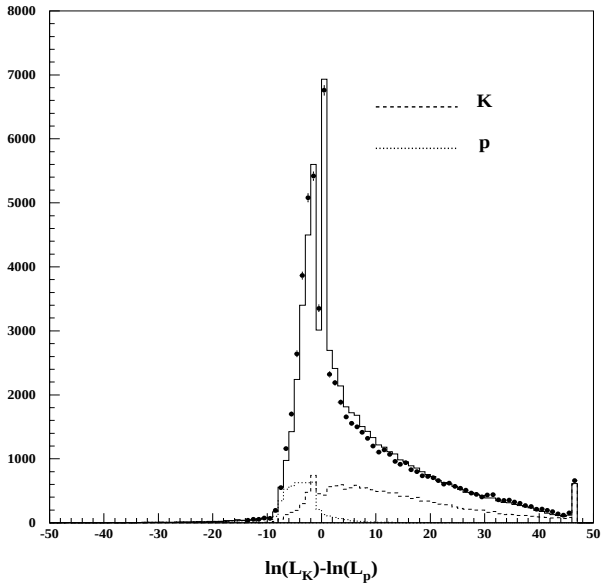

Figure 7.2: The difference of log-likelihood for $K^{\pm}$ and $p/\bar{p}$, $\mathcal{L}_K - \mathcal{L}_p$. The points are the results for real data and the histograms are for the Monte Carlo. The dashed-line represents the Monte Carlo true $K^{\pm}$ and dotted-line represents the Monte Carlo true $p/\bar{p}$.

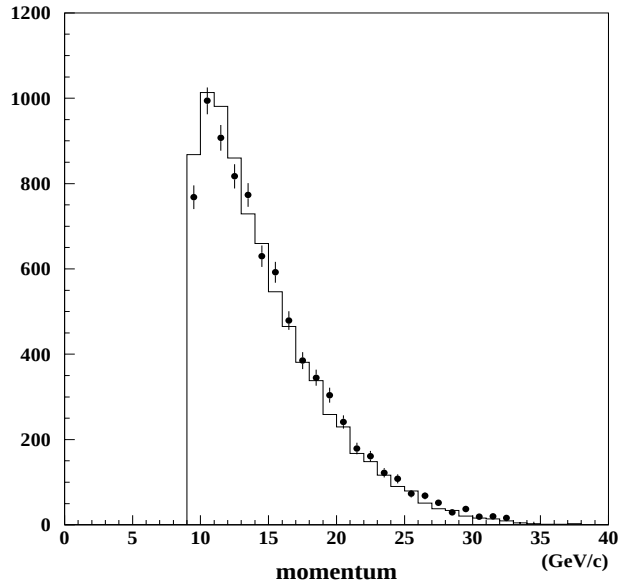

Figure 7.3: The momentum spectrum of tagged charged kaons. The points show the result for the data and the histogram shows the Monte Carlo result. The momentum below 9 GeV/c^2 is cut off due to the threshold of the CRID gas radiator.

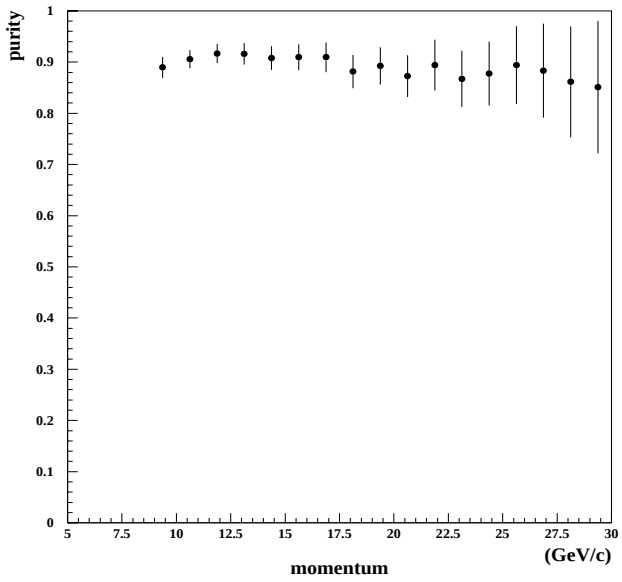

Figure 7.4: The purity of $K^{\pm}$ identified by CRID gas system as a function of track momentum. This is estimated by the SLD Monte Carlo

For tracks passing these cuts, likelihood functions L_i $(i = \pi, K, p)$ are calculated for each hypothesis. The track is tagged as charged kaon if the track satisfies the following condition.

$$\mathcal{L}_K - \mathcal{L}_\pi > 3 \quad \& \quad \mathcal{L}_K - \mathcal{L}_p > 3 \tag{7.1}$$

where $\mathcal{L}_i = \ln L_i$. Figure 7.1 and Figure 7.2 show the distributions of $\mathcal{L}_K - \mathcal{L}_\pi$ and $\mathcal{L}_K - \mathcal{L}_p$ for good quality tracks. Good agreement can be seen between the data and the Monte Carlo. In 1993-95 *uds* tagged sample, we tagged 8128 $K^{\pm}$ which have momentum above 9 GeV/c. The momentum spectrum of tagged kaons is shown in Figure 7.3. The Monte Carlo results agree with the data points. The charged kaons are tagged with up to 80% efficiency and the mis-identification of pions as kaons is a few percent, as shown in Figure 5.14. The purity of the tagged $K^{\pm}$ as a function of momentum, estimated by the Monte Carlo, is shown in Figure 7.4. The average purity over the momentum range is about 90%.

In this sample, $K^{\pm}$s from ϕ^0 decays are included. Although high momentum ϕ^0 are likely to be produced in $s\bar{s}$ events, these tracks do not provide sign information of the primary $s/\bar{s}$ quark. Since the sign of primary s quark is determined by the sign of charged kaon in this analysis, charged kaons from the decay of ϕ^0s were removed with the following procedure : We form $\phi^0 \to K^+K^-$ candidates using pairs of oppositely charged tracks satisfying loose CRID cuts :

1. HARD cut:
$$\mathcal{L}_K - \mathcal{L}_\pi > 3 \quad \& \quad \mathcal{L}_K - \mathcal{L}_p > -3.$$
2. SOFT cut:
$$\mathcal{L}_K - \mathcal{L}_\pi > -3 \quad \& \quad \mathcal{L}_K - \mathcal{L}_p > -3.$$

Obviously, the HARD cut is a subset of the SOFT cut, and Eq 7.1 is a subset of the HARD cut. We consider pairs in which at least one track passes the HARD cut and the other track passes the SOFT cut. Then, the invariant mass M_{KK} is calculated for such pairs. If $1.010 < M_{KK} < 1.030$ GeV/c^2, those tracks are regarded to come from a ϕ^0 decay and are removed from the charged kaon sample. In the charged kaon sample, 169 $K^{\pm}$s are identified to come from the identified ϕ^0 and removed. Finally, we tagged 7959 $K^{\pm}$s from the 1993-95 data sets and 27241 $K^{\pm}$s from the Monte Carlo *uds* sample.

7.2 V^0 tags

For the V^0 particle ($\Lambda^0/\bar{\Lambda}^0$ and K_s^0) tagging, we consider the charged decay modes ($\Lambda^0(\bar{\Lambda}^0) \rightarrow p(\bar{p})\pi^{\mp}$, $K_s^0 \rightarrow \pi^+\pi^-$). We consider pairs of oppositely charged tracks and use the invariant masses, $m_{p\pi^-}$, $m_{\bar{p}\pi^+}$, and $m_{\pi^+\pi^-}$, together with proton identification from the CRID and flight distance information. In this analysis, the V^0s which have momentum above 5 GeV/c are used to select the $Z^0 \rightarrow s\bar{s}$ events.

7.2.1 V^0 selection

A large combinatorial background exists for 2 prong vertexing since the average charged multiplicity in a hadronic Z^0 decay is approximately 20 tracks. In order to improve the signal-to-noise ratio for this background, several selection cuts are applied.

At first, we select the good quality tracks using the following selection criterion,

- a minimum transverse momentum of 150 MeV/c with respect to the beam direction,
- at least 40 hits in the Central Drift Chamber,
- track polar angle $|\cos\theta| < 0.8$.

Pairs of oppositely charged tracks satisfying these requirements are then combined to form V^0 candidates if the separation at their points of closest approach was less than 15 mm. A chi-square fit of the two tracks is performed to find common vertex. After finding vertex, the following cuts are applied to reject the combinatorial background :

- The vertex should be separated from the interaction point (IP) by at least $5\sigma_l$. Here, σ_l is the error in the separation length of the V^0, using the assumed flight direction, the reconstruction errors for the vertex, and the uncertainty in the IP position. The nominal errors used for the IP position are 7 μm in the plane perpendicular to the beam, and 35 μm in the electron beam direction. Figure 7.5 shows the distributions of the vertex position from the IP in the unit of the reconstruction errors for the vertex (*normalized decay length*). This cut is effective to remove the combinatorial background.

- For secondary vertices reconstructed outside the Vertex Detector, candidates are rejected if there are two or more VXD hits consistent with either of the two charged tracks.

- In the plane perpendicular to the beam, the associated angle between the momentum vector sum of the two charged tracks and line joining the IP to the decay vertex (association angle) is required to be less than $\kappa \cdot (2 + 20/p_t + 5/p_t^2)$ mrad. Here, p_t is in units of GeV/c. Figure 7.6 shows the relationship between association angle and p_t for all V^0 candidates. Also the plots for the combinatorial background, $\Lambda^0/\bar{\Lambda}^0$, and K_s^0 predicted by the Monte Carlo are shown. From the plots, the coefficient κ was determined to be 1.75 for $\Lambda^0/\bar{\Lambda}^0$ and 2.5 for K_s^0 candidates.

For V^0 candidates, we calculate two invariant masses; one is the ($m_{\pi\pi}$) assigning pion massed to both tracks, and the other is the ($m_{p\pi}$) assigning proton mass for the higher momentum charged track and pion mass for the other charged track. In the invariant mass calculation, the charged tracks' momenta at the fitted vertex position are used. K_s^0 contamination in $\Lambda^0/\bar{\Lambda}^0$ sample caused a problem since the strangeness of $\Lambda^0/\bar{\Lambda}^0$ sample is used to determine initial s-quark direction. In the following, we describe the procedure to purify the $\Lambda^0/\bar{\Lambda}^0$ sample.

7.2.2 $\Lambda^0/\bar{\Lambda}^0$ tags

In order to reject K_s^0 from $\Lambda^0/\bar{\Lambda}^0$ sample, the following three sets of requirements are considered for V^0 candidates.

a)
- reject $\Lambda^0/\bar{\Lambda}^0$ candidates if $|m_{\pi\pi} - m_{K_s^0}| < 36$ MeV/c^2. This value of 36 MeV/c^{2}corresponds to 3σ in K_s^0 mass distribution.
- reject V^0 candidates if $m_{ee} < 100$ MeV/c^2. This is to remove the background from the gamma conversion process $\gamma \rightarrow e^+e^-$ (Figure 7.7).

b)
- the higher momentum charged track should be identified as a proton by

$$\mathcal{L}_{proton} - \mathcal{L}_{\pi} > \Delta$$

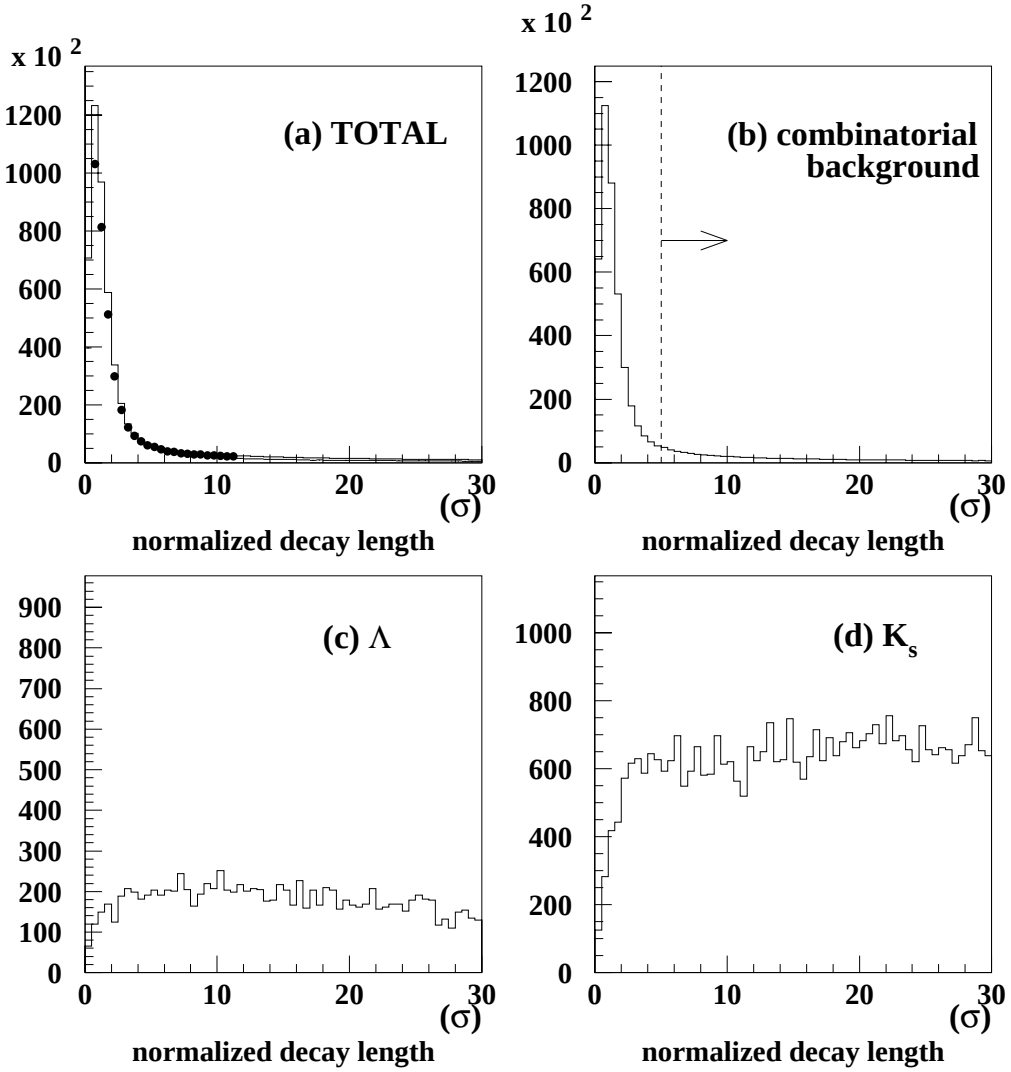

Figure 7.5: The vertex position from the IP in units of the reconstruction errors for the vertex, which is called *normalized decay length*. (a) Normalized decay length for the data (dots) and the Monte Carlo (histogram) with good agreement. The components are shown in (b) combinatorial background, (c) Λ, and (d) K_s^0 in the Monte Carlo. The tracks with the normalized decay length below 5 are cut off.

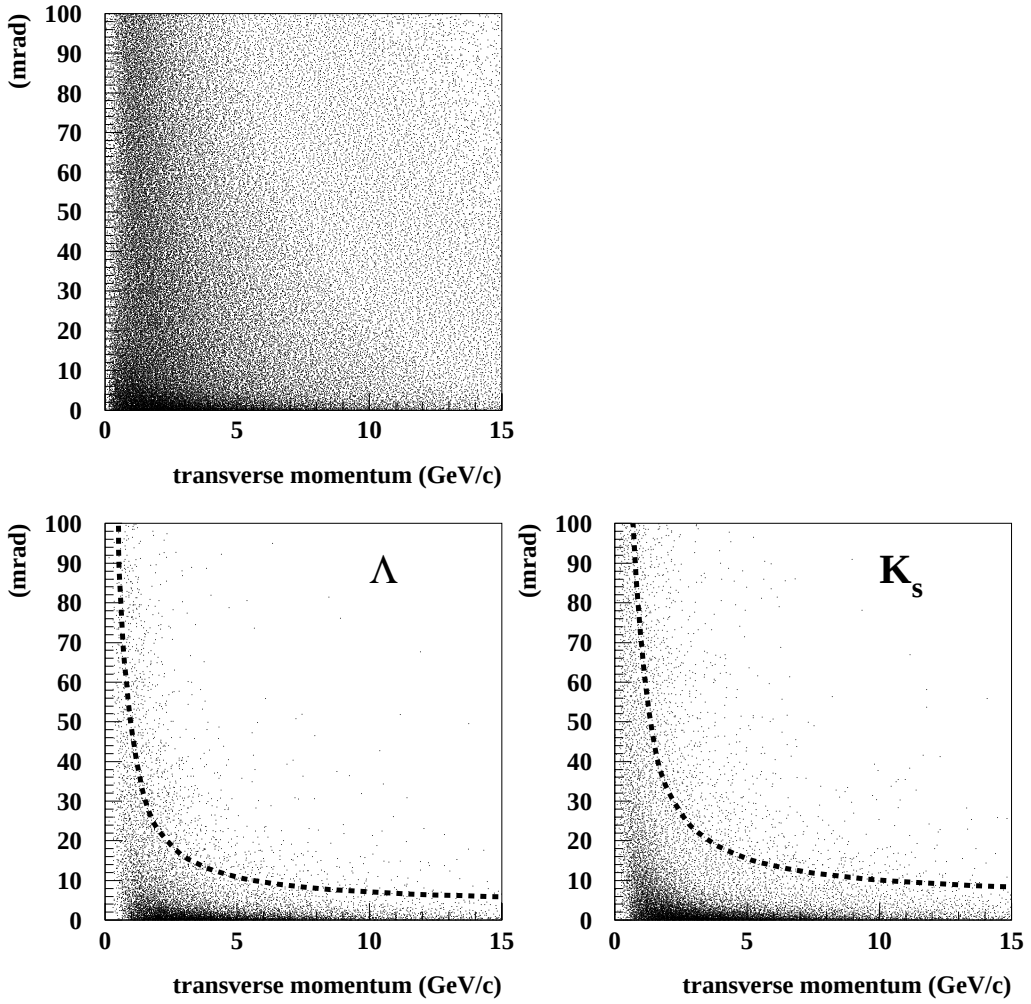

Figure 7.6: In the plane perpendicular to the beam, the angle between the vector sum of the momenta of the two charged tracks and line joining the IP to the IP to the vertex (association angle) as a function of transverse momentum. Top plot is for all V^0 candidates and the bottom two plots are for $\Lambda^0/\bar{\Lambda}^0$ and K_s^0 in the Monte Carlo. Dashed line represents the $\kappa \cdot (2 + 20/p_t + 5/p_t^2)$ and the coefficient $\kappa = 1.75$ $\Lambda^0/\bar{\Lambda}^0$ and 2.5 for K_s^0.

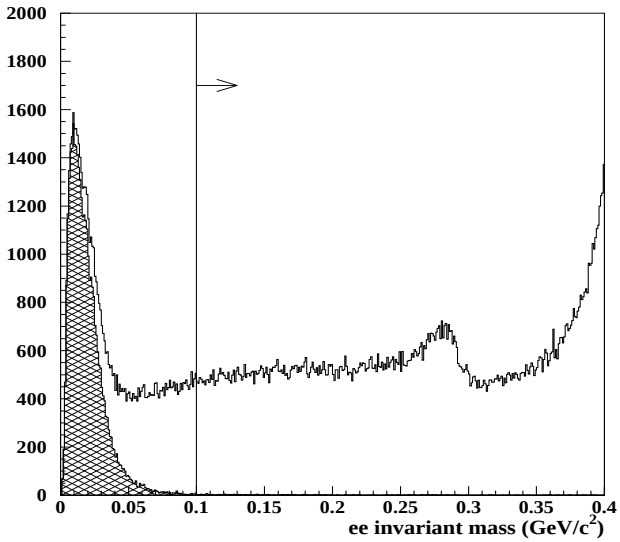

Figure 7.7: e^+e^- invariant mass M_{ee} for V^0 candidates calculated in the Monte Carlo. The hatched area represent the contribution from $\gamma \rightarrow e^+e^-$. The tracks with M_{ee} below 100 MeV/c^2 are cut off.

where $\Delta = 5$ for liquid and $\Delta = 3$ for gas system. For proton identification, we use liquid system information for the V^0 candidates with momentum below 10 GeV/c, and liquid and/or gas system whichever is available with the momentum above 10 GeV/c.

c)
- reject $\Lambda^0/\bar{\Lambda}^0$ candidates if $|m_{\pi\pi} - m_{K^0_s}| < 12$ MeV/c^2.
- $m_{ee} < 100$ MeV/c^2
- the higher momentum charged track is NOT identified as pion. "NOT pion identification" is defined as:

$$\mathcal{L}_\pi - \mathcal{L}_K < \Delta \quad \& \quad \mathcal{L}_\pi - \mathcal{L}_{proton} < \Delta.$$

The same values as "proton identification" are used for Δ. In pion rejection, we use liquid and/or system for all momentum of V^0 candidates.

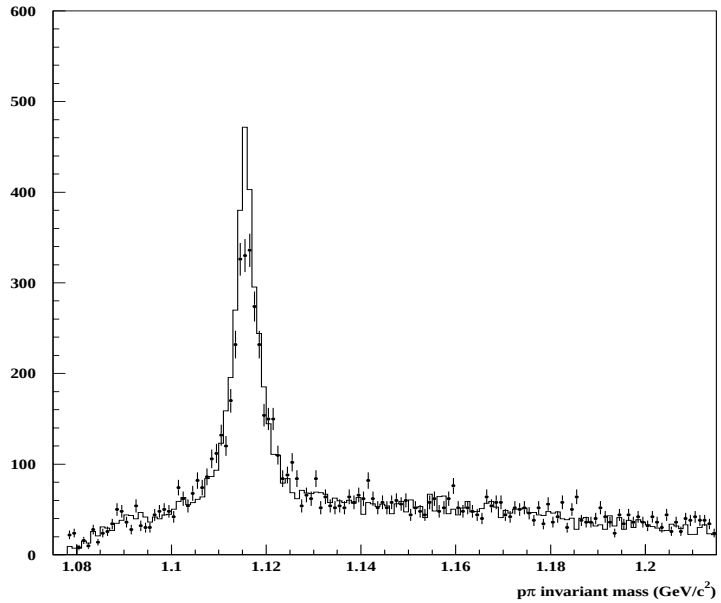

Figure 7.8: $p\pi$ invariant mass for $\Lambda^0/\bar{\Lambda}^0$ candidates which have momentum above 5 GeV/c. The dots show DATA and the histogram shows the Monte Carlo.

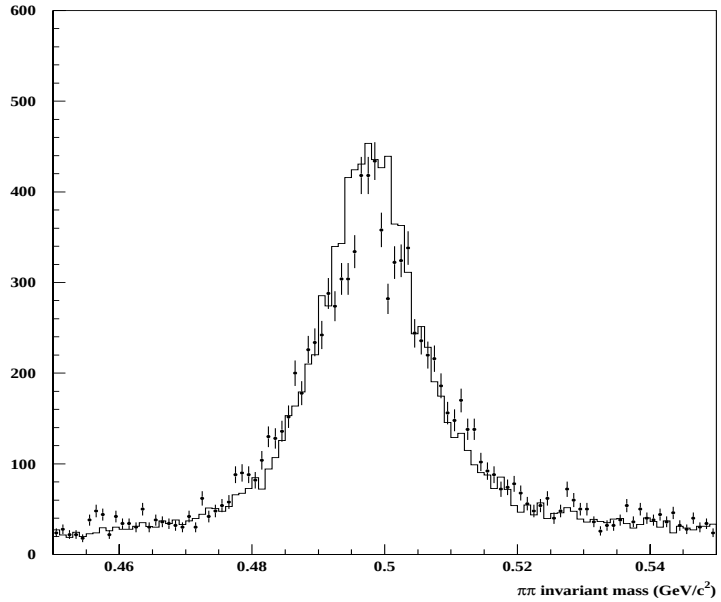

Figure 7.9: $\pi\pi$ invariant mass for K_s^0 candidates which have momentum above 5 GeV/c The dots show DATA and the histogram shows the Monte Carlo.

If a V^0 candidate satisfies at least one of these three requirements (a, b, c) with the mass window of $1.1106 < m_{p\pi} < 1.1206$ GeV/c^2, then it is tagged as a $\Lambda^0/\bar{\Lambda}^0$. The $m_{p\pi}$ invariant mass distribution is shown in Figure 7.8. In the mass window, there are 1004 $\Lambda^0/\bar{\Lambda}^0$s with $\sim 85\%$ purity in 1993-95 *uds* tagged events and 3927 $\Lambda^0/\bar{\Lambda}^0$s in the Monte Carlo events.

7.2.3 K_s^0 tags

After the above V^0 selection, additional cut is applied for K_s^0 tags, to reject the candidates which have $m_{ee} < 100$ MeV/c^2. If the invariant mass assuming π^+ and π^- for oppositely charged tracks is within the mass window of $0.4856 < m_{\pi\pi} < 0.5096$ GeV/c^2, then it is tagged as K_s^0 . The invariant mass plot, $m_{\pi\pi}$, is shown in Figure 7.9. We tagged a sample of 3369 K_s^0s with momentum above 5 GeV/c in 1993-95 *uds* tagged events with the purity $> 90\%$ and 12880 K_s^0s in the Monte Carlo events.

The momentum spectrum of the tagged $\Lambda^0/\bar{\Lambda}^0$ and K_s^0 are shown in Figure 7.10 and 7.11. For both plots, a good agreement is observed between the data and the Monte Carlo. The reconstruction efficiencies for $\Lambda^0/\bar{\Lambda}^0$ and K_s^0 are shown in Figure 7.12. These efficiencies are the ratio of the number of tagged events to the number of generated events in the Monte Carlo. The reconstruction efficiency is limited mainly by the detector acceptance (~ 0.67) and the charged decay branching fraction (0.64 for $\Lambda^0/\bar{\Lambda}^0$ and 0.68 for K_s^0).

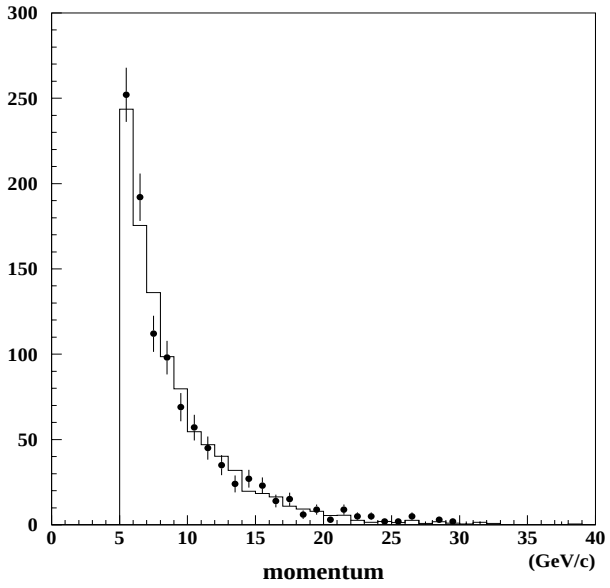

Figure 7.10: The momentum distribution of tagged $\Lambda/\bar{\Lambda}$ (momentum $p > 5$ GeV/c). The points represent the data and the histogram represents the Monte Carlo.

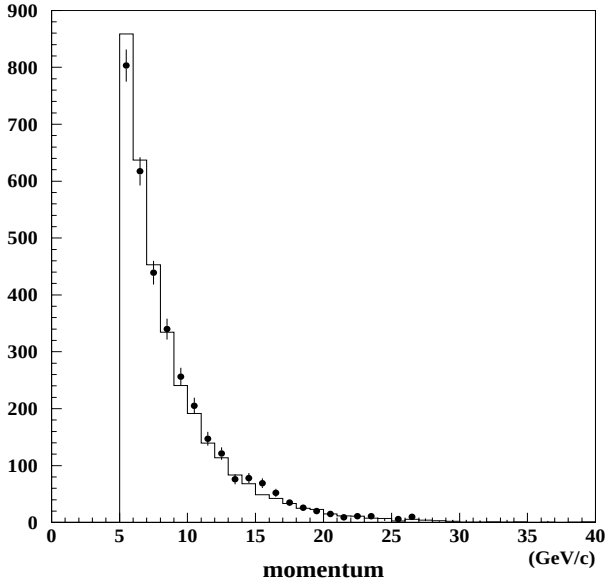

Figure 7.11: The momentum distribution of tagged K_s^0 (momentum $p > 5$ GeV/c). The points represent the data and the histogram represents the Monte Carlo.

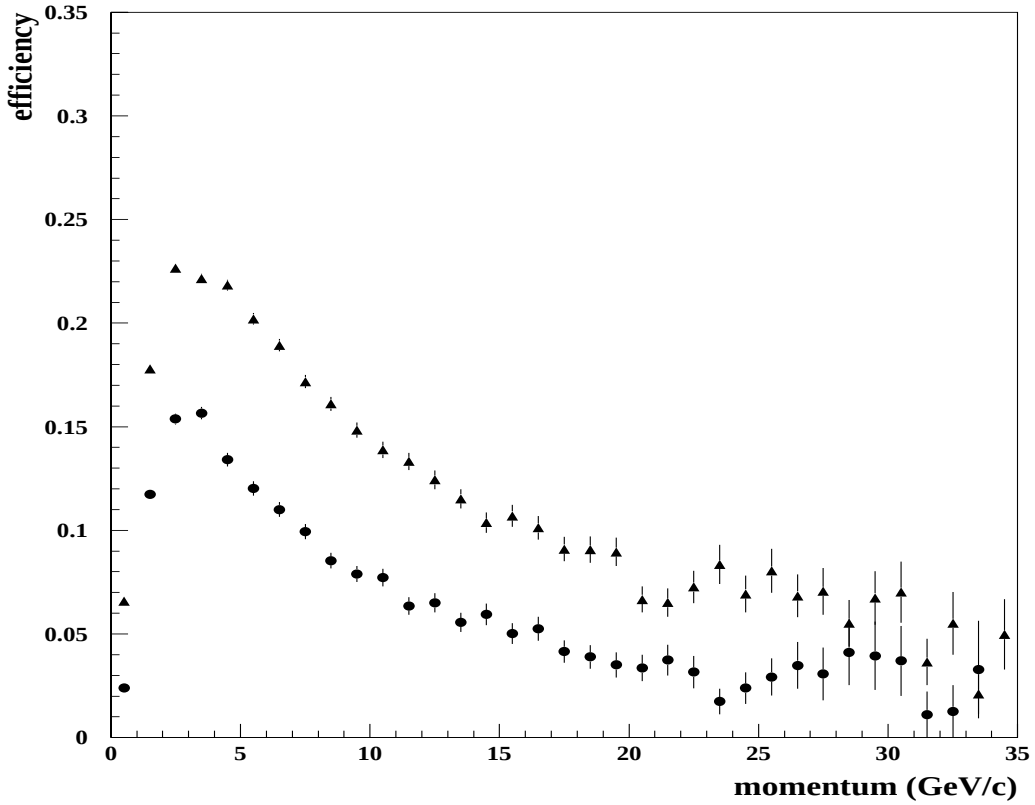

Figure 7.12: The reconstruction efficiencies for $\Lambda^0/\bar{\Lambda}^0$ (circle points) and K_s^0 (triangle points) from the Monte Carlo.

Chapter 8

The s quark asymmetry and A_s

In order to measure A_s, one must select a high purity sample of $Z^0 \to s\bar{s}$ events ans measure the s quark direction reliably. In this chapter, we discuss the $s\bar{s}$ event selection using the tagged strange particles described in the previous section, the characteristics of the selected events and their forward-backward asymmetry, and finally the parity violating parameter A_s.

8.1 $Z^0 \to s\bar{s}$ event selection

As described in Section 2.4, high momentum strange particles are likely to contain an initial s or $\bar{s}$ quark from a Z^0 decay. However, even in such events with high momentum strange particles non-$s\bar{s}$ events are substantially included. we have already rejected heavy flavor events ($c\bar{c}$ and $b\bar{b}$) by using the impact parameter flavor tagging (Section 6.3). Even if we tag a high momentum charged kaons from the uds sample, $u\bar{u}$ events contribute strongly since both $u(\bar{u})$ and $s(\bar{s})$ can be contained in charged kaon as illustrated in Figure 8.1. In $s\bar{s}$ events, the initial $s(\bar{s})$ quark picks up a $\bar{u}(u)$ from the vacuum and they form $K^-(K^+)$. Although a similar process happens in the $u\bar{u}$ case, the probability is much smaller than that for the $s\bar{s}$ events, because the ratio of the popping probability of $s\bar{s}$ to $u\bar{u}$ quark pairs is ~ 0.3[67]. Furthermore, $K^\pm$ can be decay products of $K^{*^\pm}$ and K^{*^0} mesons produced in $u\bar{u}$, $d\bar{d}$ or $s\bar{s}$ events. If we simply tagged all events with any fast strange particle, we would expect an $s\bar{s} : (u\bar{u} + d\bar{d})$ event ratio of $\sim 3/2$, not a high purity sample. However we may

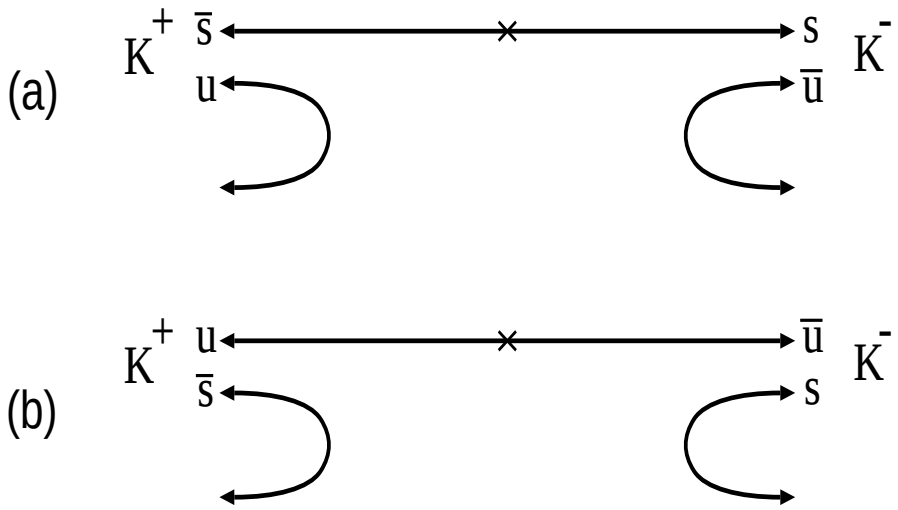

Figure 8.1: A schematic diagram of leading $K^{\pm}$ pair production in (a) $s\bar{s}$ and (b) $u\bar{u}$ events.

reduce the $u\bar{u}$ and $d\bar{d}$ event background by a double tag, requiring a fast strange particle in both hemisphere. This reduces statistics but improves systematics.

We consider events containing at least two identified strange particles. We calculate the thrust axis using calorimeter information and define two hemispheres by plane perpendicular. The rapidity of each strange particle is calculated in order to investigate the inclusive properties of jets initiated by s quarks. The rapidity y is defined:

$$y \equiv \frac{1}{2} \ln \frac{E + p_{\parallel}}{E - p_{\parallel}} \tag{8.1}$$

where $p_{\parallel}$ is the component of the particle's momentum along the thrust axis. Figure 8.2 shows the distribution of the absolute rapidity difference

$$\Delta y = |y_1 - y_2| \tag{8.2}$$

between pairs of opposite-sign (K^+K^-) and same-sign (K^+K^+, K^-K^-) charged kaons in the same event. There is a substantial excess of opposite-sign pairs at low rapidity difference. This implies that strangeness conservation in the fragmentation process is quite local when an $s\bar{s}$ pair is created from the vacuum, and the s and $\bar{s}$ appear in particles rather close to each other in phase space (Figure 8.3). For the high momentum kaon pairs in the Figure

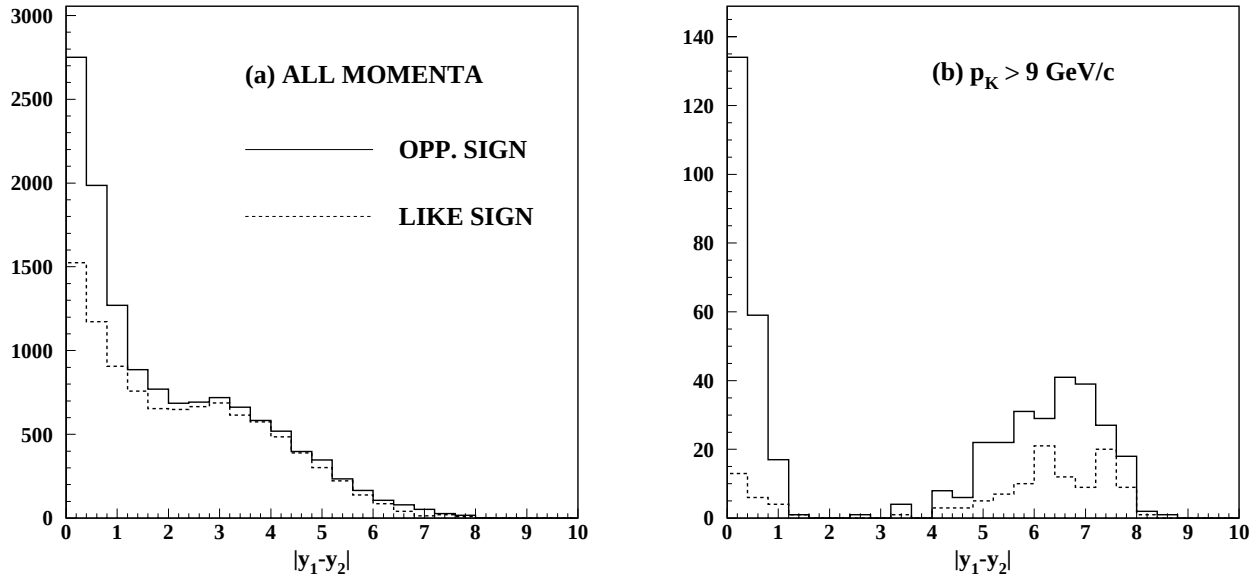

Figure 8.2: The rapidity difference Δy of pairs of opposite-sign (solid) and like-sign (dashed) charged kaons in the same event, (a) for all momenta and (b) in which both charged kaons have momentum above 9 GeV/c.

8.2(b), an additional excess of opposite-sign pairs can be seen at $\Delta y \sim 6$, as expected from events with a leading K^- in one hemisphere and a leading K^+ in the other hemisphere.

These results indicate that a charged kaon, whose momentum is relatively high, tends to be a leading kaon, since if leading charged kaons are produced by both q and $\bar{q}$ in a Z^0 decay then these two kaons must have opposite charge, whereas non-leading kaons have a random charge. As an evidence of the leading effect, this excess cannot be seen for all momenta kaon pairs (Figure 8.2(a)).

For the measurement of the left-right forward-backward asymmetry, the events with at least one tagged strange particle in each hemisphere are used. In a case of tagging two or more strange particles in a hemisphere, we used the one with the highest momentum. Since the particle direction of the known strangeness is used to determine the direction of s quark, we require at least one tagged particle to be $K^{\pm}$ or $\Lambda^0/\bar{\Lambda}^0$. If such particles are tagged in both hemispheres, we require their strangeness to be opposite. As a consequence of these requirements, we selected 532 $s\bar{s}$ events (280 for $P_e < 0$ and 252 for $P_e > 0$) from the data

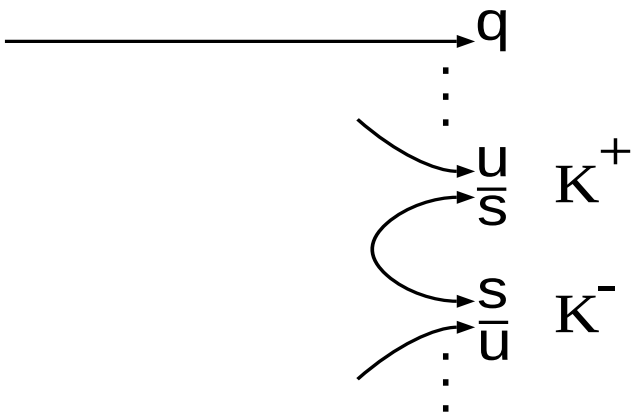

Figure 8.3: A schematic diagram of local strangeness conservation.

and 1051 $s\bar{s}$ events (585 for $P_e < 0$ and 466 for $P_e > 0$) from the Monte Carlo events[1]. Table 8.1 lists the numbers of events for each pair type.

8.2 $\tilde{A}^s_{FB}$ and A_s Results

In this section, we use the 532 $s\bar{s}$ events selected in the previous section to the study Left-Right Forward-Backward Asymmetry ($\tilde{A}^s_{FB}$) and the parity violating parameter, A_s.

8.2.1 Left-Right Forward-Backward Asymmetry for s quarks

The initial s quark direction ($\hat{u}$) is defined in terms of the event thrust axis ($\hat{t}$), the strangeness (s) and momentum ($\vec{p}$) of the tagged strange particle, by

$$\hat{u} = \frac{s(\vec{p}\cdot\hat{t})\hat{t}}{\mid \vec{p}\cdot\hat{t} \mid}. \tag{8.3}$$

Figure 8.4 shows the distribution of $\cos\theta \equiv \hat{u}_z$ for left- ($P_e < 0$) and right- ($P_e > 0$) handed electron beam. A significant production asymmetry is observed, with more s quarks

[1]As described in Section 4.1, half of events are generated with an electron beam polarization of +100%, and half with −100% in the Monte Carlo. The number 1051 represents after adjustment of the polarization and A_{LR} properly using Eq 4.1 and Eq 4.2.

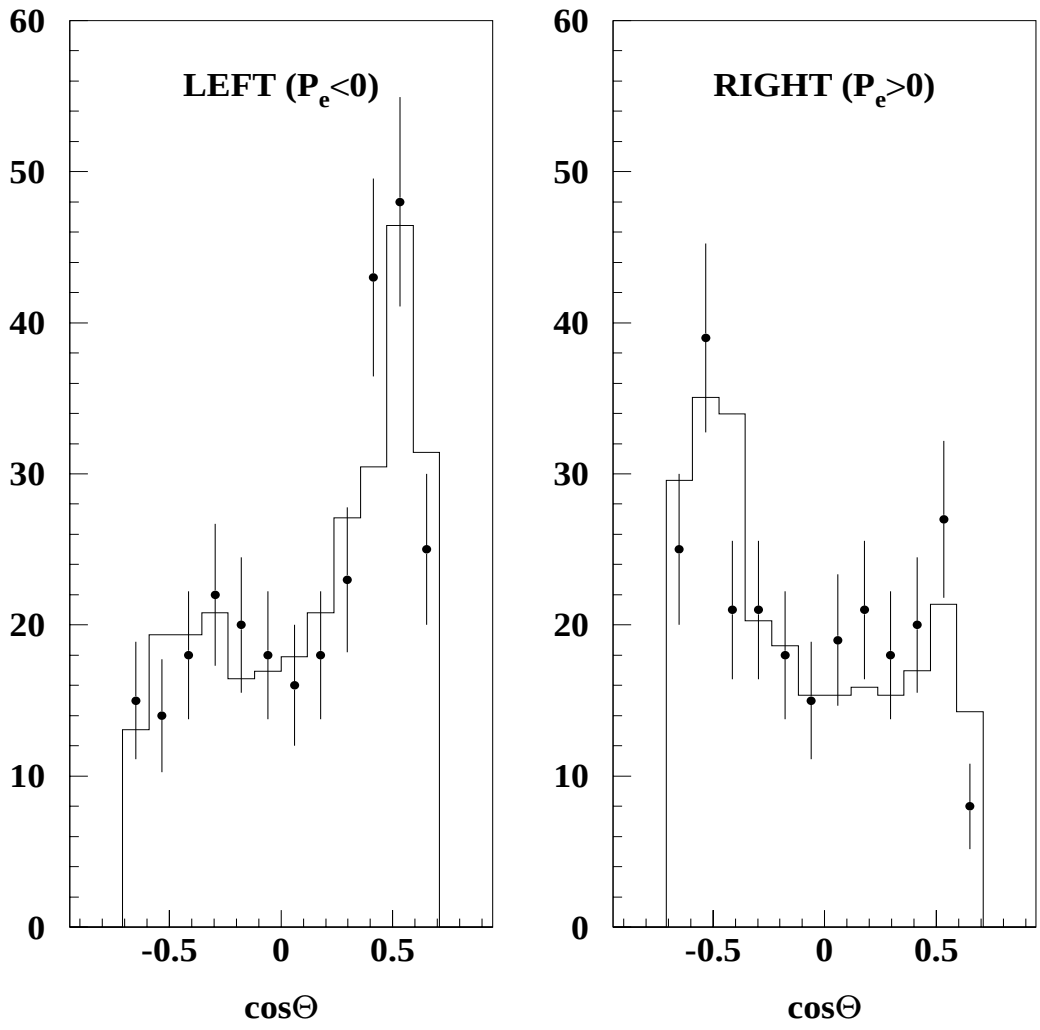

Figure 8.4: Calorimetric thrust axis $\cos\theta$, signed with the strangeness of tagged strange particles, binned separately for events created with the left-handed and right-handed electron beams. The dots shows data and the histogram shows the Monte Carlo results.

PAIR	Events	
	DATA	MC
$K^{\pm}K^{\mp}$	239	449
$K^{+}\Lambda, K^{-}\bar{\Lambda}$	40	84
$\Lambda\bar{\Lambda}$	2	9
$K^{\pm}K_s$	223	456
ΛK_s	28	53
TOTAL	532	1051

Table 8.1: The number of $s\bar{s}$ event sample for each pair.

flavor	fraction (%)
u	10.2±0.7
d	9.3±0.7
s	67.4±2.3
c	12.3±0.8
b	0.8±0.2

Table 8.2: The flavor composition of the selected $s\bar{s}$ event sample simulated by the JETSET model. The errors come from the Monte Carlo statistics.

produced at $\cos\theta > 0$ for $P_e < 0$ and $\cos\theta < 0$ for $P_e > 0$. The entries fall down at the edge bins for both plots due to thrust axis polar angle cut, $|\cos\theta| < 0.71$.

Table 8.2 shows the flavor decomposition of the 532 tagged $s\bar{s}$ events sample expected from JETSET. The non-s events are categorized into light flavor and heavy flavor backgrounds. In the LEP and many other experiments, the feature of heavy flavor events has been well studied and the physics simulator is, also, well tuned for heavy flavors. Therefore, we use the JETSET model to subtract the non-$s\bar{s}$ backgrounds from the sample. At first, heavy flavor backgrounds, c and b are estimated by the Monte Carlo. The number of entries in

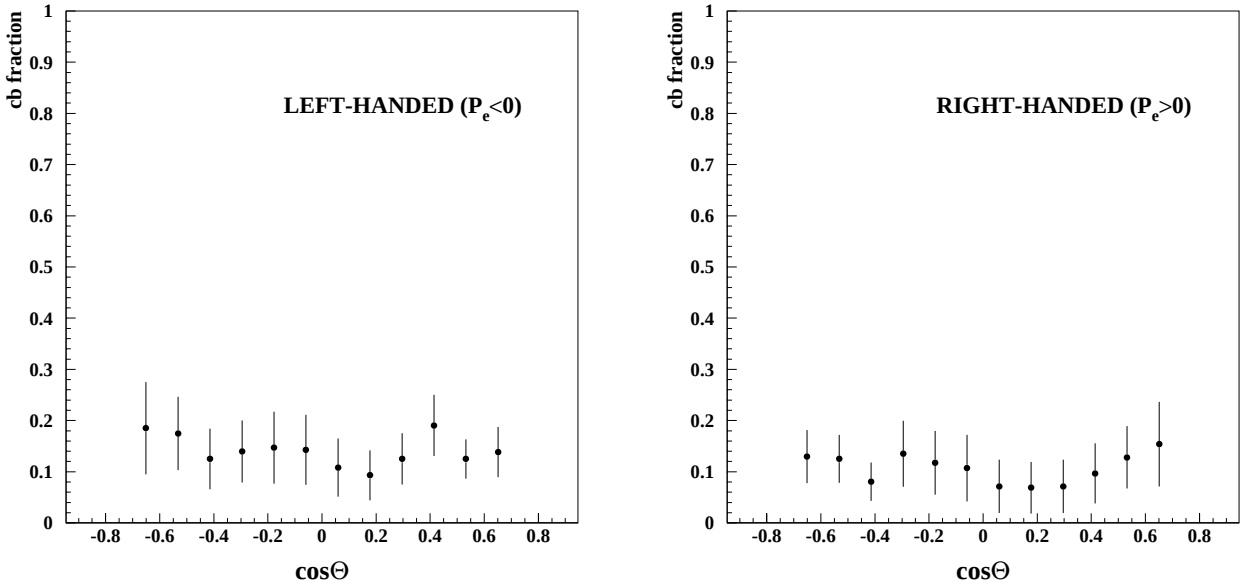

Figure 8.5: c and b fraction of selected $s\bar{s}$ events in each θ bin, for left-handed (left) and right-handed (right) electron beam. These values are estimated by the JETSET Monte Carlo.

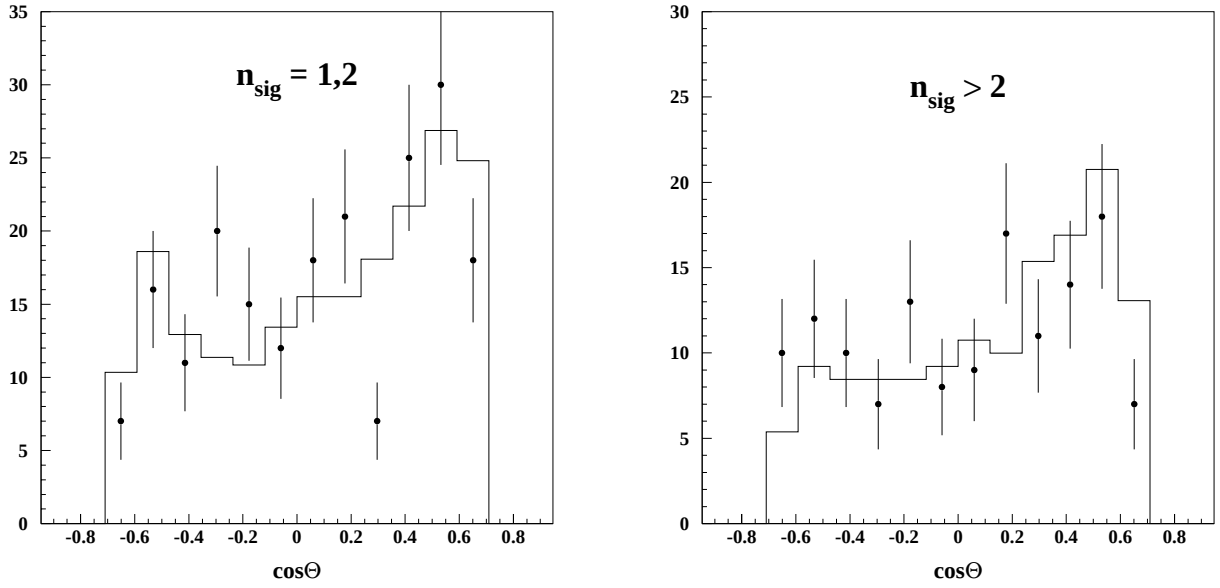

Figure 8.6: Distribution of $\cos\theta$ for the event with $n_{sig} = 1, 2$ (left) and $n_{sig} > 2$ (right). The dots shows data and the histogram shows the Monte Carlo results. The events for right-handed electron beam are added flipping the sign of θ.

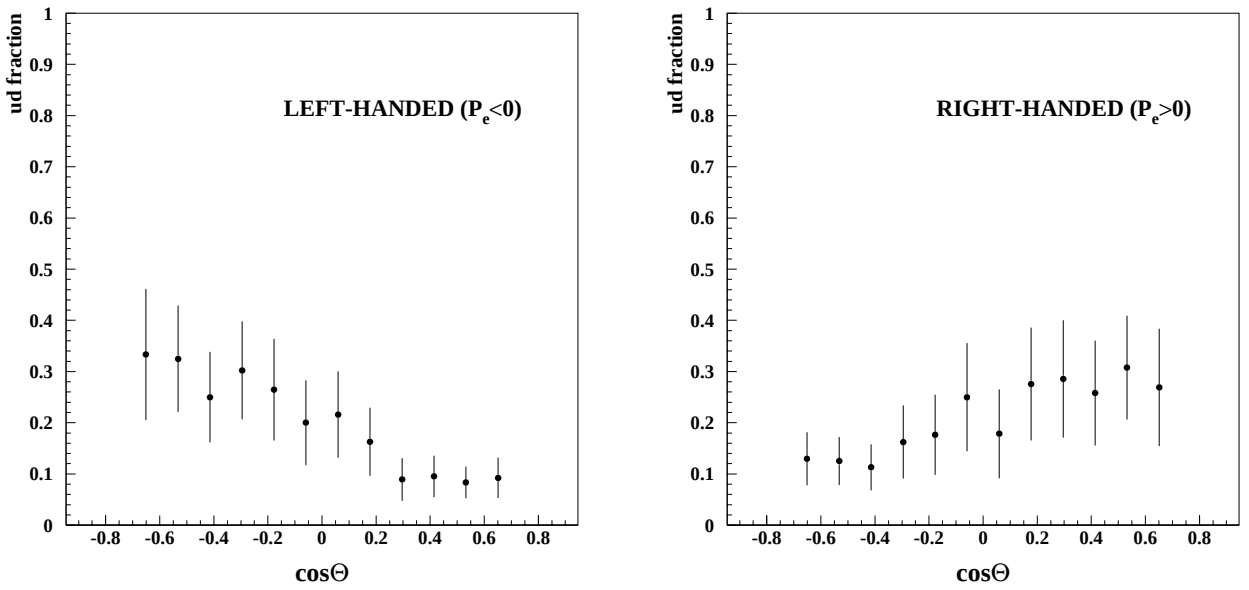

Figure 8.7: u and d fraction of selected $s\bar{s}$ events in each θ bin, for left-handed (left) and right-handed (right) electron beam. These values are estimated by the Monte Carlo.

each θ bin, $N^{total}(\theta)$ can be written by,

$$N^{total}(\theta) = N_s(\theta) + N_{ud}(\theta) + N_{cb}(\theta), \tag{8.4}$$

where $N_s(\theta)$, $N_{ud}(\theta)$, and $N_{cb}(\theta)$ are the numbers of entries in a θ bin from s, ud, and cb events respectively. Then, the cb component expected from the Monte Carlo prediction is subtracted from the selected sample, that is,

$$N_{uds}(\theta) = N^{total}(\theta)\{1 - f^{cb}(\theta)\}, \tag{8.5}$$

where $f^{cb}(\theta)$ is the c and b fraction of the entries in each θ bin, shown in Figure 8.5. The consistency between the data and the Monte Carlo prediction was checked by using c and b enhanced events with $n_{sig} = 1, 2$ and with $n_{sig} > 2$ [1]. were used. The $\cos\theta$ distribution was made for the events with $n_{sig} = 1, 2$ and $n_{sig} > 2$ with the same procedure as for uds-tagged events. Since the statistics of these events, which have high momentum strange particles, is

[1] see Section 6.3 for the definition of *significant track*.

poor, the distributions for left-handed events and right-handed events were added together:

$$N^{L+R}(\theta) = N^{Left}(\theta) + N^{Right}(-\theta), \tag{8.6}$$

where $N^{Left(Right)}(\theta)$ is the number of events in a θ bin for left(right)-handed electron beam. Figure 8.6 shows the $\cos\theta$ distribution for the events with $n_{sig} = 1, 2$ and $n_{sig} > 2$. Although the statistics of the data is poor, no obvious discrepancy between the data and the Monte Carlo can be seen.

After the cb events are subtracted by using the Monte Carlo results with $n_{sig} = 0$, the ud events remain. It is difficult to separate $s\bar{s}$ events from $u\bar{u}$ $d\bar{d}$ events since we know of no clear difference in the fragmentation and decay processes for the $u\bar{u}$, $d\bar{d}$, and $s\bar{s}$ events. In principle, the ud events can be subtracted in the same way as for the cb events using the fraction of the ud component estimated from the Monte Carlo prediction. However, we note that the fragmentation parameters in the fragmentation model for light quarks has not fixed and are still under study. Thus, the errors of parameters in the JETSET event generator are included as systematic errors for the final result.

The ud contamination is subtracted using the same equation as Eq 8.5,

$$N_s(\theta) = N_{uds}(\theta)\{1 - f^{ud}(\theta)\}. \tag{8.7}$$

The distribution of $f^{ud}(\theta)$ obtained from the Monte Carlo is shown in Figure 8.7. The corrected $\cos\theta$ distributions for the left-handed and right-handed beams are shown in Figure 8.8.

After the non-s event subtraction, the Left-Right Forward-Backward asymmetry $\tilde{A}_{FB}^{raw}$ is calculated for each θ bin by using the following equation,

$$\tilde{A}_{FB}^{raw}(\theta) = \frac{N_s^{Left}(\theta) - N_s^{Right}(\theta) - N_s^{Left}(-\theta) + N_s^{Right}(-\theta)}{N_s^{Left}(\theta) + N_s^{Right}(\theta) + N_s^{Left}(-\theta) + N_s^{Right}(-\theta),} \tag{8.8}$$

where $N_s^{Left(Right)}$ is the number of $s\bar{s}$ events in a θ bin for left(right)-handed electron beam. The results are shown in Figure 8.9.

8.2.2 Analyzing power corrections

In the $\cos\theta$ distribution shown in Figure 8.4, the s-quark direction was determined from the particle direction with the known strangeness, such that, if $K^-(K^+)$ or $\Lambda(\bar{\Lambda})$ is tagged

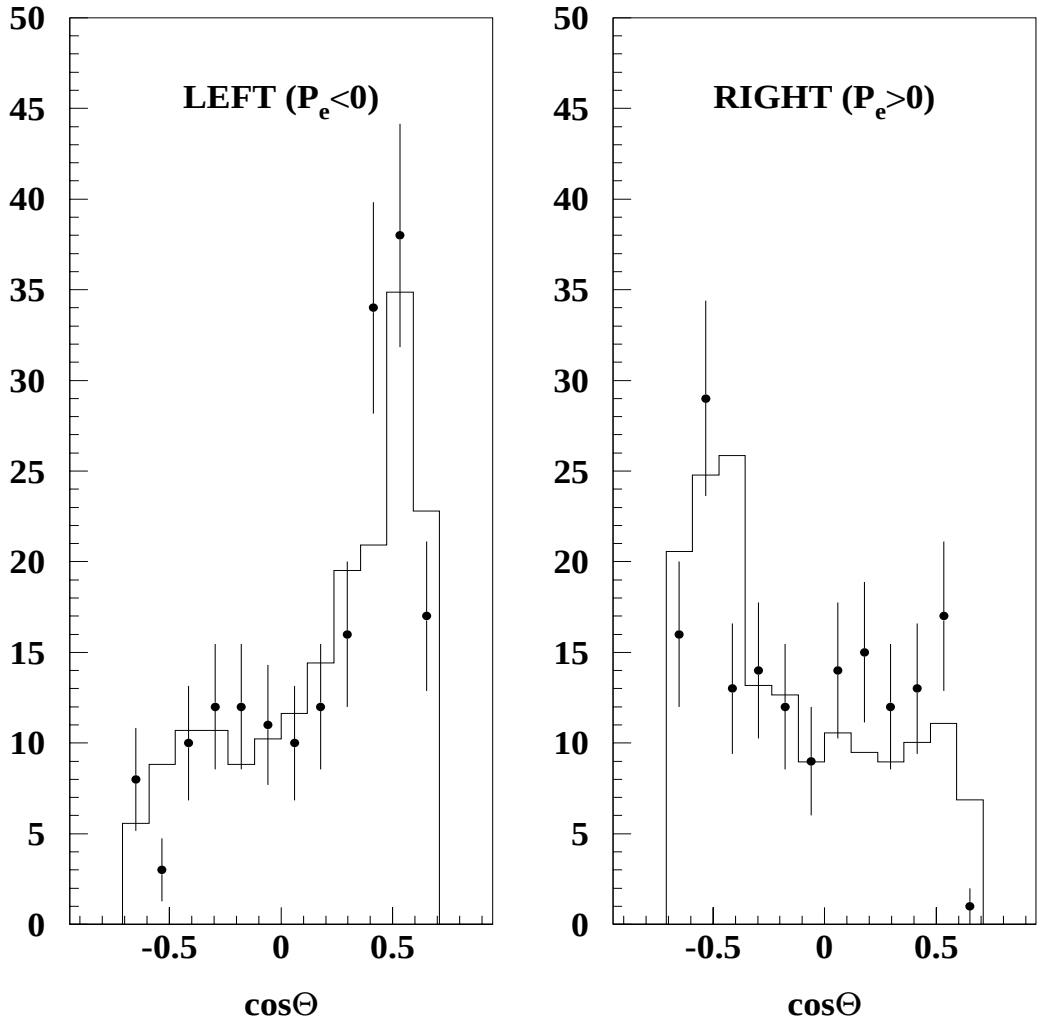

Figure 8.8: Signed thrust axis $\cos\theta$ after non-$s\bar{s}$ events subtraction using the Monte Carlo. The dots show data and the histogram shows the Monte Carlo results.

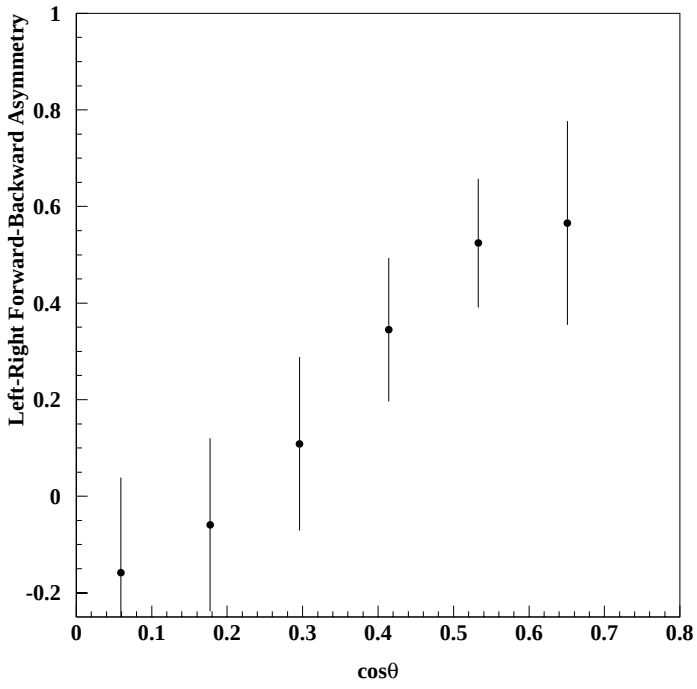

Figure 8.9: Left-Right Forward-Backward Asymmetry $\tilde{A}_{FB}^{raw}$

in a hemisphere, the thrust axis is taken as $s(\bar{s})$-quark direction. Since a tagged strange particle is not always the leading particle, the signed thrust axis does not always have the correct sign. This mis-assignment of the sign comes from two reasons; one is from tagging a non-leading strange particle (Figure 8.10-a), and the other from tagging a mis-identified particle in the CRID (Figure 8.10-b).

The probability to have the right sign is calculated by using the Monte Carlo for selected $s\bar{s}$ events in each θ bin. The probability, $\alpha(\theta)$, called "analyzing power" is defined by,

$$\alpha(\theta) = \frac{N_s^{right}(\theta)}{N_s^{right}(\theta) + N_s^{wrong}(\theta)}, \tag{8.9}$$

where $N_s^{right(wrong)}(\theta)$ is the number of $s\bar{s}$ events for which the thrust axis has the $right(wrong)$ sign. Figure 8.11 shows the expected analyzing power as a function of θ. Using this analyzing

power, the corrected $\tilde{A}^{corr}_{FB}(\theta)$ is given by,

$$\tilde{A}^{corr}_{FB}(\theta) = \frac{\tilde{A}^{raw}_{FB}(\theta)}{2\alpha(\theta) - 1}. \tag{8.10}$$

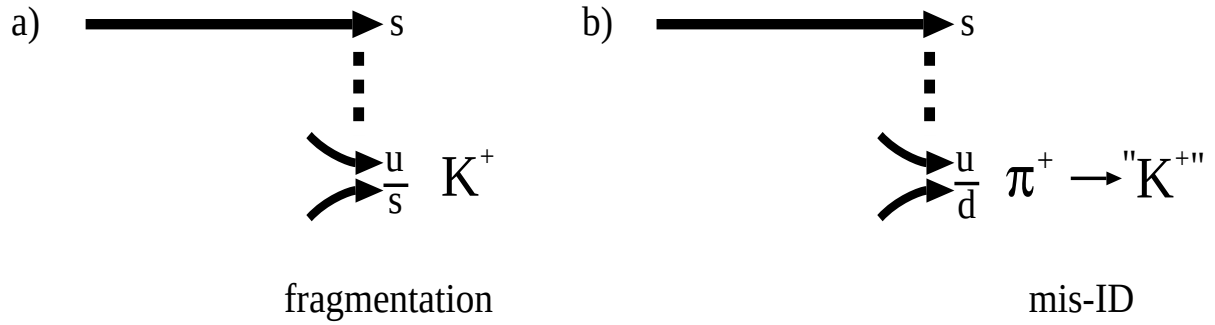

Figure 8.10: Mis-assignment of initial s-quark direction by a) tagging non-leading strange particle and b) CRID particle mis-identification.

8.2.3 QCD corrections

The smearing in the quark axis angle due to final-state QCD radiation dilutes the asymmetry. The first-order QCD corrections are calculated in [64, 65]. Figure 8.12 shows $\Delta_{O(\alpha_s)}$ which is given by,

$$\Delta_{O(\alpha_s)} = 1 - \frac{\tilde{A}^s_{FB}|_{O(\alpha_s)}}{\tilde{A}^s_{FB}|_{O(0)}}, \tag{8.11}$$

where $\tilde{A}^s_{FB}|_{O(0)}$ is the left-light forward-backward asymmetry for raw s quarks and $\tilde{A}^s_{FB}|_{O(\alpha_s)}$ is the left-light forward-backward asymmetry for s quarks with the first-order QCD radiative correction.

In this analysis, events with high momentum strange particles are selected. For such events, the effect of gluon radiation is expected to be smaller than calculated $\Delta_{O(\alpha_s)}$ since events with hard gluon radiation are less likely to have high momentum final state hadrons. In order to estimate such a bias factor, we measured A_s using the JETSET 7.4 generator to produce $s\bar{s}$ events with no gluon radiation, $s\bar{s}$ plus parton shower events, and $s\bar{s}$ plus parton

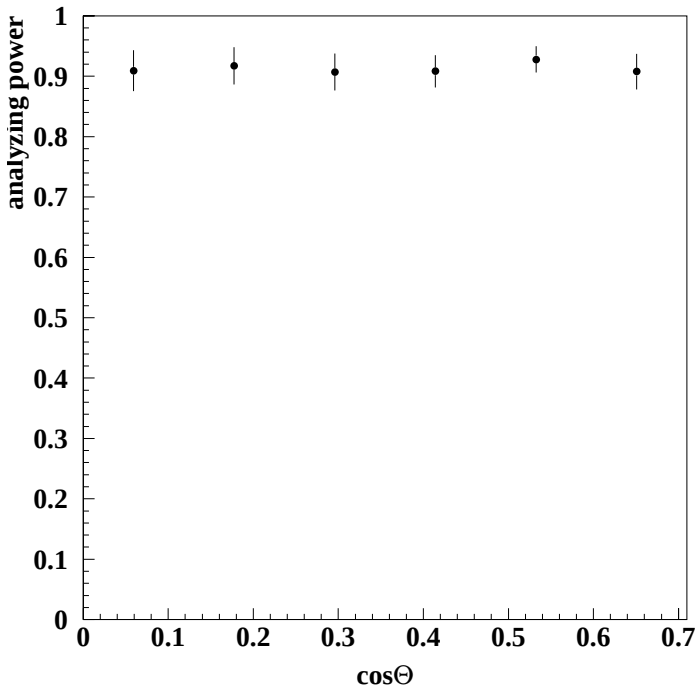

Figure 8.11: Analyzing power for $s\bar{s}$ events

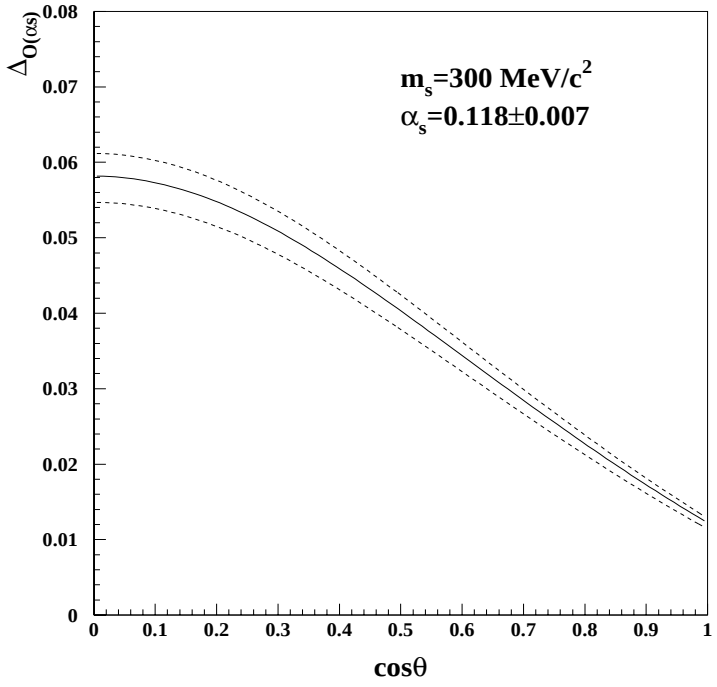

Figure 8.12: Polar angle dependence of first-order QCD radiative correction for s quarks. The dashed lines correspond to the error of α_s [66].

shower events with high momentum $K^{\pm}$ ($p > 9GeV/c$) and K_s^0 ($p > 5GeV/c$) pairs. Figure 8.13 shows the left-right forward-backward asymmetry as a function of $\cos\theta$ for each of these samples. We fitted the following function, $\tilde{A}_{FB}(\theta)$ to each Monte Carlo set;

$$\tilde{A}_{FB}(\theta) = \frac{2\cos\theta}{1+\cos^2\theta} A_s, \tag{8.12}$$

The bias factor b is defined by,

$$b \equiv \frac{A_s^{s\bar{s}} - A_s^{ptn'}}{A_s^{s\bar{s}} - A_s^{ptn}}, \tag{8.13}$$

where $A_s^{s\bar{s}}$, A_s^{ptn}, and $A_s^{ptn'}$ are A_s for the events with $s\bar{s}$, $s\bar{s}$ and parton shower, and $s\bar{s}$ and parton shower with high momentum $K^{\pm}$ and K_s^0 pairs respectively. From the fitted curve in Figure 8.13, A_s for each event sample are $A_s^{s\bar{s}} = 0.9335$, $A_s^{ptn} = 0.9206$, and $A_s^{ptn'} = 0.9271$, and the bias factor is calculated to be $b = 0.496$. The QCD correction factor including the analysis bias $b \cdot \Delta_{O(\alpha_s)}$ is applied for $\tilde{A}_{FB}^{corr}(\theta)$.

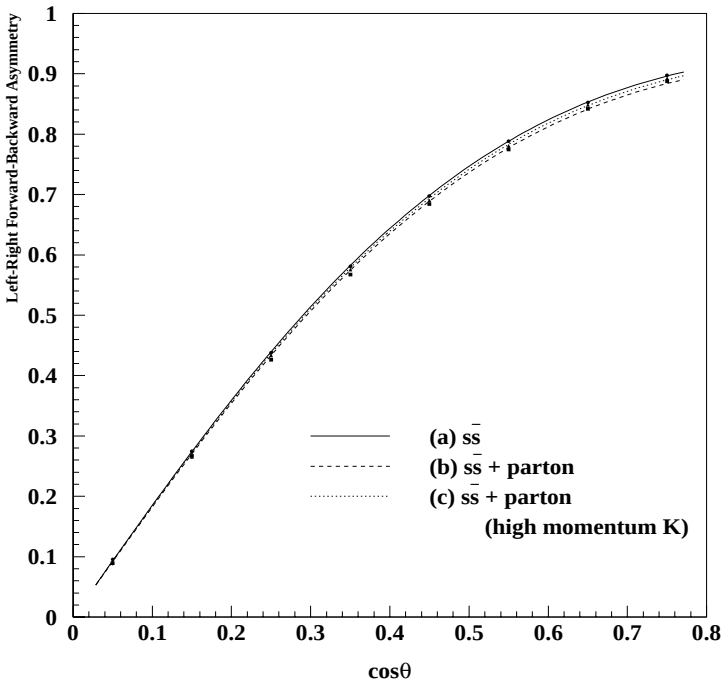

Figure 8.13: Left-Right Forward-Backward asymmetry of s quarks with JETSET 7.4 for events with (a) $s\bar{s}$ (b) $s\bar{s}$ and parton shower, and (c) $s\bar{s}$ and parton shower with high momentum $K^{\pm}$ ($p > 9GeV/c$) and K^0_s ($p > 5GeV/c$) pairs. The meaning of fitting curve is described in the text

8.2.4 A_s result

Finally, A_s is calculated from $b \cdot \Delta_{O(\alpha_s)} \times \tilde{A}^{corr}_{FB}(\theta)$. Figure 8.14 shows the left-right forward-backward asymmetry after the QCD correction as a function of polar angle. A_s is extracted by fitting the function of Eq(8.12). In the fitting, $|P_e|$ is the averaged electron polarization of 73.0% for 1993-95 runs [68]. The best fit gives the value of A_s,

$$A_s = 0.86 \pm 0.17(stat.). \tag{8.14}$$

The curve in Figure 8.14 is obtained from the fit showing a reasonable agreement with data within errors.

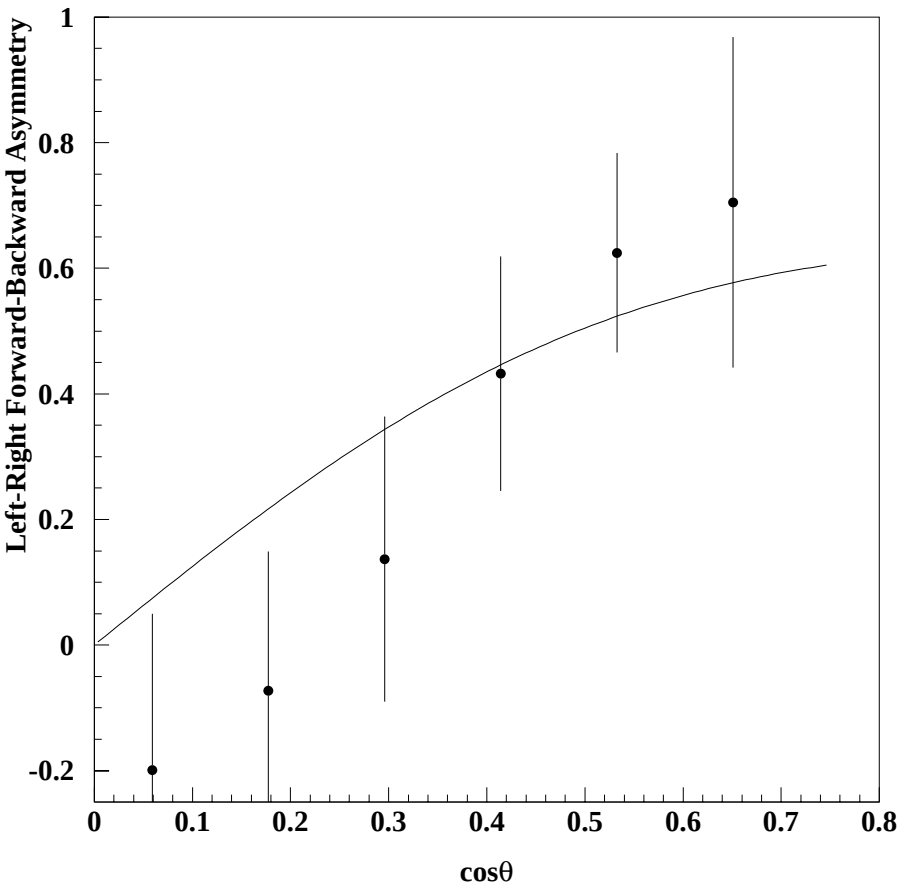

Figure 8.14: Left-right forward-backward asymmetry with analyzing power correction. The meaning of fitted curve is described in the text.

8.3 Systematic Errors

8.3.1 Background fraction and asymmetry

The fractions and the asymmetries of cb and ud backgrounds are sources of systematic errors in the Monte Carlo calculation of background. Uncertainties of these parameters should be taken into account.

For c and b quarks, $R_f = \Gamma(Z^0 \to f\bar{f})/\Gamma(Z^0 \to hadrons)$ and A_f $(f = c, b)$ have been well measured experimentally. This means the Monte Carlo is reliable for these parameters. Thus, we vary these values by the world average errors in these parameters, to examine the systematic error. The errors of these parameters in the world measurements are shown in Table 8.3.

Parameter (x)	error $(\delta x/x)$ [3]
R_c	0.048
R_b	0.008
A_c	0.148
A_b	0.063

Table 8.3: The world average error for R_f and A_f.

We consider the variation of the $u\bar{u}$ and $d\bar{d}$ event fraction in the tagged $K^{\pm}K^{\mp}$ and $K^{\pm}K^0_s$ events by changing the fragmentation parameters in the LUND symmetric model and the strangeness suppression factor within the world measurements error. Each parameter is varied as shown in Table 8.4. The largest variation of the fraction was found to be $\pm 15\%$ over the parameters considered and is taken as the uncertainty on the ud fraction in our Monte Carlo. For the uncertainty of the ud asymmetry in the Monte Carlo, we take $\pm 50\%$, which we believe to be the conceivable variation.

8.3.2 Analyzing Power

The analyzing power is also a sensitive parameter in the Monte Carlo for A_s. We take into account for the events with a charged kaon in both hemispheres. If both kaons are

leading, they should have opposite charge. If they have same charge, at least one kaon is supposed to be from non-leading. The analyzing power has been determined by physics in fragmentation process and particle mis-identification in the CRID. The non-leading charged kaon and mis-identified pion to kaon may dilute the analyzing power. In order to check whether these effects are estimated correctly, we compare the ratio of the number of same-sign charged kaon pairs ($N_{same} = N_{K^\pm K^\pm}$) to the number of opposite-sign charged kaon pairs ($N_{opp} = N_{K^\pm K^\mp}$) between data and the Monte Carlo. The ratio is calculated to be $N_{same}/N_{opp} = 0.342 \pm 0.045$ in the data and $N_{same}/N_{opp} = 0.381 \pm 0.025$ in the Monte Carlo. These values are consistent with each other. If we remove mis-identified kaons in the Monte Carlo, the ratio becomes to be $N_{same}/N_{opp} = 0.283 \pm 0.022$. This implies that the CRID mis-identifications contribute about $\sim 25\%$ of dilution effect. We also consider the pairs of $K^\pm$ and K^0_s. From the Monte Carlo, the ratio of mis-identified charged kaons in the pairs is $7.9 \pm 1.0\%$. This value agrees with the CRID mis-identification ratio of pion to kaon[1], that is to say, the Monte Carlo simulates reasonably also for $K^\pm K^0_s$ pairs. We suppose an extreme case where the difference of the ratio for K^+K^- pairs between data and the Monte Carlo including their statistic errors, is thought to be the ambiguity of the dilution effect.

8.3.3 Uncertainties from other inputs and fitting

Fragmentation Function and Strangeness suppression

The input parameters of the Lund symmetric fragmentation function and Peterson fragmentation function in the Monte Carlo were discussed in Chapter 4. We consider variation of those parameters based on the experimental measurements shown in Table 4.3. We generate 1,000,000 Z^0 hadronic events with various values and checked the changing of A_s without detector simulation. Also various values of strangeness suppression factor, γ_s were tested considering the experimental error. Table 8.4 shows A_s results with various fragmentation parameters and strangeness suppression factor.

[1] refer Figure 5.14

Parameter(default)	Input	$\delta A_s/A_s$ (%)
Lund symmetric $a(0.18)$	0.50	-0.28
$b(0.34)$	0.92	-0.05
Peterson $\epsilon_c(0.06)$	0.05	-0.05
	0.07	+0.13
$\epsilon_b(0.006)$	0.008	+0.35
$\gamma_s(0.28)$	0.265	-0.15
	0.295	+0.13

Table 8.4: The A_s variations for various fragmentation parameters inputs. For the default values, A_s =0.9348.

Polarization Uncertainties

For A_s measurement, an averaged electron polarization was used. The average electron polarization was $63.1 \pm 1.1\%$ for 1993 run, and during 1994-95 run, the average was $77.3 \pm 0.6\%$. Then, the luminosity-weighted average polarization was $73.0 \pm 0.5\%$ for 1993-95 SLD runs.

QCD correction

For the QCD radiative corrections, a value of $\alpha_s(M_Z^2) = 0.118$ was assumed, and we consider the error of α_s ($\delta\alpha_s = \pm 0.007$) as the systematic error.

Momentum cuts for strange samples

The A_s result showed in the previous section was measured with charged kaons which have momentum above 9 GeV/c and V^0s ($\Lambda^0/\bar{\Lambda}^0$s and K_s^0s) which have momentum above 5 GeV/c. The momentum cut dependence is checked with various cut values. Figure 8.15 shows measured A_s for various momentum cut for V^0 with fixed momentum cut for charged kaons. Then, the momentum cut values for charged kaon was varied to 10 GeV/c, 12 GeV/c, and 15 GeV/c making V^0 momentum cut value 5 GeV/c. The results are shown in Figure

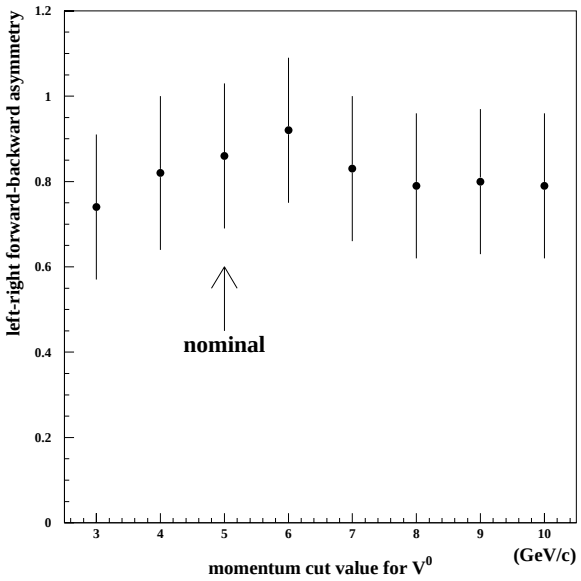

Figure 8.15: Measured A_s for various momentum cut values for V^0. In this plot, charged kaon momentum cut is fixed to 9 GeV/c

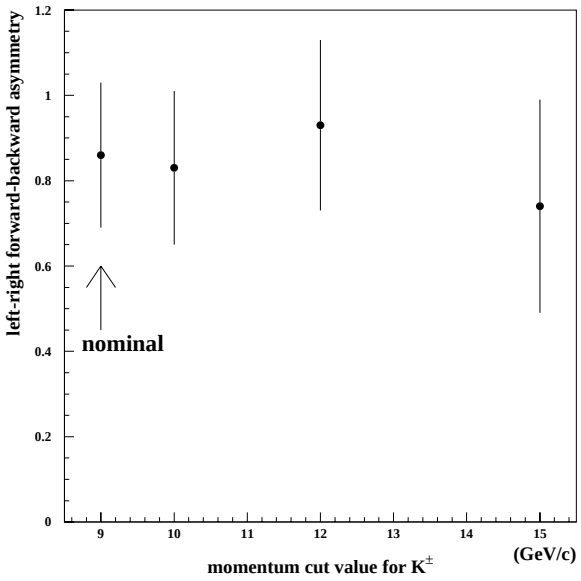

Figure 8.16: Measured A_s for various momentum cut values for $K^{\pm}$. In this plot, V^0 momentum cut is fixed to 5 GeV/c

8.16. For both plots, the root-mean-square for the averaged A_s is taken into account as systematic error. We take 6.6% and 8.1% uncertainties for V^0 momentum cuts and charged kaon momentum cuts.

8.3.4 Summary of the systematic errors

We have examined the conceivable systematic errors for measured A_s. A summary of systematic errors is shown in Table 8.5

SOURCE	RANGE	ERROR (δA_s)
cb fraction	$\pm 4.5\%$	0.003
cb asymmetry	$\pm 14\%$	0.009
ud fraction	$\pm 15\%$	0.052
ud asymmetry	$\pm 50\%$	0.030
Analyzing Power	$\pm 27\%$	0.048
Lund symmetric param.	$0.18 \leq a \leq 0.50$, $0.34 \leq b \leq 0.92$	0.002
Peterson ϵ_c	$0.05 \leq \epsilon_c \leq 0.07$	0.001
Peterson ϵ_b	$0.006 \leq \epsilon_b \leq 0.008$	0.003
Strangeness suppression γ_s	$0.265 \leq \gamma_s \leq 0.295$	0.001
QCD correction	$\delta\alpha_s = \pm 0.007$	0.001
Polarization	$\pm 0.5\%$	0.006
Momentum cut dependence	$\pm 8.1\%$	0.069
TOTAL		0.103

Table 8.5: Summary of estimated systematic errors

Chapter 9

Summary

We have presented the first direct measurement of A_s, the parity violating parameter of the coupling of s quarks to the Z^0 boson. The analysis is based upon the approximately 150,000 hadronic Z^0 events obtained from the SLD run data between 1993 and 1995 using the highly polarized electron beams. We selected a sample of highly pure $s\bar{s}$ events by using high momentum strange particles based on the leading particle effect. The SLD vertex detector has an excellent vertex resolution, and it allows to separate light flavor events from heavy flavor events, so that the heavy flavor background in the final $s\bar{s}$ sample was remarkably suppressed. In this analysis, the Cherenkov Ring Imaging Detector (CRID) played an important role to tag high momentum strange particle. For this analysis, we had improved the particle identification performance of the CRID, and we have achieved high tagging efficiency and tagged high momentum charged kaons and $\Lambda^0/\bar{\Lambda}^0$ baryons with high purity. Using the selected $s\bar{s}$ events, we form left-right forward-backward asymmetry where the thrust axis has been signed with the strangeness of tagged strange particle. The SLD Monte Carlo, incorporating JETSET 7.4 and GEANT detector simulation, was used to estimate the non-s contamination in selected $s\bar{s}$ sample, assignment of correct quark sign, and other physics effects (fragmentation, final state radiation). Finally, this measurement gives,

$$A_s = 0.86 \pm 0.17(stat.) \pm 0.10(syst.). \tag{9.1}$$

The systematic error arises almost entirely from the use of the Monte Carlo to estimate non-s events contamination and the dependence of momentum cut for strange particles.

In order to check the universality of coupling constant, we compare this result with A_b results. Figure 9.1 shows a comparison of A_s with the world's measurements of A_b [69, 1]. The value of A_s agrees with both the Standard Model prediction and other A_b results although the error is still large. From this, we conclude that no significant evidence is observed to violate the universality of the coupling constants and the universality is held within the error.

For future prospects, the systematic errors in the ud background estimation should be decreased. One possibility is tuning the Monte Carlo in the QCD process. Many QCD parameters (fragmentation parameter, hadron production rates, strangeness suppression factor, *etc*) have been measured and we will get a more precise value in the future. We expect we will be able to tune the Monte Carlo more reliably.

The SLC is scheduled to run until 1998, aiming to accumulate 500,000 hadronic Z^0 decays. With such a large number of data, the statistic error as well as the systematic error of A_s will be decreased to make a precise test for the universality of the weak coupling constants.

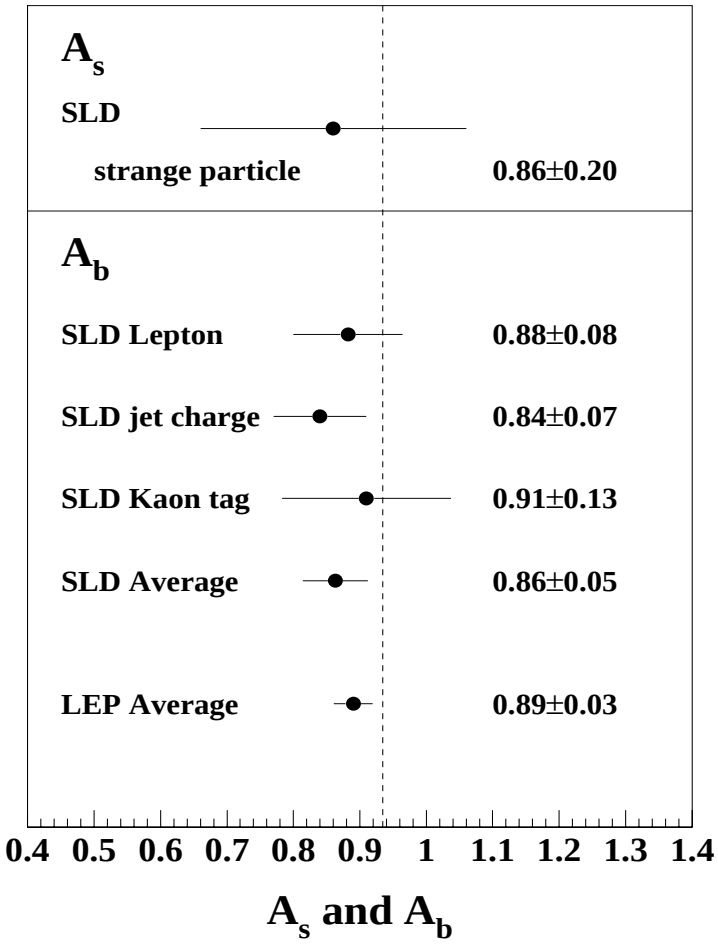

Figure 9.1: A comparison of A_s with the world's measurement of A_b. The vertical line is drawn at the standard model value of $A_s = A_b = 0.935$. The LEP result is derived using LEP averaged lepton asymmetry parameter $A_l = 0.1466 \pm 0.0033$.

Appendix A

The Likelihood Method

The statistical technique of *maximum likelihood* tests a hypothesis for the distribution of observed data by considering a likelihood function $\mathcal{L}$, which is the probability of producing the observed data given a particular hypothesis. In our case, a hypothesis consists of a set of particle assignments $\{h_k\}$ for each track k and a background model $B(\vec{x})$. Let $\bar{n}$ be the expected number of photons for the hypothesis $\{h_k\}$. If n is the observed number of photoelectrons in the CRID, then the probability of n given $\bar{n}$ is just the Poisson term

$$P(n|\bar{n}) = \frac{\bar{n}^n}{n!} e^{-\bar{n}}. \tag{A.1}$$

In addition to the number of photons, we also have information from the spatial distribution of the photons. Let $P(\vec{x})$ be the probability of a given photoelectron being in a differential volume $d^3\vec{x}$. Then $\bar{n}P(\vec{x})$ is the expected number of photoelectrons in $d^3\vec{x}$. Define this to be $\rho(\vec{x})$. Taking into account the permutations of the n photoelectrons, the overall likelihood is given by

$$\begin{aligned} \mathcal{L} &= P(n|\bar{n}) P\left(\{\vec{x_i}\}\right) \\ &= \bar{n}^n e^{-\bar{n}} \prod_{i=1}^{n} P(\vec{x_i}) \\ &= e^{-\bar{n}} \prod_{i=1}^{n} \rho(\vec{x_i}), \end{aligned} \tag{A.2}$$

where the index i runs over all observed photoelectrons.

It is convenient to split up $\rho(\vec{x})$ into a background term independent of tracks and a term

representing the Cherenkov rings produced by each track,

$$\rho(\vec{x}) = B(\vec{x}) + \sum_k \rho_{k,h_k}(\vec{x}), \tag{A.3}$$

where $\rho_{k,h_k}(\vec{x})$ represents the density due to track k, given particle hypothesis h_k for that track. Furthermore, it is simpler to describe ρ_{k,h_k} in terms of a different set of coordinates, (θ_c, ϕ_c, l), in which θ_c is the Cherenkov polar angle, ϕ_c is the Cherenkov azimuthal angle, and l is the conversion depth of the photoelectron along the photon's trajectory. In this new set of coordinates, we can write the density as

$$\rho_{k,h_k}(\vec{x}) = \frac{N_{k,h_k}}{2\pi} \frac{e^{-l/\lambda}}{\lambda} \frac{e^{-(\theta_c-\theta_0)^2/2\sigma_\theta^2}}{\sqrt{2\pi}\sigma_\theta} \frac{1}{\mathcal{J}}, \tag{A.4}$$

where $\mathcal{J}$ is the Jacobian $\partial(x,y,z)/\partial(\theta_c,\phi_c,l)$, λ is the photon absorption length in the TPC gas, θ_0 is the expected Cherenkov angle for track k and hypothesis h_k, and σ_θ is the resolution on the Cherenkov angle measurement at position $\vec{x}$. The factor N_{k,h_k} is the number of photoelectrons expected per full ring for track k and hypothesis h_k (which may be zero if h_k is below threshold, for example). Because of total internal reflection, the allowable ϕ_c range for a liquid ring may be less than the full $[-\pi, \pi]$. This effect is included into the Jacobian $\mathcal{J}$, which will go to 0 where no space point (x,y,z) can produce a hit at the given (θ_c, ϕ_c, l). Alternatively, one can define M_{k,h_k} to be the number of photoelectrons expected after accounting for total internal reflection. Then $N_{k,h_k}/2\pi = M_{k,h_k}/\Delta\Phi$, where $\Delta\Phi$ is the allowed ϕ range.

In principle, the likelihood $\mathcal{L}$ is now straightforward to compute for all 5 hypotheses of each track, and the set $\{h_k\}$ which maximizes $\mathcal{L}$ is our best answer. In practice, however, we cannot compute such an exponentially-large number of combinations. Instead, we make the simplifying assumption that the most likely hypothesis h_k for track k is largely independent of the hypotheses for other tracks $\{h_j\}_{j\neq k}$. We then iterate through the set of tracks, choosing each h_k to be the current best hypothesis for track k (favoring the π hypothesis when information is absent or ambiguous), and continue until the set $\{h_k\}$ is stable.

Let us define the likelihood for a hypothesis h_k to be

$$\mathcal{L}_{k,h_k} \equiv e^{-M_{k,h_k}} \prod_i \left(B_k + \rho_{k,h_k}(\vec{x_i})\right), \tag{A.5}$$

where B_k is the background that is independent of track k,

$$B_k(\vec{x}) \equiv B(\vec{x}) + \sum_{j \neq k} \rho_{j,h_j}(\vec{x}). \tag{A.6}$$

Then our independence assumption is equivalent to the difference in overall likelihood between hypothesis h_k and h'_k being given by

$$\frac{\mathcal{L}(h_k, \{h_j\}_{j \neq k})}{\mathcal{L}(h'_k, \{h_j\}_{j \neq k})} = \frac{\mathcal{L}_{k,h_k}}{\mathcal{L}_{k,h'_k}}. \tag{A.7}$$

Hence, we need only maximize each $\mathcal{L}_{k,h_k}$ for the five hypotheses h_k (and then iterate).

Since we are only concerned with relative likelihoods, we can divide through by a factor to get

$$\mathcal{L}'_{k,h_k} = e^{-M_{k,h_k}} \prod_i \left(1 + \frac{\rho_{k,h_k}(\vec{x_i})}{B_k(\vec{x_i})}\right), \tag{A.8}$$

or

$$\log \mathcal{L}'_{k,h_k} = -M_{k,h_k} + \sum_i \log \left(1 + \frac{\rho_{k,h_k}(\vec{x_i})}{B_k(\vec{x_i})}\right), \tag{A.9}$$

which is what we practically use in our analysis. Hence, the important criteria for particle identification are the ratios of Cherenkov angle weights $\rho_{k,h_k}(\vec{x_i})$ to backgrounds $B_k(\vec{x_i})$. Hits with signal weight significantly below the background weight are automatically ignored. Thus, a particle with hits nowhere near expected rings for any hypotheses is classified as ambiguous. For particles which are below threshold, the likelihoods of their above-threshold assignments are controlled by the expected number of hits $\log \mathcal{L}'_{k,h_k} = -M_{k,h_k}$.

In practice, the iterative procedure is found to converge rapidly. The $\{h_k\}$ all start at the π hypothesis and converge for most events in only two iterations. One weakness of the method lies in the need to know the correct background model $B(\vec{x})$. We currently use a uniform density per TPC, with the normalization computed from counting photoelectrons which have negligible weight ($< 10^{-4}$) for any hypothesis for any track. Separate backgrounds are used for the liquid and gas sides of the TPCs, and quartz Cherenkov photons are properly included in the background (*i.e.*, they are treated in the category of signal hits from other tracks). There is some evidence that real backgrounds are non-uniform and concentrated towards the two windows of the TPC. Tuning of the background model could be an area for future improvement of the CRID particle identification performance [8].

Appendix B

The SLD Collaboration

* K. Abe,[19] K. Abe,[29] I. Abt,[13] T. Akagi,[27] N.J. Allen,[4] W.W. Ash,[27]† D. Aston,[27]
K.G. Baird,[24] C. Baltay,[33] H.R. Band,[32] M.B. Barakat,[33] G. Baranko,[9]
O. Bardon,[15] T. Barklow,[27] G.L. Bashindzhagyan,[18] A.O. Bazarko,[10]
R. Ben-David,[33] A.C. Benvenuti,[2] G.M. Bilei,[22] D. Bisello,[21] G. Blaylock,[6]
J.R. Bogart,[27] T. Bolton,[10] G.R. Bower,[27] J.E. Brau,[20] M. Breidenbach,[27]
W.M. Bugg,[28] D. Burke,[27] T.H. Burnett,[31] P.N. Burrows,[15] W. Busza,[15]
A. Calcaterra,[12] D.O. Caldwell,[5] D. Calloway,[27] B. Camanzi,[11] M. Carpinelli,[23]
R. Cassell,[27] R. Castaldi,[23][a] A. Castro,[21] M. Cavalli-Sforza,[6] A. Chou,[27]
E. Church,[31] H.O. Cohn,[28] J.A. Coller,[3] V. Cook,[31] R. Cotton,[4] R.F. Cowan,[15]
D.G. Coyne,[6] G. Crawford,[27] A. D'Oliveira,[7] C.J.S. Damerell,[25] M. Daoudi,[27]
R. De Sangro,[12] P. De Simone,[12] R. Dell'Orso,[23] P.J. Dervan,[4] M. Dima,[8]
D.N. Dong,[15] P.Y.C. Du,[28] R. Dubois,[27] B.I. Eisenstein,[13] R. Elia,[27] E. Etzion,[4]
D. Falciai,[22] C. Fan,[9] M.J. Fero,[15] R. Frey,[20] K. Furuno,[20] T. Gillman,[25]
G. Gladding,[13] S. Gonzalez,[15] G.D. Hallewell,[27] E.L. Hart,[28] A. Hasan,[4]
Y. Hasegawa,[29] K. Hasuko,[29] S. Hedges,[3] S.S. Hertzbach,[16] M.D. Hildreth,[27]
J. Huber,[20] M.E. Huffer,[27] E.W. Hughes,[27] H. Hwang,[20] Y. Iwasaki,[29]
D.J. Jackson,[25] P. Jacques,[24] J. Jaros,[27] A.S. Johnson,[3] J.R. Johnson,[32]
R.A. Johnson,[7] T. Junk,[27] R. Kajikawa,[19] M. Kalelkar,[24] H. J. Kang,[26]
I. Karliner,[13] H. Kawahara,[27] H.W. Kendall,[15] Y. Kim,[26] M.E. King,[27] R. King,[27]

R.R. Kofler,[16] N.M. Krishna,[9] R.S. Kroeger,[17] J.F. Labs,[27] M. Langston,[20] A. Lath,[15] J.A. Lauber,[9] D.W.G.S. Leith,[27] V. Lia,[15] M.X. Liu,[33] X. Liu,[6] M. Loreti,[21] A. Lu,[5] H.L. Lynch,[27] J. Ma,[31] G. Mancinelli,[22] S. Manly,[33] G. Mantovani,[22] T.W. Markiewicz,[27] T. Maruyama,[27] R. Massetti,[22] H. Masuda,[27] E. Mazzucato,[11] A.K. McKemey,[4] B.T. Meadows,[7] R. Messner,[27] P.M. Mockett,[31] K.C. Moffeit,[27] B. Mours,[27] D. Muller,[27] T. Nagamine,[27] S. Narita,[29] U. Nauenberg,[9] H. Neal,[27] M. Nussbaum,[7] Y. Ohnishi,[19] L.S. Osborne,[15] R.S. Panvini,[30] H. Park,[20] T.J. Pavel,[27] I. Peruzzi,[12][b] M. Piccolo,[12] L. Piemontese,[11] E. Pieroni,[23] K.T. Pitts,[20] R.J. Plano,[24] R. Prepost,[32] C.Y. Prescott,[27] G.D. Punkar,[27] J. Quigley,[15] B.N. Ratcliff,[27] T.W. Reeves,[30] J. Reidy,[17] P.E. Rensing,[27] L.S. Rochester,[27] P.C. Rowson,[10] J.J. Russell,[27] O.H. Saxton,[27] T. Schalk,[6] R.H. Schindler,[27] B.A. Schumm,[14] S. Sen,[33] V.V. Serbo,[32] M.H. Shaevitz,[10] J.T. Shank,[3] G. Shapiro,[14] D.J. Sherden,[27] K.D. Shmakov,[28] C. Simopoulos,[27] N.B. Sinev,[20] S.R. Smith,[27] J.A. Snyder,[33] P. Stamer,[24] H. Steiner,[14] R. Steiner,[1] M.G. Strauss,[16] D. Su,[27] F. Suekane,[29] A. Sugiyama,[19] S. Suzuki,[19] M. Swartz,[27] A. Szumilo,[31] T. Takahashi,[27] F.E. Taylor,[15] E. Torrence,[15] A.I. Trandafir,[16] J.D. Turk,[33] T. Usher,[27] J. Va'vra,[27] C. Vannini,[23] E. Vella,[27] J.P. Venuti,[30] R. Verdier,[15] P.G. Verdini,[23] S.R. Wagner,[27] A.P. Waite,[27] S.J. Watts,[4] A.W. Weidemann,[28] E.R. Weiss,[31] J.S. Whitaker,[3] S.L. White,[28] F.J. Wickens,[25] D.A. Williams,[6] D.C. Williams,[15] S.H. Williams,[27] S. Willocq,[33] R.J. Wilson,[8] W.J. Wisniewski,[27] M. Woods,[27] G.B. Word,[24] J. Wyss,[21] R.K. Yamamoto,[15] J.M. Yamartino,[15] X. Yang,[20] S.J. Yellin,[5] C.C. Young,[27] H. Yuta,[29] G. Zapalac,[32] R.W. Zdarko,[27] C. Zeitlin,[20] and J. Zhou,[20]

[1] *Adelphi University, Garden City, New York 11530*

[2] *INFN Sezione di Bologna, I-40126 Bologna, Italy*

[3] *Boston University, Boston, Massachusetts 02215*

[4] *Brunel University, Uxbridge, Middlesex UB8 3PH, United Kingdom*

[5] *University of California at Santa Barbara, Santa Barbara, California 93106*

[6] *University of California at Santa Cruz, Santa Cruz, California 95064*

[7] *University of Cincinnati, Cincinnati, Ohio 45221*

[8] *Colorado State University, Fort Collins, Colorado 80523*

[9] *University of Colorado, Boulder, Colorado 80309*

[10] *Columbia University, New York, New York 10027*

[11] *INFN Sezione di Ferrara and Università di Ferrara, I-44100 Ferrara, Italy*

[12] *INFN Lab. Nazionali di Frascati, I-00044 Frascati, Italy*

[13] *University of Illinois, Urbana, Illinois 61801*

[14] *Lawrence Berkeley Laboratory, University of California, Berkeley, California 94720*

[15] *Massachusetts Institute of Technology, Cambridge, Massachusetts 02139*

[16] *University of Massachusetts, Amherst, Massachusetts 01003*

[17] *University of Mississippi, University, Mississippi 38677*

[18] *Moscow State University, Institute of Nuclear Physics, 119899 Moscow, Russia*

[19] *Nagoya University, Chikusa-ku, Nagoya 464 Japan*

[20] *University of Oregon, Eugene, Oregon 97403*

[21] *INFN Sezione di Padova and Università di Padova, I-35100 Padova, Italy*

[22] *INFN Sezione di Perugia and Università di Perugia, I-06100 Perugia, Italy*

[23] *INFN Sezione di Pisa and Università di Pisa, I-56100 Pisa, Italy*

[24] *Rutgers University, Piscataway, New Jersey 08855*

[25] *Rutherford Appleton Laboratory, Chilton, Didcot, Oxon OX11 0QX United Kingdom*

[26] *Sogang University, Seoul, Korea*

[27] *Stanford Linear Accelerator Center, Stanford University, Stanford, California 94309*

[28] *University of Tennessee, Knoxville, Tennessee 37996*

[29] *Tohoku University, Sendai 980 Japan*

[30] *Vanderbilt University, Nashville, Tennessee 37235*

[31] *University of Washington, Seattle, Washington 98195*

[32] *University of Wisconsin, Madison, Wisconsin 53706*

[33] *Yale University, New Haven, Connecticut 06511*

[†] *Deceased*

[a] *Also at the Università di Genova*

[b] *Also at the Università di Perugia*

Bibliography

[1] The LEP Electroweak Working Group and the SLD Heavy Flavor Group, *A Combination of Preliminary LEP and SLD Electroweak Measurements and Constraints on the Standard Model*, LEPEWWG/96-02, ALEPH 96-107 PHYSIC 96-98, DELPHI 96-121 PHYS 631, L3 Note 1975, OPAL Technical Note TM 399, SLD Physics Note 52, (1996).

[2] DELPHI collaboration: P. Abreu *et al.*, Z. Phys. **C67** (1995) 1.

[3] Particle Data Group, *Review of Particle Physics*, Phys. Rev. **D53** (1996)

[4] detailed descripition of Z^0 production and decay can be found in, for example, C. Quigg, *Gauge Theories of the Strong, Weak, and Electromagnetic Interactions*, Frontiers in physics 56, 1983.

[5] Paolo Gambino and Alberto Sirlin, Phys. Rev. **D49** (1994) 1160.

[6] A. Blondel, B. W. Lynn, F. M. Renard, and C. Verzegnassi, Nucl. Phys. **B304** (1988) 438.

[7] K. G. Baird, Ph. D. dissertaion, Rutgers University, (1995); also SLAC-R-483.

[8] T. J. Pavel, Ph. D. dissertation, Stanford University, (1996).

[9] X. Artru and G. Mennessier, Nucl. Phys. **B70** (1974) 93.

[10] B. Andersson, G. Gustafson, and T. Sjöstrand, Z. Phys. **C6** (1980) 235.

[11] T. Sjöstrand, Comp. Phys. Commun. **39** (1986) 347.

[12] B. Foster, *Electron-Positron Annihiltion Physics*, 1990.

[13] P. N. Burrows and H. Masuda, SLD Physics Note 36 (1995).

[14] M. Basile *et al.*, IL Nuovo Cimento **A66** (1981) 129.

[15] ALEPH Collaboration: D. Buskulic *et al.*, Z. Phys. **C62** (1994) 179.
DELPHI Collaboration: P. Abreu *et al.*, CERN-PPE/95-08 (1995).
L3 Collaboration: B. Adeva *et al.*, Phys. Lett. **B261** (1991) 177.
OPAL Collaboration: R. Akres *et al.*, Z. Phys. **C60** (1993) 199.

[16] SLD collaboration: K. Abe *et al.*, SLAC-PUB-7197, (1996).

[17] L. Hendrickson *et al.* SLAC-PUB-6621 (1994). Presented at the 17^{th} International Linear Accelerator Conference (LINAC 94), Tsukuba, Japan 1994.

[18] M. Swartz, SLAC-PUB-4656, (1988).

[19] SLD collaboration: K. Abe *et al.*, Phys. Rev. Lett. **70** (1993) 2515.

[20] SLD collaboration: K. Abe *et al.*, Phys. Rev. Lett. **73** (1995) 24.

[21] R. Prepost, Proceedings of the 21^{st} SLAC Summer Institute on Particle Physics, SLAC-REPORT-444, (1994) 57.

[22] J. Kent *et al.*, SLAC-PUB-4922, (1989).

[23] D. Calloway *et al.*, SLAC-PUB-6423, (1994).

[24] A. Lath, Ph. D. dissertaion, Massachusetts Institute of Technology,(1994); also SLAC-R-454.

[25] SLD Design Report SLAC-Report-273, (1984).

[26] S. C. Berridge *et al.*, IEEE Trans. Nucl. Sci. **37** (1990) 1191.

[27] K. T. Pitts, Ph. D. dissertaion, University of Oregon (1994); also SLAC-R-446.

[28] M. Strauss, SLAC-PUB-6686, (1994).

[29] J. P. Venuti and G. B. Chadwick, IEEE Trans. Nucl. Sci. **NS-36** (1989) 595.

[30] D. Axen *et al.*, Nucl. Instrum. Methods **A238** (1993) 472.

[31] S. Gonzalez, Ph. D. dissertation, Massachusetts Institute of Technology (1994); also SLAC-R-439.

[32] SLD collaboration: K. Abe *et al.*, Phys. Rev. **D53** (1996) 1023.

[33] A. C. Benvenuti *et al.*, Nucl. Instrum. Methods **A276** (1989) 94.

[34] Mark II collaboration: A. Peterson *et al.*, Phys. Rev. **D37** (1988) 1.

[35] TASSO collaboration: W. Braunshweig *et al.*, Z. Phys. **C41** (1988) 359.

[36] OPAL collaboration: M. Z. Akrawy *et al.*, Z. Phys. **C47** (1990) 505.

[37] ALEPH collaboration: D. Buskulic *et al.*, Z. Phys. **C55** (1992) 209.

[38] L3 collaboration: B. Adeva *et al.*, Z. Phys. **C55** (1992) 39.

[39] R. Brun *et al.*, *GEANT3*, CERN-DD/EE/84-1 (1987); Cern Application Software Group, *GEANT 3.21 Program*, CERN Program Library (1994).

[40] T. R. Junk, Ph. D. dissertation, Stanford University (1995); also SLAC-R-476.

[41] H. C. Fesefeldt, *Simulation of Hadronic Showers, Physics and Applications*, Technical Report PITHA 85-02, III Physikalisches Institut, Aachen, Germany (1985).

[42] W. Nelson, H. Hirayama, D. W. O. Rogers, SLAC-R-265 (1985).

[43] H. Neil, Ph. D. dissertation, Stanford University (1995); also SLAC-R-473.

[44] R. A. Holyroyd, J. M. Presses, C. L. Woody and R. A. Johnson, Nucl. Instrum. Methods **A261** (1987) 440.

[45] T. Ypsilantis and J. Séguinot, Nucl. Instrum. Methods **A343** (1994) 30.

[46] A. Bean *et al.*, Nucl. Instrum. Methods **A300** (1991) 501.

[47] J. Séguinot and T. Ypsilantis, Nucl. Instrum. Methods **A142** (1977) 377.

[48] H. Kawahara and J. Va'vra, SLD CRID Note 78 (1993).

[49] J. Va'vra *et al.*, Nucl. Instrum. Methods **A343** (1994) 74.

[50] H. Kawahara, D. Muller, S. Narita, SLD CRID Note 83 (1994).

[51] K. Abe et al, SLAC-PUB 5986, (1992).

[52] M. Cavalli-Sforza *et al.*, IEEE Trans. Nucl. Sci. **NS-37** (1990) 1132.

[53] SLD CRID collaboration: K. Abe *et al.*, Nucl. Instrum. Methods **A300** (1991) 501.

[54] D. Muller, SLD CRID Note 88, in preparation.

[55] S. J. Yellin, SLD CRID Note 49 (1988).

[56] K. Abe *et al.*, Nucl. Instrum. Methods **A371** (1996) 195.

[57] David Aston, Tom Pavel, David Muller, SLD Physics Note 35 (1995).

[58] SLD collaboration: K. Abe *et al.*, SLAC-PUB-7199 (1996).

[59] J. M. Yamartino, Ph. D. dissertation, Massachusetts Institute of Technology (1994); also SLAC-R-426.

[60] P. N. Burrows, H. Park, K. T. Pitts, J. M. Martino, SLD Note 229, (1993).

[61] K. Hayes, in Proceedings of the Third Mark II Workshop on SLC Physics, SLAC-R-315, (1993).

[62] Mark II collaboration: R. G. Jacobsen *et al.*, Phys. Rev. Lett. **67** (1991) 3347.

[63] R. G. Jacobsen, Ph. D. dissertation, Stanford University (1991); also SLAC-R-381.

[64] J. B. Stav and H. A. Olsen, Phys. Rev. **D54** (1996) 817.

[65] P. N. Burrows, SLD Physics Note 29 (1994).

[66] SLD A_{FB} group, (private communication).

[67] G. D. Lafferty, Phys. Lett. **B353** (1995) 541.

[68] D. Su, SLAC-PUB-7000 (1995).

[69] SLD collaboration: K. Abe *et al.*, SLAC-PUB-7233 (1996).